# New advances in using Raman spectroscopy for the characterization of catalysts and catalytic reactions

Christian Hess*

*Eduard-Zintl-Institut für Anorganische und Physikalische Chemie, Technische Universität Darmstadt, Alarich-Weiss-Str. 8, 64287 Darmstadt, Germany*

**e-mail: christian.hess@tu-darmstadt.de*

Gaining insight into the mode of operation of heterogeneous catalysts is of great scientific and economic interest. Raman spectroscopy has proven its potential as a powerful vibrational spectroscopic technique for a fundamental and molecular-level characterization of catalysts and catalytic reactions. Raman spectra provide important insight into reaction mechanisms by revealing specific information on the catalysts' (defect) structure in the bulk and at the surface, as well as the presence of adsorbates and reaction intermediates. Modern Raman instrumentation based on single-stage spectrometers allows high throughput and versatility in design of *in situ/operando* cells to study working catalysts. This review highlights major advances in the use of Raman spectroscopy for the characterization of heterogeneous catalysts made during the past decade, including the development of new methods and potential directions of research for applying Raman spectroscopy to working catalysts. The main focus will be on gas–solid catalytic reactions, but (photo)catalytic reactions in the liquid phase will be touched on if it appears appropriate.

The discussion begins with the main instrumentation now available for applying vibrational Raman spectroscopy to catalysis research, including *in situ/operando* cells for studying gas–solid catalytic processes. The focus then moves to the different types of information available from Raman spectra in the bulk and on the surface of solid catalysts, including adsorbates and surface depositions, as well as the use of theoretical calculations to facilitate band assignments and to describe (resonance) Raman effects. This is followed by a presentation of major developments in enhancing the Raman signal of heterogeneous catalysts by use of UV resonance Raman spectroscopy, surface-enhanced Raman spectroscopy (SERS), and shell-isolated nanoparticle surface-enhanced Raman spectroscopy (SHINERS). The application of time-resolved Raman studies to structural and kinetic characterization is then discussed. Finally, recent developments in spatially resolved Raman analysis of catalysts and catalytic processes are presented, including the use of coherent anti-Stokes Raman spectroscopy (CARS) and tip-enhanced Raman spectroscopy (TERS). The review concludes with an outlook on potential future developments and applications of Raman spectroscopy in heterogeneous catalysis.

Keywords: Raman spectroscopy, catalysis, reaction mechanism, *in situ*, *operando*, vibrations

**TOC graphic**

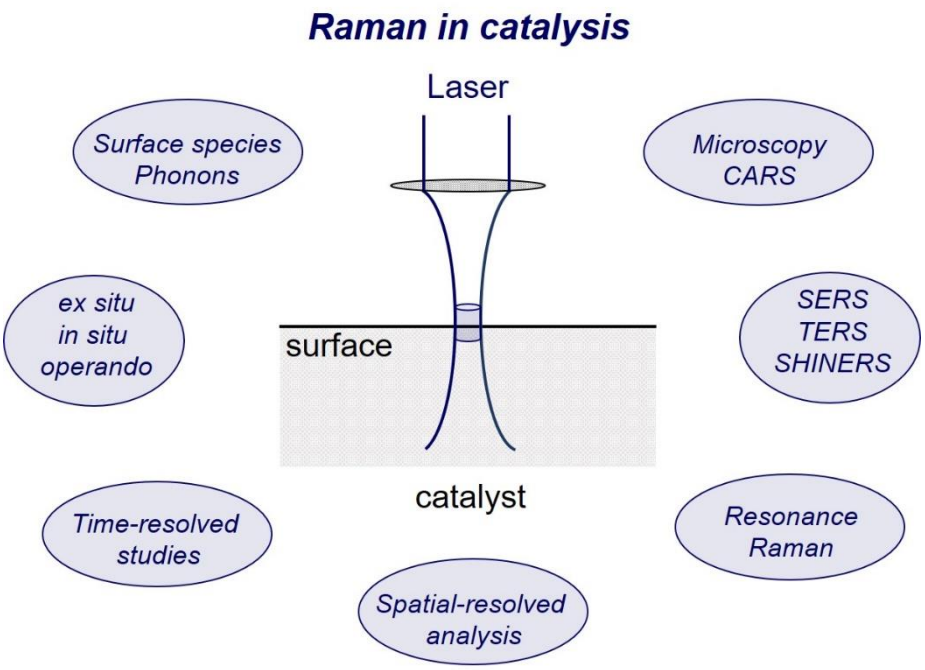
Raman in catalysis
Laser
Surface species
Phonons
Microscopy
CARS
ex situ
in situ
operando
SERS
TERS
SHINERS
surface
catalyst
Time-resolved
studies
Resonance
Raman
Spatial-resolved
analysis

## 1. Introduction

Raman spectroscopy is a vibrational spectroscopic technique and among the most versatile techniques for the characterization of catalysts materials, providing information about the catalysts' (defect) structure in the bulk and at the surface as well as the presence of adsorbates and reaction intermediates. Raman spectroscopy can be applied under a wide range of *in situ* and *operando* conditions. Raman spectra originate from the vibration of chemical bonds, thus providing access to the extended structure of crystalline solids (via phonons) but also the short-range structure of amorphous materials. Thus, when X-ray diffraction techniques are not applicable, Raman spectroscopy may provide insight into structure, changes in composition, or phase transitions.

Raman spectroscopy is based on the Raman effect, that is, the inelastic scattering of photons by a sample, which was predicted theoretically in 1923 by Smekal and discovered experimentally in 1928 for liquids and crystals, and in 1929 for gases. As a vibrational spectroscopic technique, Raman spectroscopy aroused considerable interest from the fundamental point of view but also regarding its applications. With respect to practical applicability of Raman spectroscopy, a breakthrough came with the invention of the laser in the 1960s, which boosted the sensitivity of the technique due to its brilliant, monochromatic, and coherent output, and greatly improved the quality of the spectra. Also, laser radiation could be focused onto a very small sample, thus enabling spectra to be obtained routinely from microgramme samples. Please refer to references 1-7 for reviews on Raman spectroscopy.[1-7]

First isolated studies applying Raman spectroscopy to catalytic materials go back to the 1960s, but in the late 1970s Raman characterization in catalysis started to show a first growth.[8-20] Based on the available Raman instrumentation at that time, namely double-stage spectrometers with single-channel photomultipliers, the overall sensitivity was limited, but even then, Raman spectra of supported metal oxide (molybdena, tungstia, vanadia) catalysts showed signals that were attributed to amorphous overlayers not accessible by X-ray

diffraction, in addition to features arising from crystalline oxide phases.[15,17-19] As an example, loading-dependent studies by Roozeboom *et al.* on alumina-supported vanadia showed the presence of amorphous vanadium in tetrahedral and (pseudo)octahedral coordination at lower loading and an increasing amount of crystalline $V_2O_5$ at higher loadings,[19] demonstrating the potential of Raman spectroscopy to detect and distinguish metal oxide surface and bulk structures, as also discussed in a broader perspective in the literature.[20-22]

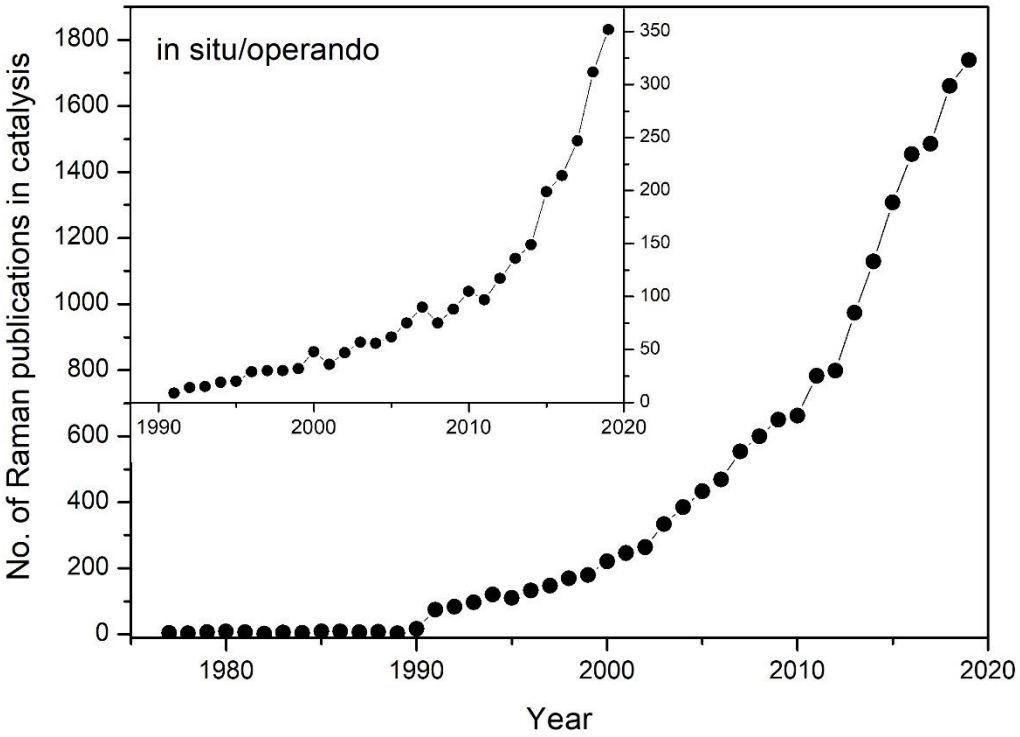


**Fig. 1** Number of Raman publications on catalysis versus year of publication. The inset gives the number of *in situ/operando* Raman studies.

In the early studies, the state of the catalyst (surface) was not always defined with respect to the presence of water. However, in the 1980s, the use of triple-stage spectrometers and optical multichannel analysers gave stronger Raman signals and facilitated *in situ* experiments, which allowed spectra to be recorded in defined gas environments and hence the surface

structural dynamics to be studied.[23-26] The availability of commercial Raman systems with increased sensitivity in the 1990s – based on the use of high-throughput single-stage spectrometers, notch filters for Rayleigh rejection, and high-efficiency multichannel detectors (charge-coupled device (CCD) arrays) – resulted in major growth of Raman characterization in catalysis (see Fig. 1). Since then, the number of catalysis-related Raman publications per year has continuously increased, from approximately 180 publications in 1999 to approximately 1800 by the end of 2019, with an increasing fraction of these publications being *in situ/operando* Raman studies (see inset). While laser emission was originally limited to visible wavelengths, nowadays, laser sources ranging from the deep ultraviolet (UV) to the near-infrared (NIR) region are available for Raman studies, enabling the effect of background fluorescence and sample absorption to be reduced efficiently. Besides, as an optical technique, Raman spectroscopy is compatible with the use of optical fibres for sending the excitation light to the sample and collecting the scattered light for remote detection. As the spatial and temporal resolution is determined by the characteristics of the excitation laser, Raman spectroscopy allows both time- and spatially-resolved measurements.

Raman spectroscopy is a powerful tool for the *in situ* characterization of heterogeneous catalysis as it can provide information about the structure of the catalyst material and surface species (including adsorbates) within one experiment, also under realistic reaction conditions (*operando* approach), as illustrated in Fig. 2. To introduce important features of Raman spectroscopy as applied to catalytic materials, some of the advantages and limitations of the technique will be discussed in the following.

Raman spectroscopy provides vibrational information on surface species (including adsorbed molecules) and solids, as does IR spectroscopy. However, there are a number of differences between these techniques, which are of relevance in the context of catalyst characterization. As Raman scattering in the gas phase is typically negligible, Raman spectra can be recorded without significant interference of gas-phase contributions from, for example,

strong IR absorbers such as $CO_2$ and $H_2O$. Glass and quartz are very weak Raman scatterers, thus allowing for an easy construction of *in situ/operando* cells. In contrast, for IR spectroscopy usually KBr windows are employed, which are sensitive to moisture and higher temperatures (i.e., cooling is required), and limit the transmission of light at low wavenumbers.

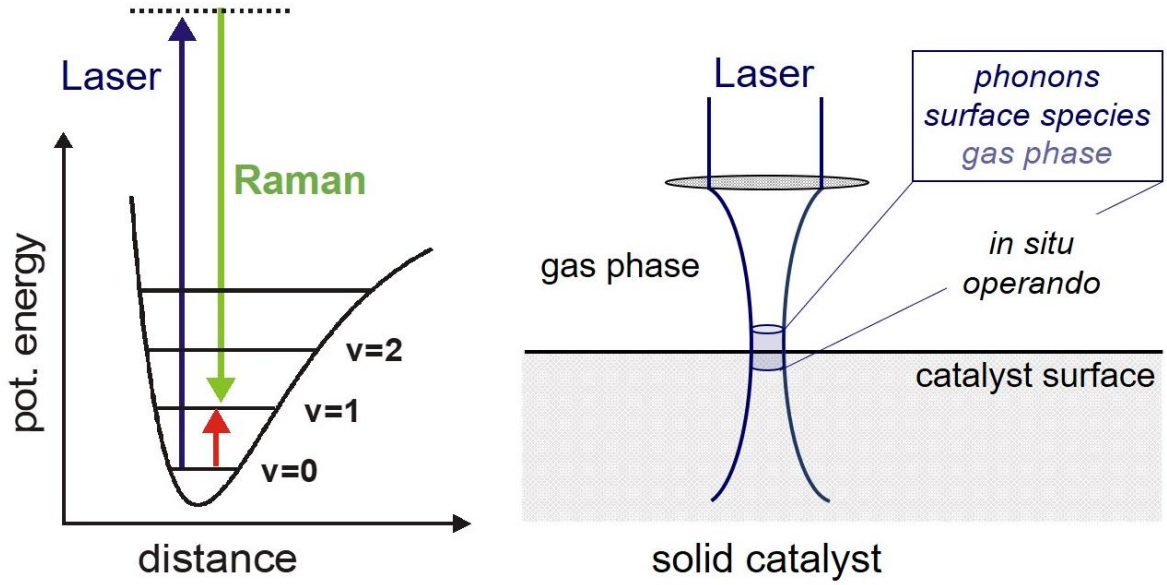


**Fig. 2** Vibrational Raman spectroscopy of solid catalysts. The Raman signal includes contributions from the surface and the bulk of the solid, whereas gas-phase contributions are usually negligible. Raman spectroscopy may be applied under *in situ/operando* conditions. The penetration depth of the laser beam depends on the properties of the solid and the excitation wavelength. As shown on the left, the Raman process is based on inelastic scattering of light. Right figure modified with permission from ref. 65, copyright 2010, Royal Society of Chemistry.

Modern Raman spectroscopy on heterogeneous catalysts is widely applied in a 180° backscattering geometry (see Fig. 2), allowing a versatile cell design, for example by designing *in situ/operando Raman* cells closely mimicking typical plug flow reactors. Raman spectra can

be recorded at elevated temperatures (> 1000°C). In particular, by using high-frequency laser excitation, the influence of blackbody radiation is efficiently reduced. For comparison, in the IR region, information from high-temperature spectra is typically limited, due to sample emission. To overcome this, the use of emission IR spectroscopy may be an alternative and commercial accessories are available, but emission IR spectroscopy has not developed into a routine technique yet.

Many common high-surface-area supports (e.g. $SiO_2$, $Al_2O_3$ etc.) are weak Raman scatterers, but show strong IR absorption below 1200 $cm^{-1}$. Thus, by using Raman spectroscopy, the supported phases are accessible routinely down to 150 $cm^{-1}$ or lower, depending on the type of filter/spectrometer. Besides catalyst characterization, a wide variety of processes related to catalyst preparation can be monitored, as water is a weak Raman scatterer.

The application of Raman spectroscopy to catalyst materials may be limited by the effects of laser irradiation, absorption, fluorescence, and the inherently low sensitivity of the technique. Laser irradiation may give rise to thermal heating of samples. As a consequence, catalyst samples may be partially or completely dehydrated, reduced or decomposed, or may undergo phase transitions or reactions (e.g. desorption of adsorbates). However, the effect of laser heating can be avoided by reducing the laser intensity on the sample, by power reduction, defocusing, sample movement, or cooling, or a combination of these. In principle, the sample temperature in the focus of the laser can be determined by measuring the Stokes and anti-Stokes intensity ratio of a vibration, however, commercial setups often do not allow the anti-Stokes range to be accessed. Besides thermal effects, laser irradiation may also lead to photochemical processes (e.g. in the UV), which can be efficiently overcome by defocusing and/or sample movement.

Major limitations of Raman spectroscopy may arise in the presence of fluorescence, which typically leads to the appearance of broad bands dominating the spectrum caused by, for

example, hydroxyl groups, organic impurities, or transition metal ions that are resonantly excited. Nowadays, fluorescence issues can often be reduced or even circumvented by changing the excitation wavelength, that is, by using NIR or UV laser excitation.

Compared to IR absorption coefficients, Raman (scattering) cross sections are small, resulting in the inherently low sensitivity of the Raman technique. However, this limitation was largely overcome by the development of high-throughput single-stage spectrometers combined with notch filters, and CCD cameras. In fact, due to their increased sensitivity and stability, this generation of Raman spectrometers has enabled time-resolved studies of catalytic reactions and the collection of kinetic data. Besides, the sensitivity of Raman spectroscopy can be further increased by exploiting resonance effects, for instance in resonance Raman spectroscopy, coherent anti-Stokes Raman spectroscopy (CARS), surface-enhanced Raman spectroscopy (SERS), or tip-enhanced Raman spectroscopy (TERS), which has led to the development of powerful Raman microscopy approaches with a spatial resolution down to single-molecule level. The increased sensitivity associated with the above Raman techniques has been explored only to some extent in the context of catalysis. Please note that in CARS/SERS/TERS the terms 'scattering' and 'spectroscopy' are used as synonyms.

An important aspect of Raman spectroscopy concerns the quantification of spectra. This is still a tremendous challenge, as Raman cross sections may depend on multiple parameters, such as temperature, pressure, gas-phase composition, or excitation wavelength. In the context of catalytic materials, relative Raman band intensities are commonly employed, for example by taking phonon bands or support bands as a reference. Such approaches need to be considered with caution as the catalyst (absorption) properties may be modified during reaction or treatment. However, strategies have been developed to account for the absorption-induced changes in Raman intensity.[27,28] The presence of resonance Raman or SERS effects may induce large changes in the Raman cross sections of the solids (adsorbates), which require their detailed description using theoretical approaches. Nowadays, such calculations are readily

performed on molecular systems serving as models for catalytic materials, and are expected to be expanded in the future to extended solids.

To date, Raman spectroscopy has been applied to a large range of catalyst materials, including bulk oxides, supported metal oxides, supported metal sulphides, molecular sieves, zeolites, bulk metals, supported metals, and heteropolyacids. There is a large number of older articles, reviews, and book chapters (up to the year 2010), that have extensively surveyed Raman studies related to heterogeneous catalysis, focusing on different classes of catalytic materials[29-31] and more specific advances in surface, adsorbate, or catalyst characterization.[20,27,32-64] In addition, since 2010 numerous reviews have addressed specific aspects of Raman spectroscopy in heterogeneous catalysis,[65-78] including resonance Raman spectroscopy,[65,79,72,73] Raman imaging,[67,68] SERS/TERS,[65,74,77] and *in situ/operando* Raman spectroscopy.[68-70,77] However, there has not been a general survey of the use of Raman spectroscopy in heterogeneous catalysis for a while. Triggered by exciting new findings and methodical aspects, this review gives an overview of major developments in the field during the past decade as well as an outlook on potential future directions. Throughout the review, the main focus will be on gas–solid catalytic reactions, but (photo)catalytic reactions in the liquid phase will be touched on if it appears appropriate.

First, I will briefly introduce some basic concepts of Raman spectroscopy and discuss experimental setups commonly employed for Raman studies in heterogeneous catalysis, highlighting methodical advances in UV and multi-wavelength Raman spectroscopy, nonlinear and surface (tip) enhanced Raman spectroscopy, and *in situ/operando* characterization (Section 2). In Section 3, the types of information nowadays available from Raman spectra will be summarized. The next sections will address ways of increasing the sensitivity of the Raman technique by fluorescence suppression, resonance and plasmon-induced enhancements (Section 4), and recent development regarding time-resolved (Section 5) and spatially-resolved (Section 6) experiments. Throughout the review I will illustrate major developments and

findings by representative literature examples mainly from the last decade, including *in situ/operando* studies in catalytic environments. In order to be of interest to a broad range of readers, this review is structured such that, on one hand, it is possible to obtain an updated view of the type of information available from Raman spectra in the context of catalytic materials (Section 3), while, on the other hand, Sections 4–6 focus on more specific topics related to developments in methods, thus providing a different perspective. Despite the unavoidable overlap of material, efforts have been made to allow each section to be read independently of the others.

## 2. Basic principle and instrumentation

### 2.1 Raman effect

Raman spectroscopy is based on the Raman effect, in which incident light is inelastically scattered from a sample and shifted in frequency by the energy of the excited molecular vibrations. As shown in Fig. 3a, when starting from the vibrational ground state, spontaneous scattering may give rise to a frequency redshift (Stokes scattering), whereas starting from an excited vibrational state, the incident photon may gain energy when scattered (anti-Stokes scattering). In general, Raman spectroscopy may also observe rotational or other low-frequency modes, but these are of no relevance in the context of the catalytic applications discussed here. Figure 3 provides an overview of Raman processes applied in the context of catalyst characterization. In the following, the focus will be on spontaneous and resonance Raman scattering, while nonlinear Raman spectroscopy (CARS) and processes based on surface-enhanced Raman scattering (SERS, SHINERS (shell-isolated nanoparticle enhanced Raman spectroscopy), TERS) will be discussed in Section 2.5.

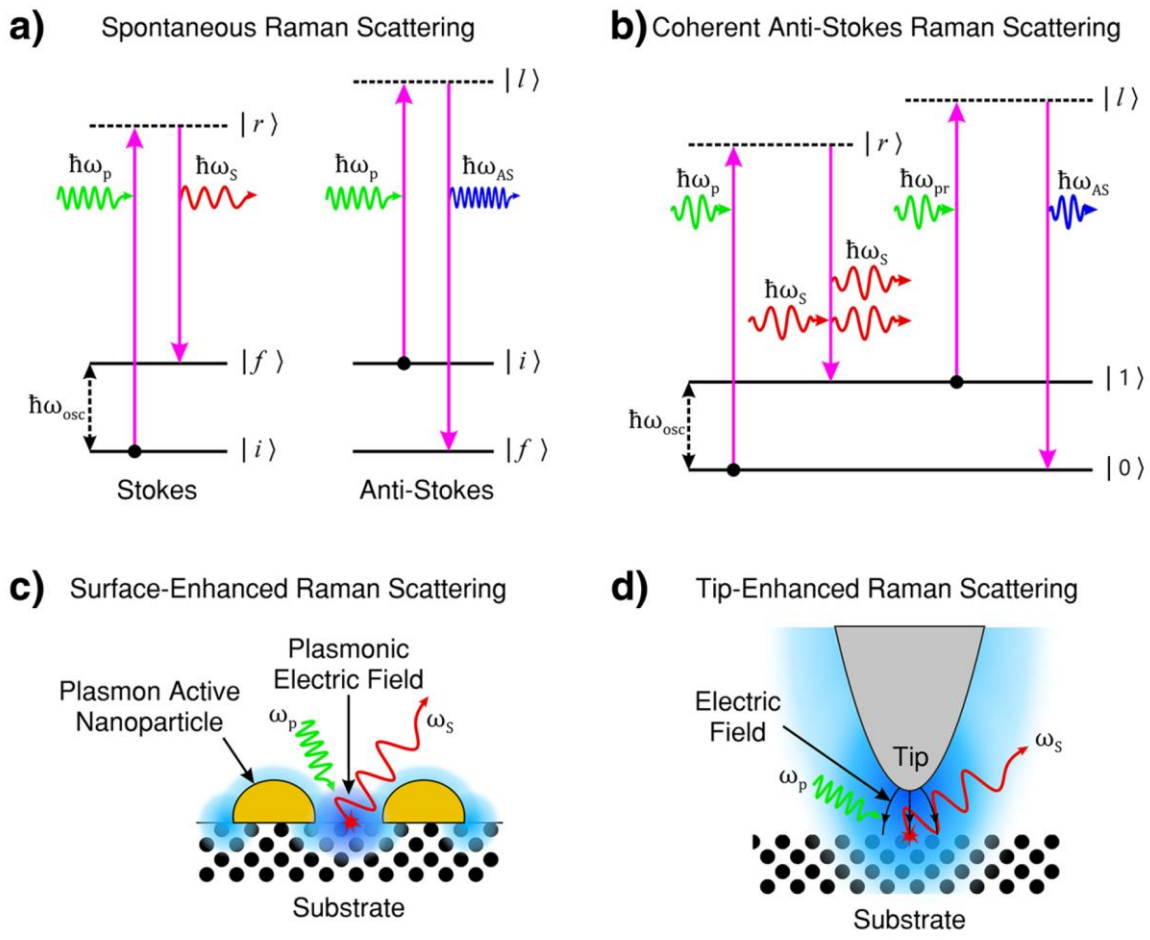


**Fig. 3** Vibrational Raman processes applied in the context of catalyst characterization. (**a)** Spontaneous Raman scattering is based on inelastic scattering of light leading to a frequency redshift (Stokes) or blueshift (anti-Stokes). (**b)** CARS is a four-wave mixing process based on the interaction of three laser beams with frequencies $\omega_p$ (pump), $\omega_S$ (Stokes), and $\omega_{pr}$ (probe), leading to the generation of a coherent signal at the anti-Stokes frequency $\omega_{AS}$. (**c)** In SERS the incident light may induce a surface plasmon excitation, resulting in an increase of the Raman scattered light due to electromagnetic enhancement. Besides, the coupling with the metal may increase the Raman cross section, leading to chemical enhancement. (**d)** In TERS, enhancement originates from surface plasmon excitation at a tip and is localized in the vicinity of the tip apex. Reproduced with permission from ref. 80, copyright 2019, Springer.

As a first estimate of the Raman intensity of solid samples, the scattering intensity $I$ of gas-phase molecules may be considered, which is proportional to the intensity $I_0$ and the fourth power of the frequency of the exciting radiation $\omega_p$:

$$I \sim I_0 \left(\omega_p - \Delta\omega\right)^4 \qquad (1)$$

Thus for normal (non-resonant) Raman spectroscopy, an increase of the incident intensity $I_0$ and excitation frequency $\omega_p$ leads to an increase in the Raman intensity. However, to reduce laser-induced heating effects $I_0$ needs to be limited by power reduction, defocusing or spreading the beam into a line by a cylindrical lens, for example. In addition, sample movement has been demonstrated to efficiently reduce the effect of the laser, as will be discussed below (see Section 2.3).

For solids, the penetration depth of vibrational Raman scattering, that is, the sampling depth of the technique, depends on the absorption properties and the wavelength of the excitation laser, and ranges typically from millimetres to nanometres.[81] Self-absorption may affect relative intensities and may therefore limit the capability of Raman spectroscopy for quantification. In this regard, the use of UV-vis spectroscopy is advisable, which may facilitate the interpretation of Raman spectra and allows intensity corrections.[28]

In most studies on catalyst materials, visible lasers are employed for excitation (e.g. 515, 532, 633 nm), mostly in combination with dispersive spectrometers and front/back-illuminated CCDs, allowing characterization of a wide range of materials. However, visible Raman spectroscopy is susceptible to fluorescence, giving rise to a Raman background. As the origin of the fluorescence background, molecules and ions (fluorophores), present as an impurity or part of the sample, as well as defects, excitons, and defect energy levels, have been proposed, as discussed by Kim *et al*.[65] Conventional Raman scattering is a non-resonant phenomenon (see Fig. 3); thus, on average, only one out of $10^8$ photons hitting the sample will be Raman scattered. In contrast, fluorescence is a resonant phenomenon. For example, in the presence of

an impurity at the ppm level with a fluorescent quantum yield of 0.1, ten fluorescent photons would be produced for every Raman photon. As a consequence, even for small impurity concentrations, fluorescence may dominate the spectrum. One major strategy to minimize the effect of fluorescence is to choose an excitation frequency $\nu_0$ that avoids fluorescence (e.g. in the NIR or UV), as will be described in more detail in Section 2.3 (see Fig. 7). In addition, variable laser excitation allows the Raman signal to be increased by exploiting resonance enhancements, that is, resonance Raman spectroscopy can be performed. The intensity of Raman scattering is proportional to $|\alpha_{\rho\sigma}|^2$, and the polarizability ($\alpha_{\rho\sigma}$) can be described according to the Kramers–Heisenberg equation (eq. 2):[82,65,72]

$$(\alpha_{\rho\sigma})_{fi} = \sum_{r \neq i,f} \left( \frac{\langle f|\mu_\rho|r\rangle\langle r|\mu_\sigma|i\rangle}{\Delta E_{ri} - \hbar\omega_p - i\Gamma_r} + \frac{\langle f|\mu_\sigma|r\rangle\langle r|\mu_\rho|i\rangle}{\Delta E_{rf} + \hbar\omega_p + i\Gamma_r} \right) \qquad (2)$$

In the equation, $\omega_p$ represents the frequency of the excitation laser, $\Delta E_{ri}$ the energy difference of the two electronic states i and r, and state f the first excited vibrational energy level. If the energy of the excitation laser ($\hbar\omega_p$) closely matches an electronic transition ($\Delta E_{ri}$), the polarizability ($\alpha_{\rho\sigma}$) is strongly enhanced. As a consequence of such a resonance Raman effect, the Raman intensity may increase by several orders of magnitude. As will be illustrated below, Raman bands related to different catalyst components can be selectively enhanced by excitation with different lasers according to their electronic transitions, making resonance Raman spectroscopy a powerful tool to characterize heterogeneous catalysts. Moreover, even species present as a minority of the catalyst material may be detected.

### 2.2 Raman spectrometers

The major components of Raman instrumentation comprise an excitation laser, a spectrometer, and a detector.[6] For applications in catalysis, mostly dispersive Raman spectrometers are applied, which use a diffraction grating to disperse the light scattered from a sample onto a

detector, e.g. a CCD (charge-coupled device) camera. In the past, different types of diffraction spectrometers have been employed for Raman studies: single-, double-, or triple-grating. Nowadays, for most catalytic applications, single-grating spectrometers are combined with a notch/edge filter for rejection of the Rayleigh light. This allows excellent optical throughput at low spectrometer complexity. On the other hand, the use of notch/edge filters is accompanied by a significant suppression of low Raman shifts of at least 100 $cm^{-1}$ (for a super notch filter). Lower Raman shifts are accessible using triple-grating spectrometers, however, at the expense of much lower optical throughput and significantly higher spectrometer complexity. A comparison of single- and triple-grating spectrometers for Raman studies is summarized in Table 1. Besides dispersive spectrometers, FT (Fourier-transform) Raman spectrometers can be employed for catalyst characterization. In FT Raman spectrometers, an interferometer introduces a path difference between the source signal and the signal beams, leading to an interference pattern, that is, an interferogram, which is used to construct the Raman spectrum. A comparison of the different Raman spectrometer systems can be found in Section 2.4.

**Table 1** Characteristics of dispersive spectrometers used for Raman studies in catalysis. As filters either notch or edge filters are employed.

| | **Single-grating + filter** | **Triple-grating** |
|---|---|---|
| **Rayleigh + stray light** | Good | Excellent |
| **Optical throughput** | Excellent | Moderate |
| **Low Raman shifts** | Limited | Excellent |
| **Discrete laser wavelengths** | With appropriate filter | Compatible |
| **Tuneable laser wavelengths** | Not compatible | Compatible |
| **Complexity** | Low | High |

## 2.3 UV Raman spectroscopy

In the past, the application of UV Raman spectroscopy for catalyst characterization was limited by sample degradation owing to heating and photochemical effects induced by the high-frequency laser excitation. However, these issues have been resolved, thus allowing the applications of UV Raman spectroscopy to be extended. In fact, over the past decade, there have been an increasing number of catalysis-related Raman studies using UV-laser excitation, as will be illustrated below. In the following, experimental UV Raman approaches will be discussed, as well as important developments in methods that allow the effect of laser irradiation to be avoided. Examples of applications of UV Raman spectroscopy in catalysis will be given in Section 4.1.

Early UV Raman sources were based on pulsed, low-frequency (10–20 Hz) Nd:YAG (neodymium-doped yttrium aluminium garnet) lasers with high peak power and frequency conversion of the 1064 nm emission into the UV.[83-85] To reduce the potential of sample degradation by high peak power, intracavity frequency doubling of continuous-wave (CW) $Ar^+$ and $Kr^+$ lasers has been applied,[86,87] leading to CW UV emission. In the context of catalytic applications, particularly the deep-UV 244 nm line from a frequency doubled $Ar^+$ laser[88-90] and 325 nm emission from a CW helium–cadmium (HeCd) laser[88,91,92,61] has been employed. In both cases, Rayleigh rejection can be achieved by single-grating spectrometers in combination with edge (notch) filters or by triple-grating spectrometers. In triple-grating spectrometers, the third stage functions as a spectrograph to disperse the Raman scattered light onto a UV-enhanced CCD or an imaging (2D) photomultiplier tube for detection. Recently, hollow cathode lasers as compact source of deep UV emission at 224.3 and 248.6 nm as well as the corresponding edge filters have become available.

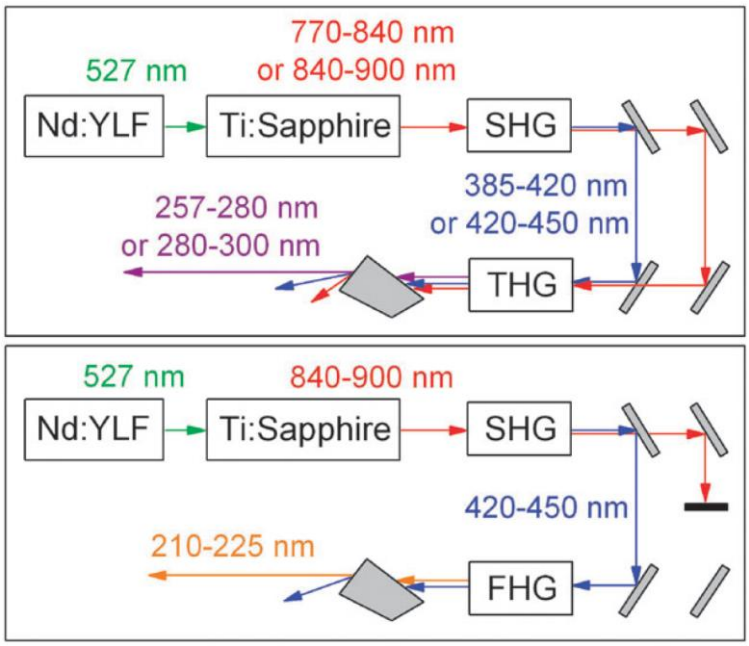


**Fig. 4** Wavelength-tuneable laser system for Raman spectroscopy in catalysis operated at Argonne National Laboratory and TU Darmstadt. The light emitted by a Nd:YLF-pumped tuneable Ti:Sa laser is converted into visible, near-UV, and deep-UV emission by second- (SHG), third- (THG), and fourth-harmonic generation (FHG) processes, respectively. Reproduced with permission from ref. 65, copyright 2010, Royal Society of Chemistry.

A new generation of UV laser systems is based on a solid-state, wavelength-tunable Ti:Sa-based laser, pumped, for example, by a frequency-doubled Nd:YLF (yttrium lithium fluoride) laser emitting at 527 nm.[93-96] Such laser systems are quasi-CW due to the high repetition rates (1–6 kHz) and long pulse durations (20–50 ns). Besides their overall stability, they are characterized by a low peak power and narrow laser bandwidth of <1 $cm^{-1}$ across the entire tuning range. Combined with a triple-grating spectrometer, they are ideally suited for Raman applications in catalysis as shown first by the Stair group and later by our own work.[65,97] For example, the Ti:Sa laser at Argonne National Laboratory and TU Darmstadt is continuously tuneable within the range 770–920 nm, and uses nonlinear BBO (beta barium borate) and LBO (lithium triborate) crystals to convert the NIR emission by second- (SHG), third- (THG), and

forth-harmonic generation (FHG) processes into continuously tuneable wavelengths in the deep UV (210–225 nm), near UV (257–300 nm), and visible regions (385–450 nm), respectively, as illustrated in Fig. 4.

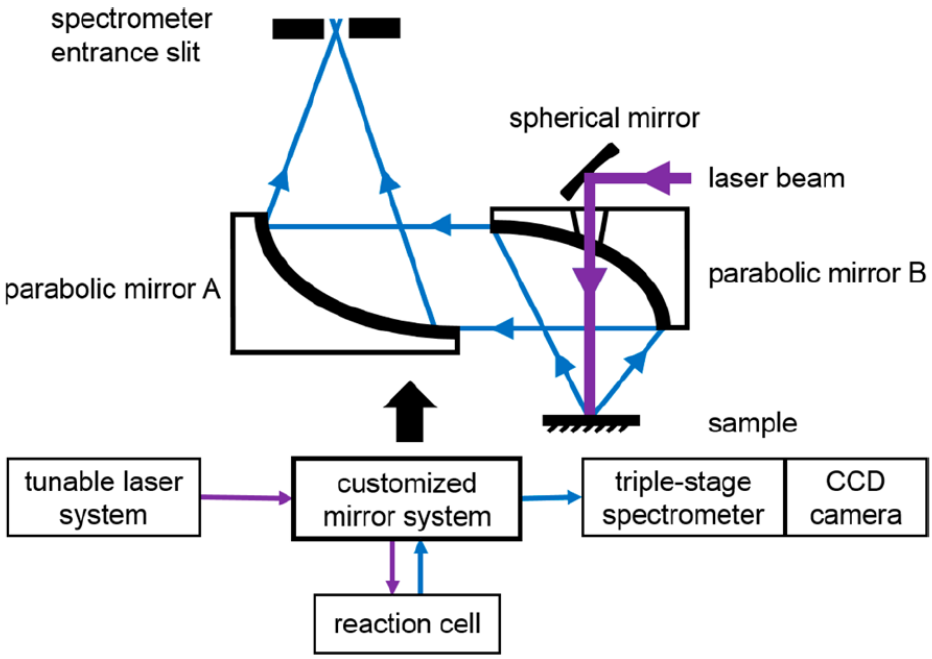


**Fig. 5** Scheme of a UV Raman experiment at TU Darmstadt combining beam expansion and efficient collection optics to reduce the effect of laser irradiation intensity. A spherical mirror focuses the laser radiation onto the catalyst, while the scattered radiation is collected using parabolic mirrors. Reproduced with permission from ref. 98, copyright 2016, American Chemistry Society.

An important aspect of UV Raman applications in catalysis has been the development of experimental approaches to avoid the effects of laser irradiation. One strategy is based on the reduction of the laser intensity by increasing the spot size of the laser on the sample. To avoid a loss of sensitivity in this case, efficient collection optics are required. Recently, a mirror system has been designed by Waleska *et al.*, which is based on 90° off-axis parabolic mirrors

A and B, as shown in Fig. 5.[98] A spherical mirror focuses the laser radiation through a hole in parabolic mirror B onto the sample (spot size: ~0.6 $mm^2$). This design allowed the researchers to realize a confocal setup with only three optical components and, besides that, to increase the overall sensitivity compared to a setup based on standard objectives. A UV Raman setup based on one 90° off-axis elliptical mirror has also been reported.[65]

A further strategy to avoid laser-induced effects is to reduce the interaction time between the laser beam and the sample by moving the sample. This can be achieved by placing the sample or Raman cell on an *xyz*-stage subject to continuous movement, for example.[98] Alternatively, a fluidized bed may be used to induce a homogeneous movement (fluidization) of the catalyst particles.[32,99-103] Figure 6 depicts a fluidized bed reactor for Raman experiments in catalysis, which was developed by modifying a commercial CCR1000 catalyst cell from Linkam Scientific Instruments.[101] The feed flows downwards from the top to the bottom of the microreactor, passing through the sample. For fluidization, pressure oscillations are induced reverse to the flow direction at about 40–100 Hz, lifting the particles intermediately upwards while keeping the net flow direction downwards, as illustrated in Fig. 6b.

In recent years, the applicability of the fluidized bed approach has been demonstrated not only for UV Raman studies,[101,102,104] but also for Raman studies on (light/heat)-sensitive catalyst materials in general.[103] Recently, the Linkam-based fluidized bed approach has been expanded to allow combined Raman and UV-vis analysis, also under *in situ/operando* conditions.[103]

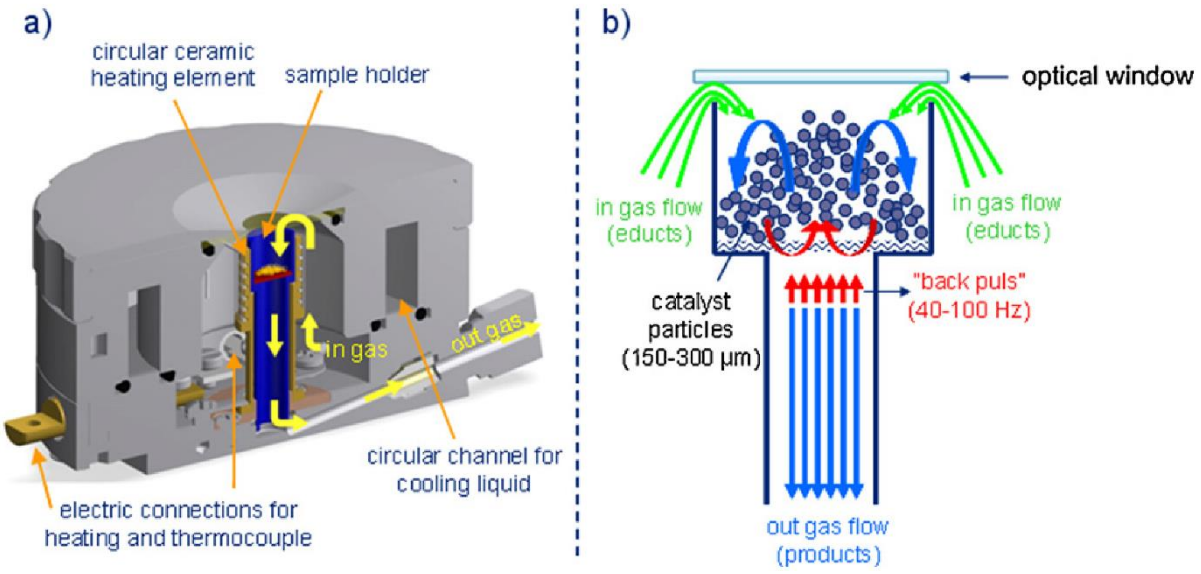


**Fig. 6** Fluidized bed reactor for Raman experiments in catalysis. **(a)** Detailed sketch of the microreactor. **(b)** Schematic drawing of the sample holder illustrating the fluidization principle. Reproduced with permission from ref. 101, copyright 2013, Elsevier.

Visible Raman spectroscopy can be widely applied to the characterization of catalysts, but it is susceptible to fluorescence problems that may even dominate the spectrum. For example, fluorescence is frequently observed with zeolites or compounds with similar framework structures, and sometimes in hydrocarbon environments. However, the fluorescence problem can be greatly reduced or even removed if an excitation wavelength in the UV or NIR region is chosen.[100,105,106,63,101,72] As illustrated in Fig. 7 for $AlPO_4$-5, in both cases the Stokes Raman range is shifted to a region not interfering with fluorescence, that means, in the UV this leads to Raman shifts appearing at shorter wavelengths than fluorescence, and in the NIR to Raman shifts appearing at longer wavelengths than fluorescence. However, in the UV, the Raman signal further benefits from the increased scattering intensity (see eq. 1).

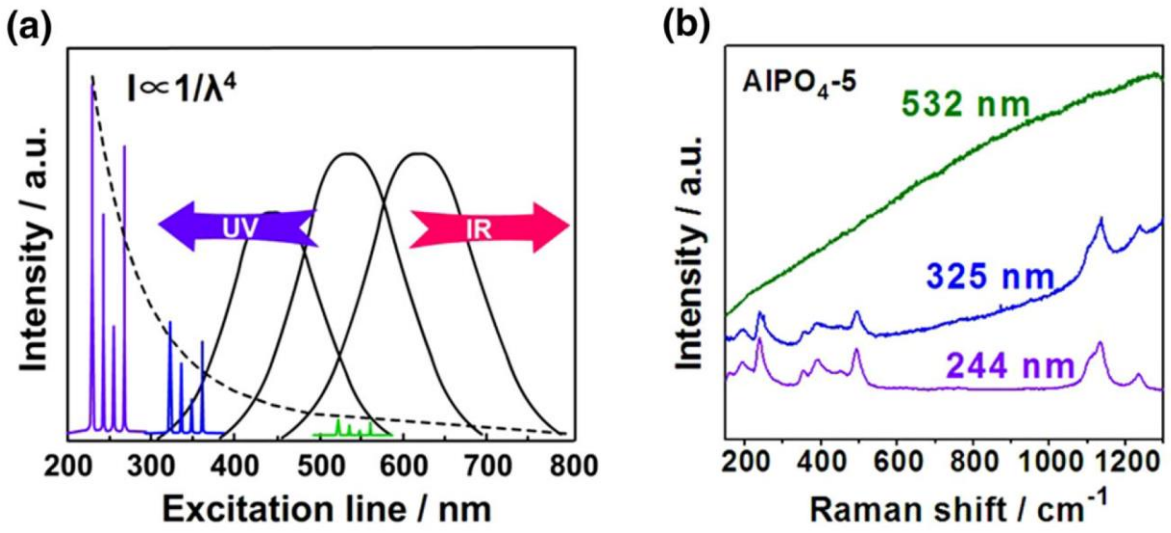


**Fig. 7** Avoidance of fluorescence problems of Raman spectroscopy in catalysis. **(a)** The choice of UV or NIR excitation shifts the Stokes Raman range out of the region of fluorescence. **(b)** Raman spectra of aluminium phosphate $AlPO_4$-5 at 244, 325, and 532 nm excitation. Modified with permission from ref. 72, copyright 2015, Springer.

### 2.4 Comparison of Raman spectrometer systems

For the characterization of heterogeneous catalysts, two fundamentally different types of Raman spectrometer systems have been employed, based on either dispersive or FT spectrometers, with a pronounced preference for dispersive spectrometers. Among the systems with dispersive spectrometers, the use of laser excitation wavelengths in the visible (visible Raman: 400–700 nm) are most common, followed by a much lower but increasing number of studies with excitation in the UV (UV Raman: 200–370 nm), and an even smaller number of NIR studies (NIR Raman: typically 785 nm). FT Raman spectrometers, developed to reject fluorescence, which is encountered in many (industrial) samples, use NIR laser excitation (750–1100 nm), in particular the emission of (fluctuation-noise-free) Nd:YAG and Nd:YLF lasers at 1064 nm and 1054 nm, respectively.[107,108] According to eq. 1, there is a significant decrease in the Raman intensity on moving from visible to NIR excitation. For example, going from

515 nm to 1064 nm laser wavelength leads to an intensity loss of a factor of ~16. However, the decrease in Raman signal can in principle be compensated by higher laser irradiation because, in the NIR region, sample absorption of many catalyst samples is minimized and high laser powers can be employed, with a lower risk of absorption-induced sample damage. On the other hand, studies at even moderate temperatures (~200°C) may be limited by blackbody radiation, which is much stronger in the NIR than in the visible or UV.[109] Besides thermal emission, (traces of) transition metal ions, for instance iron (present in the sample or in used glassware), may give rise to a broad background signal.[109] Note that the above arguments hold not only for FT Raman, but also for dispersive Raman measurements using NIR excitation. However, to this end, the use of smaller NIR wavelengths (e.g. 785 nm) may reduce some of the limitations and even allow *operando* studies and the exploitation of resonance Raman effects.[110] As discussed in detail in the previous section, fluorescence may also be successfully circumvented by the use of UV laser excitation, provided the laser intensity can be reduced, for example by sample movement. As becomes apparent from the above discussion, each Raman spectrometer system exhibits advantages and disadvantages for different types of heterogeneous catalysts, that is, each catalyst material may show its optimum spectrum with a different Raman spectrometer system.

Shortcomings of single-wavelength Raman spectroscopy can be overcome by employing multiple laser excitation wavelengths. Such an approach, while experimentally more demanding, may significantly expand the applicability of Raman spectroscopy to catalytic studies, explicitly including industrial samples. Besides improvements in general applicability and Raman intensity, the use of different laser lines offers further advantages, such as facilitated (defect) structural analysis by targeted enhancement of specific Raman bands, molecular parameters (anharmonicity, dissociation energy, etc.), and/or information on the presence of resonances, electronically excited states, and electronic transitions, as will be illustrated in

Sections 3 and 4. Multi-wavelength Raman spectroscopy has been successfully implemented in the context of catalyst characterization, for example by use of separate lasers sources with different excitation wavelengths (e.g. 325, 532, and 633 nm),[61,88,111-115,104] lasers that offer different emission lines or can be frequency-converted (e.g. $Ar^+$ laser),[116,89,117,118] or wavelength-tuneable laser systems (preferably) providing access to UV, UV-vis, and NIR excitations, as described above (see Fig. 4).[119,65,97,120,121,104]

### 2.5 Raman spectroscopy based on nonlinear and surface-enhanced processes (CARS, SRS, SERS, SHINERS, TERS)

In conventional (linear) optics, the induced polarization depends linearly on the electric field strength, which can be described by the first term of eq. 3, where the constant of proportionality $\chi^{(1)}$ is known as the linear susceptibility of the material (rank one tensor) and $\varepsilon_0$ is the permittivity of free space:[122,123]

$$P_j = \varepsilon_0 \left[ \chi_{jk}^{(1)} E_k + \chi_{jkl}^{(2)} E_k E_l + \chi_{jklm}^{(3)} E_k E_l E_m + \cdots \right] \qquad (3)$$

The linear polarization is the basis of spontaneous (linear) Raman spectroscopy, which is characterized by a single-photon scattering process (two-wave mixing process), as illustrated in Fig. 3a.[80] In nonlinear Raman scattering, more than two waves need to be considered in wave-mixing processes, and the nonlinear polarization depends on the products of the mixed electric field components. The corresponding susceptibilities for the second- and third-order processes are $\chi^{(2)}$, the second-order susceptibility (rank three tensor), and $\chi^{(3)}$, the third-order susceptibility (rank four tensor). $\chi^{(2)}$ vanishes for liquids, gases, amorphous solids and many crystals displaying inversion symmetry, whereas $\chi^{(3)}$ can occur for both centrosymmetric and non-centrosymmetric media.[122] As illustrated in Fig. 3b, coherent anti-Stokes Raman scattering (CARS) is a third-order nonlinear four-wave mixing process based on the interaction of three

laser beams with frequencies $\omega_p$ (pump), $\omega_S$ (Stokes), and $\omega_{pr}$ (probe), leading to the generation of a coherent signal at the anti-Stokes frequency $\omega_{AS}$. In particular, the frequency difference ($\omega_p - \omega_S$) needs to match the frequency associated with the Raman active mode $\omega_{osc} = \omega_p - \omega_S$, which is usually achieved by tuning the frequency of the Stokes beam.[124] The probe photon ($\omega_{pr}$) then induces the anti-Stokes scattering process, which for $\omega_{pr} = \omega_p$ occurs at frequency $\omega_{AS} = 2\omega_p - \omega_S$. Instrumentation for CARS (microscopy) has been reviewed by Kano *et al.*[125] and Jones *et al.*[80] While the instrumentation is significantly more complex than for spontaneous Raman scattering, CARS has a number of advantages, such as fluorescence suppression, high spatial resolution, and access to different types of polarization measurments.[125]

Stimulated Raman scattering (SRS) is another third-order nonlinear four-wave mixing process based on the interaction of two laser beams with frequencies $\omega_p$ (pump) and $\omega_S$ (Stokes). If the frequency difference ($\omega_p - \omega_S$) matches the frequency of the Raman active mode $\omega_{osc} = \omega_p - \omega_S$, stimulated excitation of the vibrational transition occurs.[80] Emission is usually achieved by tuning the frequency of the Stokes beam. Note that there is no signal at frequencies different than those of the excitation sources. In contrast to CARS, SRS provides a signal that is free from a non-resonant background, allowing straightforward data analysis.

As illustrated in Fig. 3c, the sensitivity of Raman spectroscopy can be strongly enhanced if molecules are attached to rough metallic nanostructures exhibiting surface plasmon excitations, which is known as surface-enhanced Raman spectroscopy (SERS).[126-130] In the context of catalytic applications, SERS is of particular interest owing to its high local sensitivity, which allows surface species and adsorbates to be monitored.[131-133] In the past, strong sensitivity enhancements have only been observed with Ag, Au, and Cu, and, even with these SERS-active metals, a surface morphology with roughness on the nanometre scale is crucial for large enhancements.[131,134] Such noble metallic nanostructures are not benign, because, based on surface plasmon excitation, they may lead to interference with the catalytic reaction by generating heat, supplying energetic ('hot') electrons, and/or providing strong local

electromagnetic fields.[135,74,136] These limitations have been successfully overcome by coating Au or Ag nanoparticles with thin shells, just a few nanometres thick, of chemically inert oxides ($SiO_2$, $Al_2O_3$, etc.), referred to as shell-isolated nanoparticle-enhanced Raman spectroscopy (SHINERS).[137,138] Thus, in these core–shell systems, the noble metal core provides large enhancement of the Raman signals of the nearby molecules, and the inert shell isolates the metal nanoparticle from the environment. Figure 8 provides an overview of different types of nanoparticles used as SERS substrates,[138] focusing on spheres, although other shapes, such as rods[134] and cubes,[139] may also be employed. Applications of SERS and SHINERS in the context of heterogeneous catalysis will be discussed in Sections 4 and 5.

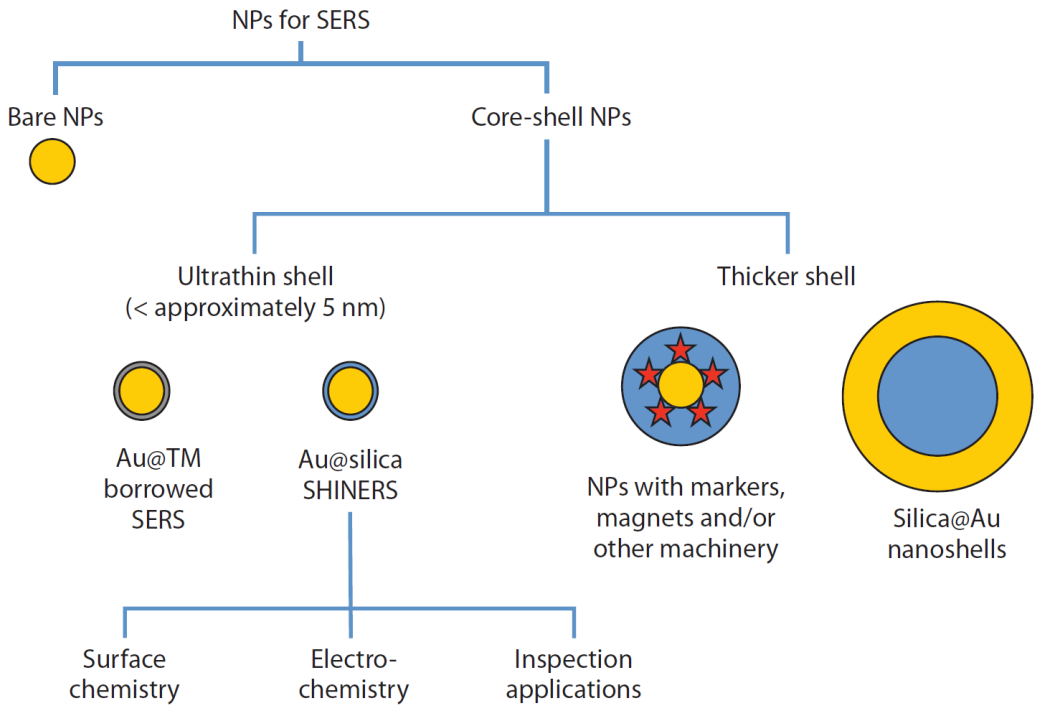


**Fig. 8** Core–shell nanoparticles (NPs) and shell-isolated nanoparticle-enhanced Raman spectroscopy (SHINERS). Abbreviations: SERS, surface-enhanced Raman spectroscopy; TM, transition metal. Reproduced with permission from ref. 138, copyright 2013, Annual Reviews.

More recently, photo-induced enhanced Raman spectroscopy (PIERS) has been developed, which employs a photo-activated semiconductor substrate to give additional chemical enhancements as compared to SERS, and which has been proposed to be based on surface oxygen vacancies ($V$o) formed upon substrate pre-irradiation.[140,141]

As a variation of SERS, tip-enhanced Raman spectroscopy (TERS) has developed into a promising technique for the *in situ* characterization of heterogeneous catalysts, combining high sensitivity and spatial resolution with chemical information. Whereas in SERS enhancement arises from the substrate, the TERS enhancement originates from a metallic scanning probe microscopy (SPM) tip, as illustrated in Fig. 3d.[80,142] For the tip material, Ag and Au are most commonly used, in combination with excitation wavelengths in the green or red, while typical setups are based on atomic force microscopy (AFM) or scanning tunnelling microscopy (STM) feedback mechanisms.[143] There are different ways of producing TERS tips, for instance by electrochemical etching from a full metal wire, by metal coating of an atomic force microscopy (AFM) cantilever, or by more complicated procedures.[143] A great challenge in TERS is the fabrication of tips that are stable and reproducible and allow large enhancements. Despite the potential of TERS for *in situ* analysis, there are only a few studies related to heterogeneous catalysts.[144-151] SERS and TERS instrumentation has recently been reviewed by Jones *et al.*[80] Applications and very recent developments of TERS for (spatially resolved) analysis catalytic processes will be discussed in Sections 5 and 6.

### 2.6 *In situ/operando* Raman cells for gas–solid catalytic reactions

As catalysts may change their structure under reaction conditions, the development and application of *in situ/operando* techniques is essential to unravel their structure–activity relations. In general, when using *in situ* spectroscopy, catalyst materials are investigated as a function of temperature, pressure, and/or gas atmosphere. For cases in which the spectroscopic experiment is performed simultaneously with the measurement of the function of the material

(e.g. activity of catalyst), that is, the spectroscopy is performed under working conditions of the functional material, the term *operando* spectroscopy has been used.[152]

The application of *in situ/operando* Raman spectroscopy to catalytic materials has attracted a great deal of attention, particularly because of its sensitivity to the catalyst structure and its dynamics both in the bulk and at the surface, the (typically) small interference of gas-phase signals (e.g. $H_2O$, $CO_2$), its applicability within a wide range of temperatures (~25–1000°C) and pressures (~0.1–10.0 MPa), and the possibility of designing *in situ/operando* cells resembling typical plug flow reactors. The use of *operando* Raman spectroscopy in catalytic studies has been reviewed previously,[64,68,70,153] and more recent examples will be given throughout this review. In the past, different designs of *operando* Raman cells have been introduced, based on a rotating sample cell,[154,155] a stationary quartz cell,[156] a rotating lens cell,[157,158] a fluidized bed reaction cell,[100,159] a fixed bed reaction cell,[160] and a stationary FT Raman cell,[161] as well as sub-versions of these cells, as described in more detail in a recent review by Bravo-Suarez and Srinivasan.[162] The kinetic appropriateness of *operando* Raman spectroscopic cells has been critically discussed by Meunier.[163] A comparison of activity data obtained in a traditional reactor and an *operando* Raman cell, based on a fixed bed custom-built quartz reactor, has been described by Banares and Khatib.[164]

In the following, relatively recent developments in the design of *in situ/operando* Raman cells for catalyst characterization will be discussed. In 2013, Beato *et al.* introduced a fluidized bed reactor and demonstrated its use for *operando* Raman experiments in zeolite catalysis (see Fig. 6).[101] As described above, a commercial CCR1000 catalyst cell from Linkam Scientific Instruments was modified to allow homogeneous fluidization of catalyst particles, thus removing the influence of laser heating. Geske *et al.* described the design of a fixed bed tubular reactor with a quartz capillary running though the catalyst bed, allowing spatially resolved kinetic and spectroscopic profiles to be recorded (see Fig. 9). A sampling orifice in the capillary supplies a small fraction of the reacting gas mixture to a mass spectrometer, while for spatially

resolved Raman analysis the temperature probe is replaced by an optical fibre sensor. The capabilities of the reactor were demonstrated for the oxidative dehydrogenation of ethane to ethylene on a $MoO_3$-$Al_2O_3$ catalyst and will be described below (see Fig. 28).[165] Maghsoumi *et al.* reported on a novel *operando* Raman annular reactor for catalytic experiments under kinetically limiting reaction conditions and its application to the dry reforming and partial oxidation of methane over Rh catalysts.[166] A new monolithic reactor for *operando* Raman studies on honeycomb-shaped catalysts has been developed by Rasmussen *et al.* and tested in the context of the propane ammoxidation over alumina-supported vanadium phosphorus oxide phases.[167] Domènech-Ferrer *et al.* introduced an *in situ* Raman cell for high pressure (up to 200 bar) and temperature (up to 400°C) hydrogen applications.[168] Finally, an *operando* micro flow cell for industrially relevant catalytic conditions of up to 500 bar and 400°C was presented by Reymond and Rudolf von Rohr and applied to $CO_2$ hydrogenation over a commercial $Cu/ZnO/Al_2O_3$ catalyst.[169] The cell is based on a stainless steel body and a flat sapphire window, and possesses a wide optical opening to allow spatially resolved Raman spectroscopic analysis.

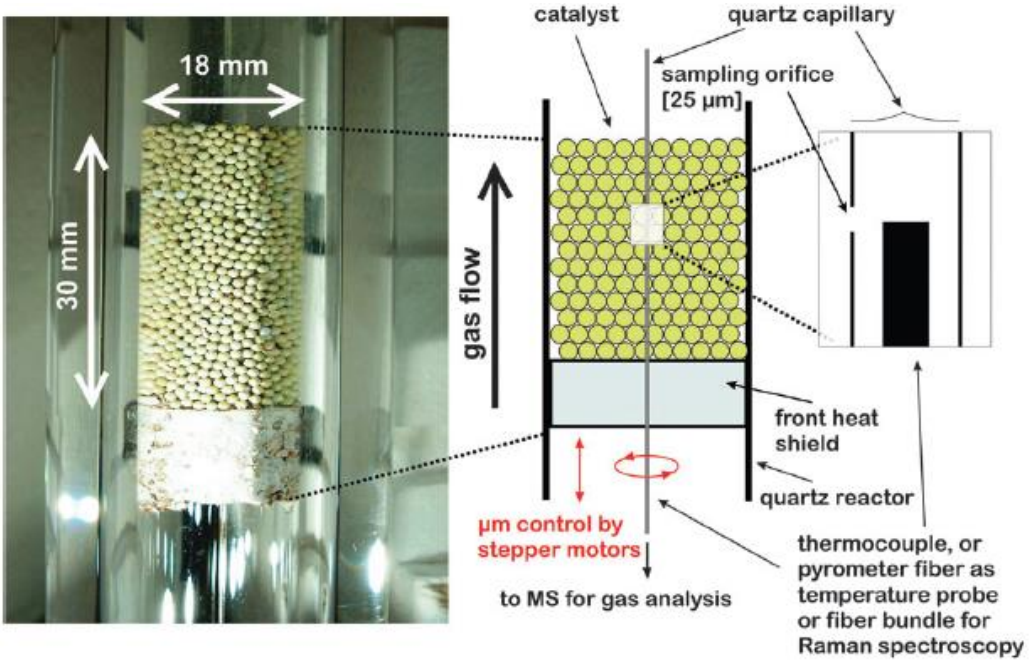

**Fig. 9** Experimental setup for simultaneous measurement of kinetic and spectroscopic profiles through a fixed bed tubular reactor. **Left** Image of the catalyst bed of γ-alumina spheres loaded with nominally 50 wt% $MoO_3$. **Right** Schematic diagram, including an enlarged area, of the probe geometry. Abbreviation: MS, mass spectrometer. Reproduced with permission from ref. 165, copyright 2013, Royal Society of Chemistry.

## 3. Type of information available from Raman spectra

The properties of heterogeneous catalysts depend on a variety of aspects, such as composition, geometric and electronic structure, particle size, defects, adsorbates, and surface functional groups. Raman spectroscopy has been shown to provide important information about bulk and surface properties of catalyst materials, including local and extended structure (crystal, amorphous, defect), surface species, and impurities. In the following, I will discuss the type of information available from Raman spectra, focusing on more-recent experimental and theoretical developments.

### 3.1 Structural characterization of solids

Raman spectroscopy has been a valuable tool for identifying the structure of bulk solids relevant to catalysis such as binary solids, multicomponent materials, zeolites, and other crystalline porous materials. It is well known from solid state spectroscopy that optical techniques allow only zone-centre optical phonons to be observed in single crystals. However, this $q \approx 0$ selection rule may be relaxed in the presence of defects or due to the interruption of the lattice periodicity in small crystallites, leading to the appearance of additional vibrational modes. Such a phonon confinement in a nanocrystal may modify the position and shape of vibrational bands, as has been demonstrated in the literature for a variety of metal oxide

nanoparticles (e.g. $CeO_2$, ZnO, $TiO_2$),[170-172] and specific surface contributions may arise, as observed for $ZrO_2$ and $SnO_2$ nanoparticles <15 nm.[173,174]

Although these effects are expected to become significant in nanocrystals as a result of the large surface-to-volume ratio, spectra of nanoparticles often still show a strong resemblance to those of the corresponding single crystals, allowing structural identification. In general, the structural analysis of a bulk solid may be facilitated by the application of group theory.

***Binary oxides.*** Binary oxides, such as alumina, silica, titania, or zirconia, have been widely used as catalyst support materials. Raman spectra allow different polymorphs of alumina (α, γ, δ) and silica to be distinguished, and also the anatase and rutile modifications of titania, and monoclinic and tetragonal zirconia.[175,30] Besides, solid–solid phase transitions have been characterized (transition order, transition temperature, transition pressure) for a number of binary oxides, including nanoparticles,[30,170,176] for example $TiO_2$. While the temperature-induced anatase-to-rutile transformation has been known for a long time,[177,178] $TiO_2$ may also undergo structural changes from anatase to rutile when the diameter of the gas-phase cluster source is decreased to below 5 nm,[179] or from anatase to Magnéli or (reduced) rutile phases in the presence of Au nanoparticles in $Au/TiO_2$ catalysts, as shown more recently.[180] A detailed UV Raman analysis of the size-dependent (7–300 nm) anatase-to-rutile phase transformation has revealed a decrease of transformation temperature with decreasing initial particle size,[181] while a novel approach for quantitatively measuring the percentage of exposed (001) facets in anatase $TiO_2$ has been introduced based on the relative intensity ratio of the $E_g$ and $A_{1g}$ peaks when using 488 nm excitation.[182]

Ceria is a widely used catalyst or support because of its redox properties.[78,104] Recently, there has been major progress in the Raman characterization of the ceria (defect) structure, including the identification of the Ce–O surface modes at around 250 $cm^{-1}$ (longitudinal phonon) and 400 $cm^{-1}$ (transversal phonon), the refined analysis of the profile of the $F_{2g}$ band,

and the relation of features in the defect region within 450–600 $cm^{-1}$ to structural motifs, as described below.[183,184]

Vanadium oxides have received continuous attention because of their applications in heterogeneous catalysis. Very recently, Shvets *et al.* reviewed the 21 binary vanadium oxide phases identified by using Raman spectroscopy so far, including films prepared by arc sputtering, such as α- and β-vanadium, $V_{14}O_6$, VO, $V_2O_3$, $V_3O_5$, several phases of $VO_2$, $V_6O_{13}$, $V_3O_7$, and $V_2O_5$.[185]

For some time, the synthesis and catalytic application of shaped nanoparticles has been the subject of intense research,[186] and Raman spectroscopy has been shown to be a valuable tool for the structural characterization of oxide nanoparticles with different surface facets, including ceria[187,188] and titania,[189] as described in more detail below in the context of adsorbate characterization (Section 3.3).

***Porous materials.*** Raman spectroscopy is a powerful technique to characterize the synthesis and particularly framework structural properties of microporous and mesoporous materials.[79,190,191,73] Difficulties arising from fluorescence interference from coke-like species, organic template impurities, or defects may be overcome by oxidative treatments, the use of laser excitation wavelengths avoiding fluorescence (typically 300–700 nm), for example in the UV, and/or sample movement.[72,73,101,102] Regarding acidic zeolites, dealumination, that is, Al leaching from the framework accompanied by loss of Brønsted acidity, is considered the main cause of deactivation. In MFI zeolites, an Al framework-related Raman signal at 745 $cm^{-1}$ has been identified that is sensitive to Brønsted sites and may therefore represent an useful indicator for steaming and/or dealumination processes in acidic zeolites.[192] Application of 3D Raman spectroscopy (at 532 nm excitation) to large zeolite ZSM-5 crystals after steaming has revealed the introduction of additional heterogeneities into the zeolite framework, migration of Al, and the formation of extra-framework Al species.[193] Very recently, dealuminated mordenite zeolites have been characterized using SRS microspectroscopy besides SEM and confocal fluorescence

microscopy showing a nonstraightforward correlation between acidity and activity, as will be discussed in more detail in Section 6.[194]

Transition metal–containing microporous and mesoporous materials such as TS-1, Ti-MCM-41 and Fe-ZSM-5 are of interest for catalytic oxidation processes. Despite the low concentration of the transition metals (<2%), Raman spectra enable characterization of framework transition metal ions by exploiting UV charge transfer transitions between the framework oxygen ion and the framework transition metal ion, for example in TS-1, Fe-ZSM-5, and V-MCM-41.[72] For instance, in TS-1 zeolite, two types of framework titanium species have been identified by UV Raman spectroscopy: titanium with tetrahedral '$TiO_4$' (1125 $cm^{-1}$, $\lambda$ = 244 nm) and octahedral '$TiO_6$' (695 $cm^{-1}$, $\lambda$ = 266 nm) coordination,[195] as will be also be discussed in Section 4.1.

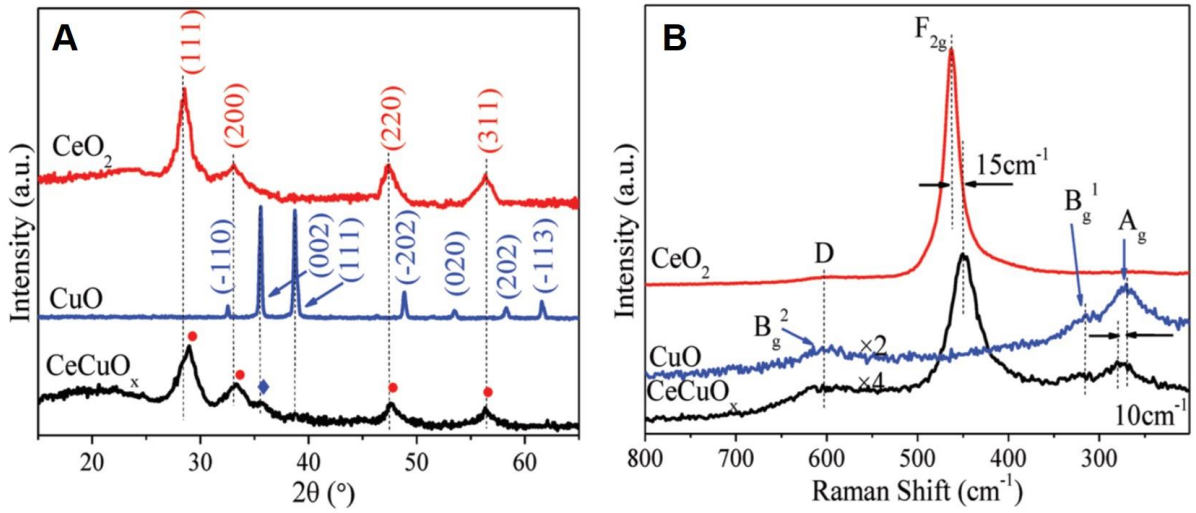


**Fig. 10** Structural analysis of $CeO_2$, CuO, and MOF-derived $CeCuO_x$. **(A)** XRD patterns. **(B)** Raman spectra at 515 nm excitation. Modified with permission from ref. 196, copyright 2020, Wiley-VCH.

Very recently, Wang *et al.* employed bimetallic metal–organic frameworks (MOFs) as a catalyst precursor for the synthesis of oxidation catalysts for volatile organic compounds

(VOCs).[196] First, a pure bimetallic MOF containing the target metals copper and cerium and organic ligands (i.e., dianions derived from 1,4-benzenedicarboxylic acid ($H_2BDC$)) was prepared, followed by its transformation into the mixed metal oxide $CeCuO_x$ by thermal treatment. Figure 10 depicts structural analysis data using X-ray diffraction (XRD, **A**) and visible Raman spectroscopy (**B**) that strongly indicates an aliovalent substitution of copper into the ceria lattice.[196]

***Supported metal oxides.*** Raman spectroscopy has been widely applied to supported metal oxide catalysts, which are relevant for applications and may serve as model catalytic systems.[75] Progress in structural characterization using Raman spectroscopy has been made on supported vanadium oxide systems, using silica,[197,89,88,198,115,120,98,121,199,200] alumina,[201-203,200] titania,[204] or ceria[111,205,104] as the support, by exploiting UV and visible excitation wavelengths, and by use of visible Raman spectroscopy on titania,[206-208] bilayered $TiO_2$-$SiO_2$,[209] niobia,[210] zirconia,[203] or carbon[211] support materials, as well as on $Mg_6Al_2(OH)_{16}(CO_3)\cdot n(H_2O)$ hydrotalcite.[212] Some of these developments will be discussed in more detail in the following.

Regarding the structure of dispersed vanadium oxide on silica, Molinari and Wachs excluded the presence of monomeric species with peroxo-oxo (umbrella) structure based on a comparison with the Raman spectrum of the well-known vanadium peroxo-oxo complex K[$VO(O_2)$(heida)], chelated with heida = *N*-(2-hydroxyethyl)iminodiacetic acid,[213,214] whereas the presence of oligomeric species was indicated by wavelength-variable Raman analysis and theoretical calculations (see also Section 3.4).[120,98,199,121] For titania-supported vanadium oxide, studies by Lewandowska *et al.* demonstrated the important role of water content and temperature, which influence the structure via V–OH formation and affect the position of the vanadyl.[206,207] Recently, an atomic layer deposition (ALD)-assisted approach to synthesising embedded vanadium oxide catalysts was introduced, which allows dispersed vanadium oxide

(in $Al_2O_3$, $SiO_2$, $TiO_2$) even at high vanadium loadings, as demonstrated by UV (256.7 nm) and visible (532 nm) Raman spectra.[200] The application of UV excitation at 256.7 nm provided detailed insight into the crystal structure and vanadium oxide structure of hierarchical $VO_x(WO_3)/TiO_2/SiO_2$ catalysts for ammonia selective catalytic reduction (SCR) based on monodisperse $SiO_2$ particles $TiO_2$-coated by ALD.[204] Ammonia SCR catalysts based on titania-supported vanadium oxides were recently investigated by modulation excitation Raman spectroscopy, revealing the dynamic role of both vanadium oxide and titania, as will be discussed in more detail in Section 5.3.[208] In the context of vanadium phosphate (VPO) catalysts, *operando* Raman spectra on alumina-supported VPO have revealed that no crystalline VPO phases are necessary for acrylonitrile formation in the propane ammoxidation reaction.[215]

Regarding alumina- and silica-supported vanadium oxide, it should be mentioned that UV resonance Raman spectra contain overtones of V=O stretching vibrations,[119,88] which the authors used to extract anharmonicity constants, a procedure that has been critically discussed by Stiegman.[216]

Raman spectra have provided valuable insight into the structure of supported molybdenum oxide.[217-223] Progress regarding the vibrational properties of $MoO_x$ sites on alumina, zirconia, titania, and silica has been critically discussed by Tsilomelekis and Boghosian.[217] Accordingly, the mono-oxo configuration (i.e., containing one Mo=O bond) appears to represent the majority $(MoO_x)_n$ species for γ-$Al_2O_3$, m-$ZrO_2$, and $TiO_2$ anatase supports, while the detailed coordination (i.e., four-fold vs. five-fold, degree of oligomerization) varies, depending on the coverage and/or support.[223]

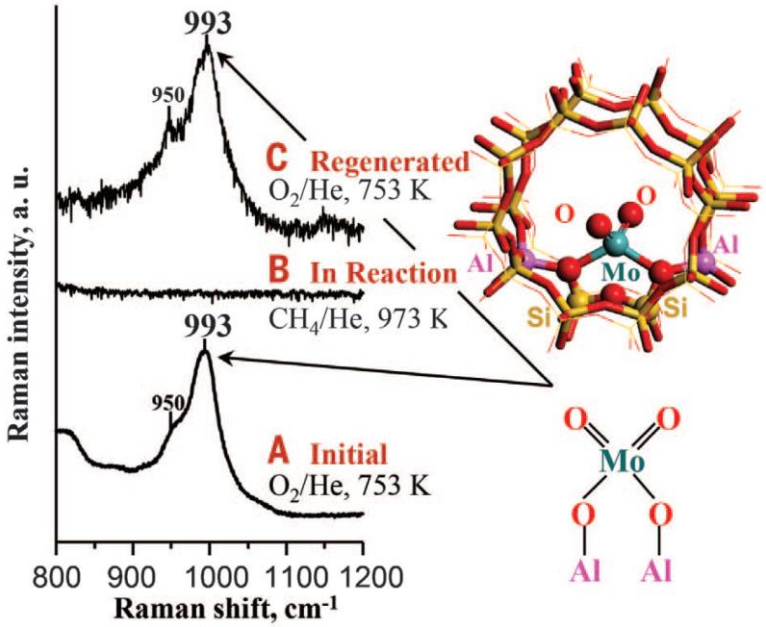


**Fig. 11** Raman spectra (442 nm) of zeolite 2 wt% Mo/ZSM-5 **(A)** after initial pretreatment in $O_2$/He at 480°C, **(B)** during reaction in $CH_4$/He at 700°C, and **(C)** after regeneration in $O_2$/He at 480°C. On the right, the structure of the proposed molybdenum oxide dioxo species is shown. Modified with permission from ref. 222, copyright 2015, American Association for the Advancement of Science.

In the case of silica supports, the presence of dioxo species in the $(O=)_2Mo(–O–Si)_2$ configuration in the majority of cases, and mono-oxo species in the $O=Mo(–O–Si)_4$ configuration in a minority of cases, has been proposed,[217] as well as the presence of both monomeric and oligomeric units with Mo coordination number values of 4 and 6.[219-221] More recently, Gao *et al.* studied molybdenum oxide supported on ZSM-5 (Si/Al = 15) zeolites used for natural gas conversion to benzene.[222] Figure 11 shows *operando* Raman spectra of 2 wt% Mo/ZSM-5 (Si/Al = 15) at 442 nm excitation after initial preteatment in oxygen (A), during reaction in $CH_4$/He at 700°C (B), and after regeneration with oxygen (C). Initially, the Raman spectrum is dominated by a band at 993 $cm^{-1}$, which is attributed to dioxo species anchored

onto double Al-atom framework sites. The disappearance of the Raman signal during reaction is the result of molybdenum oxide reduction to oxycarbide and carbide species, as confirmed by X-ray absorption fine structure and $Mo^{95}$ NMR. Under these conditions, the catalyst performed methane dehydroaromatization to benzene as the main hydrocarbon product.

In the context of supported transition metal oxides for olefin metathesis, Raman spectra have provided structural insight into alumina-supported rhenium oxide catalysts, revealing two surface dioxo $(O=)_2ReO_2$ species,[224] and into silica-supported tungsten oxide, showing the presence of dioxo $(O=)_2WO_2$ and mono-oxo $O=WO_4$ surface sites.[225] Different mono-oxo $O=WO_4$ sites have also been identified on titania.[226] Using UV Raman spectroscopy at 244 nm excitation, Ding *et al.* studied silica-supported molybdenum oxide catalysts and observed a resonance enhancement of dioxo $Mo(=O)_2$ species.[218] In combination with electron microscopy the authors proposed the active sites for olefin metathesis to be derived from monomeric dioxo species.

Using $CrO_x/SiO_2$ catalysts for ethylene polymerization, Chakrabarti *et al.* observed the presence of two distinct surface chromia species prior to reaction using 442 nm Raman spectra, namely dioxo $(O=)_2CrO_2$ in tetrahedral coordination and mono-oxo $O=CrO_4$ in a distorted square pyramidal coordination, which under reaction conditions decreased in intensity due to reduction of $CrO_x^{6+}$ sites to $Cr^{3+}$ to form $Cr–(CH_2)_2CH=CH_2$ and $Cr–CH=CH_2$ reaction intermediates, as indicated by IR spectroscopy.[227]

The structure of highly dispersed $TiO_x$ species on silica SBA-15 has recently been investigated by Nitsche and Hess over a wide range of Ti loadings (0.001–0.7 Ti/nm$^2$) using UV Raman spectroscopy at 217.5 nm excitation.[120] At very low loadings (<0.05 Ti/nm$^2$) the structure of titania is characterized by tetrahedral coordination of the central atom and anchoring to the support by one or more M−O−S linkages, whereas at higher loadings, titania partly forms oligomeric surface structures.

***Supported metals.*** While noble metal species cannot generally be detected, Raman spectra may provide valuable information on the formation of metal oxide phases, changes in the metal oxidation state, and the formation of metal-oxide interface bonds. To this end, visible Raman spectroscopy has been used to the study the properties of 0.7% $Pt/CeO_2$,[228] which shows two bands near 550 and 675 $cm^{-1}$ attributed to highly dispersed $PtO_x$ in interaction with $CeO_2$. After reduction, the overall intensity decreased due to visible light absorption and the band at 675 $cm^{-1}$ disappeared, evidencing $PtO_x$ reduction. Raman bands observed in the context of alumina-supported Pt/Ce(/Ba) $NO_x$ storage reduction catalysts have been assigned to $PtO_x/PtO_2$ ($A_g$ mode at 205 $cm^{-1}$), Pt–O–Ce (at 544 $cm^{-1}$), and surface $PtO_x/PtO_2$ (at 689 $cm^{-1}$) species.[229] Depending on the support and the experimental conditions (temperatures above ~750°C), the collection of visible Raman spectra (of supported metals) may be hampered by fluorescence and strong radiation emission. This can be overcome by using UV excitation, as demonstrated for supported $Pd/Al_2O_3$ catalyst at 800°C in an $O_2$/He environment, showing Raman bands at 600 $cm^{-1}$ (Pd–O vibration) and at around 1200 $cm^{-1}$ (first overtone of Pd–O vibration) from alumina-supported $PdO_x$.[66]

The presence of noble metals may affect the (surface) properties of the oxide support.[228,230,180,231] Even for a small amount of metal, visible Raman spectra have revealed differences in the defect structure as probed by oxygen adsorbates. For example, for 0.7 wt% $Pt/CeO_2$ an increased amount of superoxo species[228] and for 0.5 wt% $Au/CeO_2$ additional peroxide features[230] were observed. For a 1 wt% $Au/TiO_2$ catalyst the presence of gold was reported to induce a phase change from anatase to Magnéli or (reduced) rutile phases.[180]

Raman spectroscopy has also been employed to elucidate the interaction of Pd sub-nanometre clusters with oxygen defects in $TiO_2$,[232] showing a blueshift of the $E_g$ peak position of anatase $TiO_2$ with an increasing number of defects in the anatase lattice. Kang *et al.* investigated the beneficial effect of silver on the CO oxidation behaviour of ceria.[233] For a $Ag/CeO_2$ catalyst (with 6 wt% loading), 785 nm Raman spectra showed an increase in the

defect-related features at 275 and 530 $cm^{-1}$ compared to bare ceria. The intensity of these features strongly increased in CO flow due to oxygen consumption and decreased under reaction conditions ($CO/O_2$ flow), which was attributed to a facilitated refilling of oxygen vacancies. In $In_2O_3$-supported silver materials studied during ethanol sensing in air, a strong intensity increase in the $In_2O_3$ phonons upon exposure to reaction conditions has been attributed to the surface reduction of oxidized silver to metallic silver giving rise to SERS enhancement.[234,235] In the initial spectra in oxygen (prior to reaction), no bands for silver oxide were observed, probably due to the presence of a thin oxide layer. Similarly, in low-loaded $CuO/Fe_2O_3$ catalysts (with 3 wt% loading) used for water–gas shift reaction, no Raman signals due to CuO were detected, while spectra showed the presence of the hematite phase (α-$Fe_2O_3$).[236]

***Multicomponent oxides.*** There has been renewed interest in bulk iron molybdate catalysts for methanol partial oxidation to formaldehyde. Raman spectra allow the identification of both crystalline $Fe_2(MoO_4)_3$ and $MoO_3$, the latter being added in excess due to its loss in the hot spot region of the reactor. Raun *et al.* studied the deactivation in more detail, starting from $Fe_2(MoO_4)_3$ and α-$MoO_3$ phases in the fresh catalyst.[237] After 10 h on stream, $MoO_3$ was no longer detected, and after 100 h, bands due to the less-molybdenum-rich β-$FeMoO_4$ (875 and 925 $cm^{-1}$) were observed, in addition to $Fe_2(MoO_4)_3$, indicating slight reduction and molybdenum loss from the iron molybdate phase. With prolonged time on stream new phases were formed, which were assigned to β-$MoO_3$ and hematite (α-$Fe_2O_3$). Regarding vanadates, bulk $FeVO_4$ is of interest for methanol partial oxidation due to its structural similarity to $Fe_2(MoO_4)_3$. In this context, Raman analysis allows one to clearly distinguish between bulk $FeVO_4$, crystalline α-$Fe_2O_3$, and $V_2O_5$ nanophases.[238]

Raman spectroscopy has been shown to be a powerful technique to differentiate between different phases in $Ce_{1-x}Zr_xO_{2-\delta}$ mixed oxides.[239-240] In particular, the cubic–tetragonal phase transition, which occurs by oxygen ion displacements from ideal fluorite sites, is not accessible

to XRD as, among other things, the X-ray atomic scattering of oxygen is much smaller than that of the Zr and Ce cations.[240] Recently, visible Raman spectroscopy has been used to probe the structural properties of $Ce_{1-x}Zr_xO_{2-\delta}$ solids ($0 \leq x \leq 0.8$) as a function of preparation,[241] showing the potential of Raman spectra for identifying the presence of cubic c, pseudocubic t″, and tetragonal t phases, and for gaining insight into the oxygen release/refill mechanism. Raman characterization of defects, which is of importance in the context of ceria and doped ceria materials, for example, will be discussed in the following section.

### 3.2 Phonon confinement and defects

As briefly outlined above, only $q \approx 0$ phonons are Raman active in defect-free crystalline materials. However, this selection rule is relaxed as the size of a material is reduced, as encountered in catalytic materials. To model Raman scattering at wave vectors away from the zone centre, a phonon confinement model (PCM)[242] was introduced, which uses a Gaussian function for a weighted exploration of the dispersion curves (eq. 4):

$$I(\omega) \propto \sum_{i=1}^{n} \iiint_{0}^{2\pi/a} \frac{e^{\frac{-q^2L^2}{8\beta}}}{(\omega-[\omega_i(q)+\Delta\omega_i(q)])^2+\left(\frac{\Gamma}{2}\right)^2} d^3q \qquad (4)$$

In eq. 4, $\Gamma$ is the full natural linewidth at half maximum value (FWHM), $q$ the wave vector, and $L$ the correlation length. For the time being, $\Delta\omega$ is set to 0, but this will be discussed in more detail below (see eq. 5). Originally, $\beta$ was set to 1,[242] but frequently an alternative version of the confinement model has been employed,[243] in which phonons were confined even more strongly by setting $\beta = 2\pi^2$.[243-245]

Equation 4 can be computed by taking the sum over the allowed modes $\omega$, where $\omega(q)$ is the dispersion of the selected mode. Information about the vibrational density of states (VDOS) is available from neutron scattering data or ab initio calculations, for example.[170] The slope of the dispersion curve away from the zone centre determines the direction of the size-dependent

shift and the asymmetric broadening: A negative slope results in a redshift (e.g. ZnO, $CeO_2$), a positive slope in a blueshift (e.g $TiO_2$). In qualitative agreement with the PCM, a linear relation between the position of the $F_{2g}$ mode and the inverse average grain size has been observed for metal oxide nanomaterials.[183] While $L$ has been associated directly with the grain size in particular cases,[246,174,247] it may in general originate from any spatially limiting feature in the grain that leads to phonon confinement, such as defect or impurity spacings. For example, $L$ has been shown to correspond to the distance between defects in the oxygen lattice of $CeO_2$.[248] The assumptions and limitations of the PCM have been critically discussed in the literature.[245,170,171]

The presence of strain effects and/or defects (such as oxygen vacancies) may induce changes in the Raman spectra of oxides, for instance, frequency shifts.[245,249] Based on the definition of the Grüneisen parameter $\gamma$,[250] a relation between the shift in frequency $\Delta\omega_i(q)$, and the relative change in lattice parameter $\Delta a/a_0$ has been proposed (eq. 5):[245]

$$\Delta\omega_i(q) = -3\gamma\omega_i(q)\frac{\Delta a}{a_0} \qquad (5)$$

In this context, there has been recent progress in the application of Raman spectroscopy to ceria materials, which is of importance for a fundamental understanding of the role of defects in catalysis, but also with regard to applications ranging from automotive three-way catalysts (TWCs) to the water–gas shift reaction.[251-260,183,230,184] In TWCs, control of the oxygen-to-fuel ratio is essential to simultaneously remove soot, carbon monoxide, and $NO_x$ from the exhaust stream. To this end, ceria may serve as an oxygen buffer and supplier, by variation of its oxygen (non)stoichiometry, that is, supplying oxygen for carbon monoxide oxidation, and removing oxygen for $NO_x$ reduction, if needed. As an important application of eq. 5, shifts of the ceria $F_{2g}$ Raman mode can be related to the formation of oxygen vacancies in the lattice,[259] which is rationalized by $Ce^{4+}$ to $Ce^{3+}$ reduction accompanying oxygen vacancy formation, hence

increasing the lattice parameter due to the larger ionic radius of $Ce^{3+}$ compared to $Ce^{4+}$. Based on recent DFT calculations, the stoichiometry $CeO_{2-\delta}$ has been related to the Raman $F_{2g}$ shift ($\Delta\omega$) as $\delta = 0.024 \pm 0.005\ \Delta\omega/cm^{-1}$,[259,261] enabling a quantification of the oxygen vacancy concentration. This useful property of the $F_{2g}$ mode has allowed new mechanistic insight into the mode of operation of ceria-supported gold and vanadia catalysts in oxidation reactions,[262,259,263,104] as will be illustrated in Sections 4.1 and 5.1.

Ceria may contain intrinsic or extrinsic defects. Intrinsic defects may result from thermal disorder and/or redox reactions of the solid with its surroundings and may be located at the surface or in the bulk. Ceria surface defects have been studied both experimentally (Raman)[264,265,188,228,230,261] and theoretically (DFT)[266-269,270] by using the formation of $O_2^{2-}$ peroxide species upon oxygen adsorption on reduced ceria as a probe of surface oxygen vacancy sites. Regarding the ceria subsurface/bulk structure, the spectral broadening of the $F_{2g}$ band may serve as an indicator of the defect density of a ceria sample for a given crystal size.[183] Bands blueshifted to the $F_{2g}$ band, that is, located within the 480–600 $cm^{-1}$ region, have been related to the presence of oxygen vacancy defects[270,244,262,245] and thus the presence of reduced $Ce^{3+}$ ions. While UV Raman excitation of ceria at 363.8 nm led to enhanced intensities at 500–600 $cm^{-1}$, assigned to D1 and D2 bands (see Section 4.1),[271] recent studies have shown that under resonant conditions (3.81 eV, 325 nm) the off-resonant D2 band is overshadowed by the resonant LO phonon scattering,[272] indicating that analysis of defect bands under resonant conditions needs to be done with care.

The number of defects in ceria materials can be increased by reduction or extrinsic doping, for example by aliovalent cations, leading to the appearance of additional modes with frequencies near 270 $cm^{-1}$ and 550–600 $cm^{-1}$. Besides, doping ceria with 20 mol% aliovalent cations (Y, Er, Gd, La, etc.) has revealed a linear relationship between the lattice parameter and the $F_{2g}$ Raman mode, illustrating the use of the $F_{2g}$ position as a sensitive indicator for doping, in addition to oxygen (non)stoichiometry, temperature, and isostatic pressure, as described

elsewhere.[260] For the (defect) structural characterization of rare earth (RE)-doped ceria materials (RE = Gd, Tb, Sm, and Pr) both visible and UV Raman spectroscopy have proved useful,[273,112,274] but require careful interpretation due to the overlay of resonance- and sampling depth-dependent effects as discussed above.

It is well-known that the oxygen storage capacity (OSC) of bare ceria is affected by thermal stability issues. To overcome this limitation, different metal oxides have been employed as additives,[275] with zirconia being particularly attractive with respect to function and stability.[276] Recent Raman studies have revealed that the defect-related band at around 600 $cm^{-1}$ in $Ce_{1-x}Zr_xO_{2-\delta}$ mixed oxide (but also in bare ceria) consists of at least two components, whereas the high-wavenumber component is shown to be selectively sensitive to reducing conditions at 450°C and is assigned to a metal−oxygen vibrational mode involving interstitial oxygen atoms that can be reversibly detached/refilled under appropriate conditions.[241]

Defects, and in particular oxygen vacancies, are considered to play a significant role in the (photo)catalytic performance of metal oxides.[277] Visible Raman spectroscopy has been used to identify the presence of oxygen vacancies in titania materials by means of peak shifts, peak broadening, and/or the appearance of new features,[278-283] while a contribution of phonon confinement effects needs to be taken into account in $TiO_2$ nanoparticles. For oxygen-deficient $TiO_2$ anatase sheets with surface-terminated fluorine, two new Raman modes at 155 and 171 $cm^{-1}$ and a weakening of the $B_{1g}$ mode at 397 $cm^{-1}$ were observed and attributed to a reconstructed surface,[279] proposed to consist of exposed titanium atoms with lower coordination numbers, that is, four-coordinated titanium, which may be more favourable sites for reactants in catalytic reactions. After hydrogenation of nanophase $TiO_2$ anatase, black $TiO_2$ nanocrystals were obtained, which besides broadening of the anatase peaks displayed new Raman bands at 247, 294, 353, 690, 766, 849, and 938 $cm^{-1}$ not compatible with any of the three titania polymorphs, and which were assigned to the presence of surface disorder after

hydrogenation.[281] Similarly, Raman spectra of other metal oxides, of less relevance to catalytic applications, have shown indications for the presence of oxygen vacancies. Exemplarily, in ZnO powder reduced in hydrogen atmosphere, the peak position of the $E_2$(high) mode, which is related to the oxide ion vibration, shifts toward a lower frequency as the oxygen vacancies increase.[284] Very recently, clay surfaces rich with hydroxyl groups were shown to induce the formation of oxygen vacancies in $Co_3O_4$ nanoparticles, which then exhibited enhanced catalytic and electrocatalytic performances.[285] In this context, Raman spectra of reduced $Co_3O_4$ displayed a broadening and shift of the $A_{1g}$ mode, attributed to the phonon confinement and distortion around oxygen vacancies. Surface oxygen vacancies were also discussed in the context of the catalytic formaldehyde oxidation at room temperature over nanostructured $Co_3O_4$.[286] In contrast to $Co_3O_4$ nanosheets, which were shown to have a negligible structure disorder, Raman bands of nanoplates and nanobelts at ~225 $cm^{-1}$ and 683 $cm^{-1}$, due to the Raman vibration of $Co^{2+}$–$O^{2-}$ and $Co^{3+}$–$O^{2-}$, show a blueshift assigned to surface oxygen vacancies.

### 3.3 Identification of surface phonons, adsorbates, and surface depositions

Raman spectroscopy is a powerful technique to characterize surface oxygen phonons, including interface modes, adsorbed molecular oxygen species, and coke depositions. In the following, recent progress in this area will be discussed, which is of particular relevance to metal oxide– and zeolite-based catalysts. While Raman spectra provide unique information on surface phonons, the combined use with other techniques, such as IR spectroscopy, is often helpful to obtain a more complete picture, in particular with regard to the presence and quantification of adsorbates.

***Surface oxygen.*** Raman spectroscopy allows the detection of different types of surface oxygen features, including lattice oxygen (M-O-M), interface oxygen (M1-O-M2), superoxides

($O_2^-$), peroxides ($O_2^{2-}$), and surface hydroxyl groups, as has been demonstrated in the context of ceria-based materials, for example.[184,259,263,78] More recently, ceria surface oxygen (lattice oxygen) features at around 250 and 400 $cm^{-1}$ (shoulder) were identified by combined experimental and theoretical studies,[259,184] showing that the 250 $cm^{-1}$ feature (calculated: 225 $cm^{-1}$) originates from O–Ce longitudinal stretching of atoms in the topmost Ce–O layer, and the 400 $cm^{-1}$ feature from the corresponding transversal Ce–O stretching vibration (calculated: 363 $cm^{-1}$). Previously, a band at 250 $cm^{-1}$ had been exclusively assigned to an overtone of a bulk phonon mode (2TA).[244] However, for smaller nanocrystals the surface phonon is much more intense than the 2TA bulk contribution (see below, Fig. 14).

Raman characterization of surface oxygen due to metal-oxygen bonds was discussed above in the context of the structure of supported metals (see Section 3.1). It is known that oxygen-containing interface bonds (M1-O-M2), relevant in the context of supported metal oxides, are widely accessible by visible and UV Raman spectroscopy, for example in transition metal oxide catalysts for oxidation catalysis (V-O-Si, V-O-Al, V-O-Ce, Ti-O-Si, etc.).

Surface hydroxyl groups exhibit typical O–H stretching frequencies and can therefore be used as local probes to provide information on the surface structure (e.g. coordination). While IR spectroscopy is known to be particularly sensitive to hydroxyl groups, Raman spectra may provide access to M–OH or O–H stretching vibrations in specific cases (titania, ceria, etc.), which has recently been shown to be of relevance for elucidating reaction mechanisms, as will be discussed in more detail in Section 4.1.[287,103]

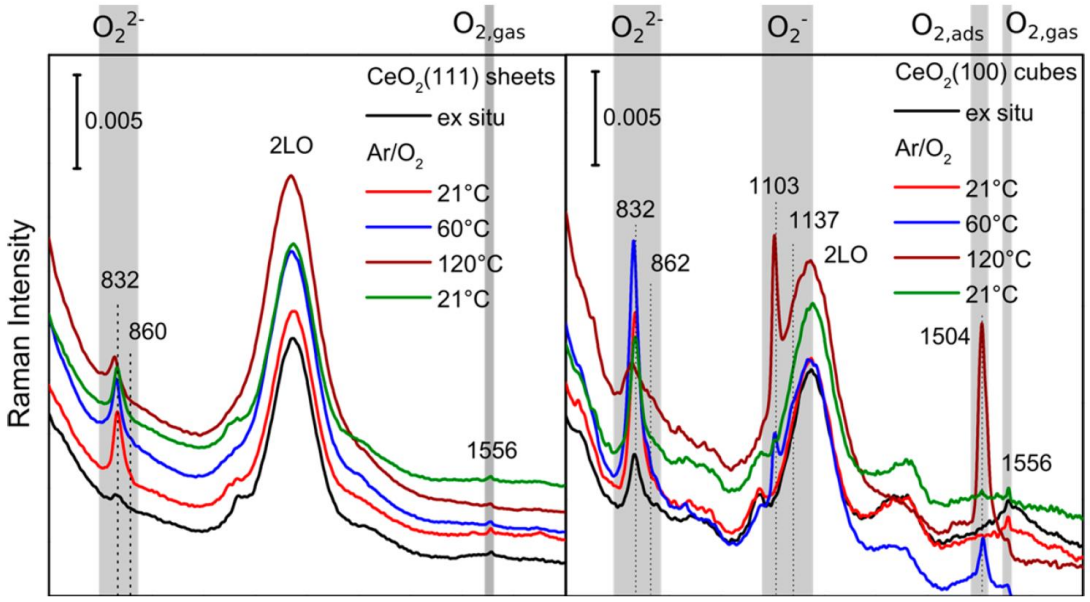


**Fig. 12:** Raman spectra (532 nm) of ceria sheets (exhibiting (111) facets, left) and ceria cubes (exhibiting (100) facets, right), recorded *ex situ* and *in situ* in 25% $O_2$/Ar flow at different temperatures. For details see text. Modified with permission from ref. 187, copyright 2019, American Chemical Society.

***Oxygen adsorbates.*** $O_2$ adsorption and activation plays an important role in oxidation catalysis. Raman spectroscopy has the potential to identify different molecularly adsorbed oxygen species, namely superoxides ($O_2^-$) and peroxides ($O_2^{2-}$), and weakly adsorbed oxygen species ($O_2^{\delta-}$). For a first estimate of frequencies, oxygen bond orders can be considered, for instance, the O–O bond orders of gas-phase $O_2$ and free peroxide ions are calculated to be 2.0 and 1.0, respectively. Based on the O–O stretching frequency of gas-phase $O_2$ at 1556 $cm^{-1}$, the O–O stretching frequency of unperturbed peroxide ions can be estimated to be ~778 $cm^{-1}$. In fact, O–O stretching frequencies in peroxide complexes have been observed in the range 640–970 $cm^{-1}$.[288] Accordingly, as an estimate for free superoxide ions with bond order 1.5, frequencies at ~1167 $cm^{-1}$ are expected. From the 1990s until very recently, Raman studies on the structure of peroxide/peroxo and (to a lesser degree) superoxide/superoxo species were

carried out, for example in the context of $La_2O_3$[45] and Ba/MgO,[289-291,69] TS-1[292,195] (see below, Fig. 20), Fe/MFI,[293] Fe/ZSM-5,[294] Fe/ZSM-35,[114] and Au/$CeO_2$[230,231] catalysts, and a relation to metallo-enzymes and enzyme mimics has been drawn.[295,213,214]

The identification of different molecularly adsorbed oxygen species has recently been demonstrated in temperature- and gas-phase-dependent experiments on faceted ceria nanoparticles.[187] For illustration, Fig. 12 shows Raman spectra (532 nm) of ceria sheets (exhibiting (111) facets) and ceria cubes (exhibiting (100) facets) in 25% $O_2$/Ar flow at different temperatures, showing the facet-dependent oxygen adsorption on ceria nanoparticles. The peroxide feature at around 830 $cm^{-1}$ has been attributed to an O–O stretch vibration, resulting from the adsorption of molecular oxygen onto two electron surface defects.[264,266, 179,268,261] Upon closer inspection, the peroxide feature reveals the presence of an asymmetric band profile, which can be deconvoluted into two components located at 830 $cm^{-1}$ and 860 $cm^{-1}$. For (111) facets, calculations support the existence of two stable peroxide structures at coverages up to 0.25 ML (monolayer), resulting in O–O stretching frequencies separated by ~39 $cm^{-1}$, and showing an intensity ratio consistent with experiment.[261] On the other hand, for (100) facets there is only one stable peroxide structure, that is, the presence of two features is attributed to peroxide species with a different degree of aggregation.[187] Along these lines, in previous experiments on polycrystalline ceria (i.e., $CeO_2$(111)), more strongly reduced ceria samples have shown additional further blueshifted Raman features at 877 $cm^{-1}$ [264] or 874 $cm^{-1}$ [179] and at 881 $cm^{-1}$ [230] for bare $CeO_2$ and Au/$CeO_2$, respectively, which have been attributed to aggregated peroxide species.[261] The formation of superoxide species originates from the transfer of only one electron to the chemisorbed oxygen molecule, and the experimentally observed Raman bands at 1137 and 1103 $cm^{-1}$ can be attributed to superoxides with $Ce^{3+}$ in direct proximity, whereas the latter is assigned to superoxides with $Ce^{3+}$ further part (NNN positions).[187]

Summarizing, the detection of adsorbed oxygen species plays an important role in heterogeneous catalysis for different reasons, for example due to their function as a direct reaction intermediate, such as in TS-1 catalysts (as will be discussed in more detail in Section 4.1), or as a sensitive indicator for the presence of surface defect species, for instance in ceria-based catalysts.

***Other adsorbates.*** A variety of adsorbates, other than adsorbed oxygen species, that are of relevance for catalysis have been detected by (resonance) Raman spectroscopy,[43] such as $NO_x$, i.e., nitrates, nitrites, nitro, and NO (e.g. on BaO,[156,296,291] Pt/(BaO)/$Al_2O_3$,[297-299] $CeO_2$[300,103]); alkoxy species (e.g. methoxy[31,214] and ethoxy[287,104] on supported metal oxides); hydrogen, i.e., M–H, ethylene, and CO (e.g. on (enhanced?) Ni/$SiO_2$[301-304]); acetate/formate species (e.g. on $CeO_2$[305,306]); carbonates (e.g. on BaO[291], Au/$CeO_2$[307]; sulphates (e.g. on zirconia[308], Pt/$Al_2O_3$[309]); and sulphides (e.g. in $MoS_x$[310]). Carbonaceous surface depositions, including aromatics, will be discussed below.

In the presence of enhancements (i.e., SERS), the applicability of Raman spectroscopy for adsorbate identification in catalysts is significantly increased for adsorption on Au, Ag, and Cu SERS substrates, as has been noted earlier.[57] Recently, by using SHINERS, the limitations of SERS have been largely overcome, allowing sensitive detection of adsorbates (CO, oxygen species, ethylene, etc.) on a variety of catalytically active metals (Pt, Pd, Rh, Ru, Ni, etc.),[77] as will be discussed in detail in Section 4.2.

***Carbonaceous surface depositions.*** Raman spectroscopy has been widely used for studying carbons and coke-containing samples. Based on earlier work by Tuinstra and Koenig,[311] a perfect single crystal of graphite shows only one Raman band, at 1575 $cm^{-1}$ (G or graphitic band), which is due to in-plane bond stretching of pairs of $sp^2$ carbons. For amorphous graphite another major Raman contribution is observed, at around 1355 $cm^{-1}$ (D or disordered band), attributed to the 'breathing' mode of the aromatic ring clusters in the graphite sheets.[312]

Often, when the structure of the carbon species is not graphitic, as in activated carbons or coked catalysts, significant line broadening may occur, making peak fitting challenging.[313]

After some pioneering Raman work in the characterization of coke in zeolites,[314,100,315,316,101] the coking progress of H-ZSM-5 has been studied by the Li group more recently under methanol to dimethyl ether (MTD) working conditions using *operando* UV Raman spectroscopy at 325 nm excitation. Methylbenzenium carbenium ions, proposed as an indicator for 'soft coke', are identified at 1605 $cm^{-1}$ and rapidly transform into 'hard coke' at the beginning of the catalyst bed, a process that can be suppressed by the water formed.[317] Using UV Raman spectroscopy at 244 nm excitation, as shown in Fig. 13, Signorile *et al.* analysed a selection of polycyclic aromatic hydrocarbons (PAHs), as representatives of coke-like species, which are frequently found as byproducts of petrochemical reactions, e.g. MTD, or methanol to hydrocarbon (MTH).[318] PAHs were dosed onto Aerosil 300 (a), Silicalite-1 (b), and coconut-origin granular carbon (c) to represent different environments, but only small differences in the position of the vibrational modes are observed in the spectra, highlighting their use as a reference for the identification of PAHs during petrochemical reactions. Recently, the influence of zeolites (ZSM-5, Beta, Mordenite, ZSM-22, SAPO-34) with different topologies for the MTH reaction has been studied by *operando* UV Raman spectroscopy at 244 nm excitation by the Bordiga group,[319] showing that the topology of each catalyst leads to significantly different hydrocarbon transformation pathways.

In the context of propane dehydrogenation over a $CrO_x/Al_2O_3$ catalyst, *operando* visible Raman spectroscopy at 532 nm excitation has been employed to study the coke deposition at the top and bottom of a reactor bed. While the nature of the coke deposits was found to be independent of reaction time and position, differences in the rate of coke deposition were related to the local temperature of the catalyst.[320] Visible Raman spectra have also been used in combination with XRD to study the long-term deactivation of $Co/TiO_2$ Fischer–Tropsch

synthesis (FTS) catalysts, showing the formation of graphitic-like coke species at atmospheric pressure.[321]

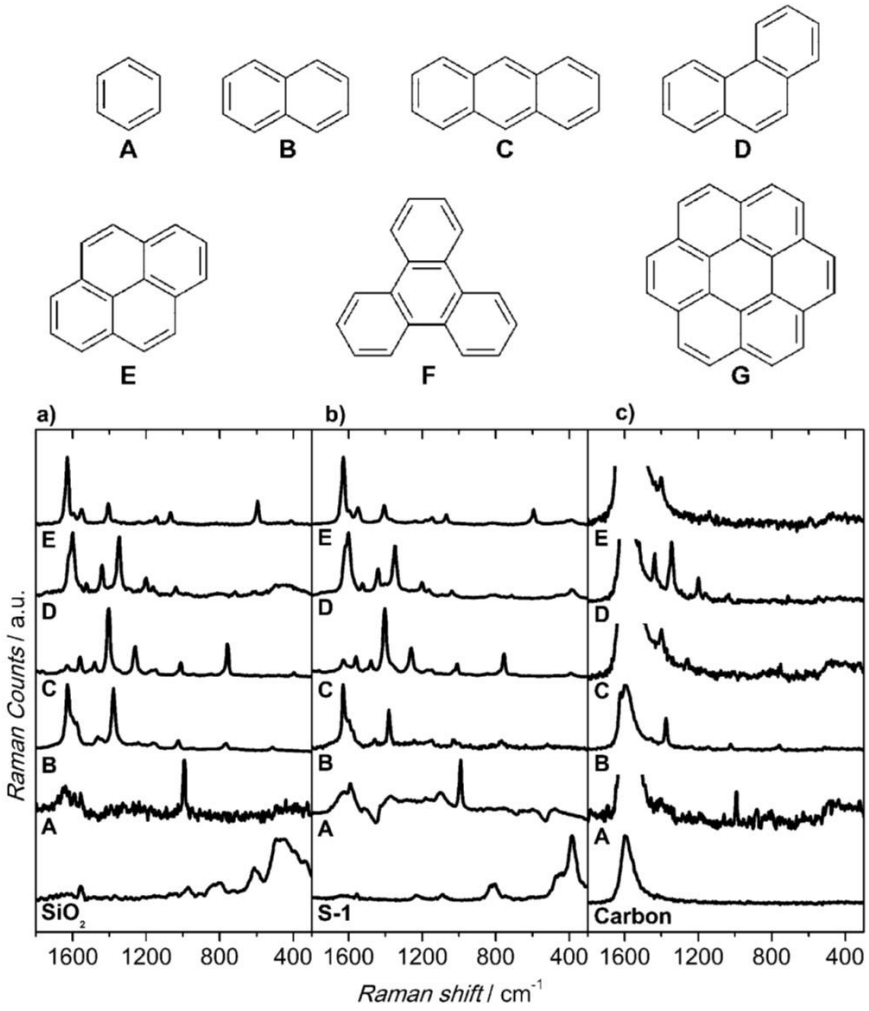


**Fig. 13** UV Raman spectra (244 nm) of benzene A, naphthalene B, anthracene C, phenanthrene D, and pyrene E adsorbed from the vapour phase on Silicalite-1 **(a)**, Aerosil 300 **(b)**, and activated carbon **(c)**.The spectra of the adsorption supports are also reported. Spectra have been rescaled and shifted to ease comparison. Modified with permission from ref. 318, copyright 2015, American Chemical Society.

The soot oxidation reaction over ceria cube-based catalysts has recently been studied using 515 nm excitation.[322] The higher activity of pure and Mn-doped ceria over Cu-containing

catalysts is proposed to be related to their ability to avoid deactivation of $O_2^{x-}$ species during soot oxidation.

### 3.4 Developments in theoretical description

In the past decade there has been considerable progress in the theoretical description of Raman spectra in the context of heterogeneous catalysis, with respect to both classical and quantum chemical calculations. In the following, first the use of normal mode analysis and then the development and application of density functional theory (DFT) approaches to calculate Raman and resonance Raman spectra will be discussed.

As pointed out by Stiegman in the context of supported heterogeneous catalysts,[216] single bond-unit designators (e.g. V=O, V-O-Si) do not adequately describe normal modes. In fact, such characteristic mode descriptors simply indicate the internal coordinates with the largest single contribution (and typically the largest displacement) to the normal mode, but these do not necessarily dominate the vibration.[216] As a consequence, by using an empirical force field[323] it could be shown that the normal modes associated with the 'V=O' and 'V–O–Si' bands of silica-supported vanadium oxides are composed of concerted stretching of the V=O bond coupled to stretching of the bridging Si–O–V bonds,[89] for example, the 'V=O' bond draws considerable contributions from *f*(Si–O) and *f*(V–O) force constants. This approach was expanded by us by explicitly taking the support into account,[198,120,324] by using polyhedral oligomeric silsesquioxanes (POSSs). The silica-supported vanadium oxide catalyst was then modelled by monomeric[198] and also dimeric[120] vanadium oxide species attached to POSS, facilitating the assignment of vibrational bands from UV Raman spectra (at 217.5 nm excitation). The analysis underlines that the vanadium oxide–related modes are characterized by significant contributions of several force constants, while revealing the importance of an adequate description of the support. A combined vibrational and normal-mode analysis has also been applied to dispersed titania.[120,324] For the calculations, double- and tri-grafted

hydroxylated titania species were attached to POSS as a silica support, identifying vibrational features due to Ti–O–Si interphase, Ti–O–Si in-phase, and out-of-phase stretching vibrations, consistent with results from UV Raman spectroscopy (at 217.5 nm excitation).

In recent years, an increasing number of experimental Raman studies in heterogeneous catalysis have been combined with results from DFT calculations to facilitate band assignments, as illustrated by studies mentioned above.[201,206,207,217,222,224,114,263,113] However, the potential of theoretical approaches to describe catalytic systems can be further extended, as will be discussed in the following based on recent progress made in the area of ceria-based and supported metal oxide catalyst materials. Recently, an DFT-based approach was introduced to describe the Raman spectra of polycrystalline ceria, which may serve as a model study for the description of vibrational properties of other metal oxides.[261]

To this end, first normal mode positions are evaluated with a finite differences approach with PBE+U or a hybrid functional framework (HSE06), followed by a calculation of the associated Raman scattering activity using density functional perturbation (or linear response) theory (DFPT) by calculating the change in the macroscopic dielectric tensor for each normal mode, thereby relating it to the third derivative of the energy with respect to atomic positions.[261] Results of such calculations[184] and their comparison with experimental Raman spectra[183] of 25–30 nm and >1000 nm ceria particles are presented in Fig. 14. It should be mentioned that the theoretical approach allows a consistent description of the particle size–dependent ceria Raman spectra including (defective) bulk and surface-related features, as well as oxygen peroxide adsorbates. Important findings include the quantitative description of mode softening of the $F_{2g}$ mode (see eq. 5), as well as the identification of the Ce–O surface phonon modes at around 250 and 400 $cm^{-1}$, both of which are relevant for the interpretation of *operando* Raman spectra, as demonstrated recently for the CO oxidation and water–gas shift reaction over Au/ceria catalysts,[259,263,325,307] including the use of shaped ceria particles.[187,325,307] Regarding the ceria (defect) structure, DFT calculations have revealed that the spectral properties in $CeO_2$-

$_x$ are determined by the valency of the cerium ions ($Ce^{4+}$ or $Ce^{3+}$) and the type of coordination around the cerium ion.[261] Accordingly, $Ce^{3+}$ ions in direct proximity to an oxygen defect are characterized by a calculated band at 500 $cm^{-1}$, whereas $Ce^{3+}$ located in the second coordination sphere of an oxygen vacancy gives rise to a calculated band at 480 $cm^{-1}$. Besides, a calculated feature at around 550 $cm^{-1}$ can be related to a $Ce^{3+}O_7V_O^{\bullet\bullet}$ coordination, that is, the presence of $Ce^{3+}$ close to a defect, and one at around 525 $cm^{-1}$ to a $Ce^{4+}O_7V_O^{\bullet\bullet}$ coordination. A comparison of the theoretical results with experimental data requires the scaling of the calculated vibrational frequencies by a factor of 1.06 to account for the underestimation of the $F_{2g}$ band position in the PBE+U exchange functional framework.[261]

Other recent examples of calculated Raman spectra related to catalysis include doped ceria[326] and metal oxide organic framework (MOF)[327] or crystalline materials.[328] Interestingly, calculated Raman spectra of a reduced ceria surface, for example with 0.25 ML of surface or subsurface oxygen vacancy, reveal a strong intensity decrease of the O–Ce stretching vibrations. Alternatively, the intensity of the surface phonons may be reduced by hydrogen attachment, that is, the formation of hydroxyl groups.[263] These findings are of great relevance for mechanistic studies in fundamental and applied catalysis, as has recently been demonstrated in the context of oxidation reactions, the water–gas shift reaction, and $NO_x$ storage systems.[259,263,103]

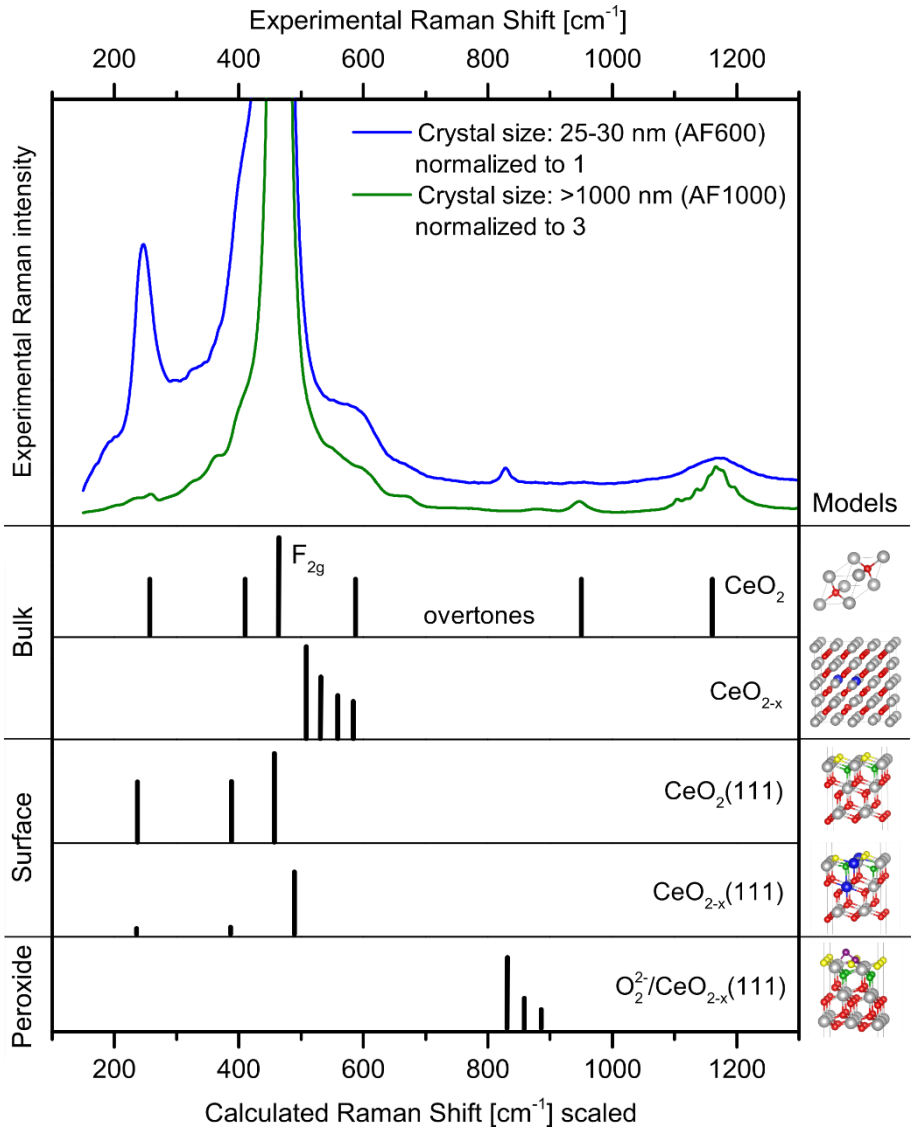


**Fig. 14** Experimental Raman spectra (515 nm) of 25–30 nm and >1000 nm ceria particles in comparison with the calculated bands of the indicated ceria model systems. The calculated Raman shifts were scaled by a factor of 1.06 except for $O_2^{2-}/CeO_{2-x}(111)$. The $O_2^{2-}$ calculated shifts (893 $cm^{-1}$, 932 $cm^{-1}$) were correlated with the experimentally observed shifts (830 $cm^{-1}$, 860 $cm^{-1}$). Only the peroxide mode and the shifts corresponding to the lowest (0.06 ML) and highest (1 ML) $O_2^{2-}$ coverages are displayed. In the models, grey and blue balls represent $Ce^{4+}$ and $Ce^{3+}$ cations, respectively, red balls represent bulk oxygen, and yellow and green balls represent surface and subsurface oxygen atoms, respectively. Reproduced with permission from ref. 184, copyright 2017, American Chemical Society.

To achieve a theoretical description of resonance Raman effects in catalytic materials, detailed calculations on cluster models have recently been performed by the Neese group by using the ORCA suite of programs.[329,199,113] Spectra were calculated by time-dependent density functional theory (TD-DFT) in conjunction with the independent mode displaced harmonic oscillator model (IMDHO). The developed approach was applied to silica-supported vanadium oxide and M1 $MoVO_x$ catalysts, as well as the vanadium complex K[$VO(O_2)$Hheida].[199,113]

For the evaluation of the resonance Raman spectra, Maganas *et al.* considered low-lying electronically excited states of $VO_x/SiO_2$ model structures between 300 and 500 nm (20000 and 35000 $cm^{-1}$), as illustrated for the $V_3Si_5H_5O_{15}$ structure containing a trimeric vanadium oxide unit (see Fig. 15).[199] The calculated absorption spectrum (A) is characterized by three low-lying groups of bands located at 22500 (orange), 25000 (cyan), and 27000 $cm^{-1}$ (purple), resulting from single-electron excitations within the V=O and V–O–V (orange) or V=O and Si–O–V fragments (cyan and purple), while higher lying states are drawn in grey. The corresponding calculated resonance Raman spectrum for $V_3Si_5H_5O_{15}$ is shown in (B). Deconvolution of the calculated Raman spectra regarding the dominant excited state reveals a strong overlap of all states, as each absorption band contains tails that overlap with the other two. In detail, the 1025 $cm^{-1}$ signal is dominated by states involving V=O and V–O–V (orange), as well as V=O and Si–O–V structural motifs (cyan), while the signals at 1050 and 1075 $cm^{-1}$ are dominated by states involving the V=O and Si–O–V fragments (cyan and purple). As shown in (E), the experimental spectrum is better described by the trimeric $V_3Si_5H_5O_{15}$ (C) than the monomeric $VSi_7H_7O_{13}$ (D) due to the presence of V–O–V vibrations.[199]

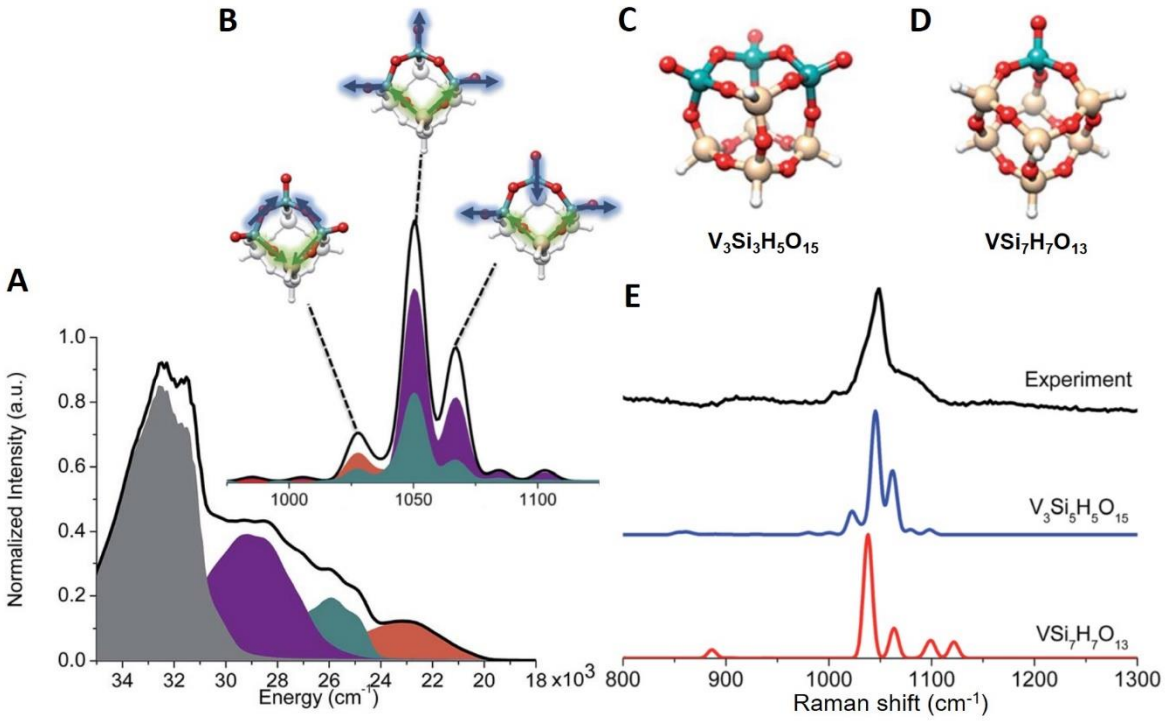


**Fig. 15** Calculated absorption **(A)** and Raman **(B)** spectra of $V_3Si_5H_5O_{15}$ **(C)**. The states are grouped according to the character of the dominant single-electron excitations involving either V=O and V–O–V sequences (orange), or V=O and Si–O–V sequences (cyan and purple). Higher lying states are drawn in grey. In **(E),** the experimental Raman spectrum is compared to the calculated spectra of $V_3Si_5H_5O_{15}$ **(C)** and $VSi_7H_5O_{15}$ **(D)** after applying a shift. For details see text. Modified with permission from ref. 199, copyright 2016, Royal Society of Chemistry.

***Metals – SERS.*** As described above, experimental Raman spectra of molecules and periodic non-metallic systems (e.g. oxides) of relevance to heterogeneous catalysis have been successfully reproduced by theory. In contrast, the calculation of Raman spectra of adsorbates on metal surfaces is not straightforward, as their intensities depend not only on the formation of adsorption bonds, but also on enhanced near fields generated by surface plasmon excitations and resonances excited in the Raman experiment.[330] Recently, a method for simulating Raman spectra of adsorbates on metal surfaces was introduced,[330] based on first-principles phonon

calculations within periodic boundary conditions (slab model) with the polarizability derivatives obtained from a minimal electrostatic-corrected cluster model, which contains additional electron charge to compensate for the loss of coordination of the metal atoms. Applying this approach to Rh(111) surfaces allows Raman spectra of CO and ethylene adsorption to be simulated and the enhancement of the Raman intensity of both CO and ethylene upon chemisorption to be related to the gain of charge on carbon atoms and the polarization of orbitals.[330] Interestingly, the methodology is general and may therefore be applied to other systems, for example from the field of surface-enhanced Raman spectroscopy (SERS).

To describe the adsorption of molecules on metal surface, besides the use of cluster models,[331-335] progress has been made in the application of the framework of periodic boundary conditions to the electronic structure of metallic substrates,[336,337] enabling the calculation of Raman intensities of benzene thiol adsorbed on the Au(111) surface.[337] Previous approaches[336,337] were combined to develop a quasi-analytical method based on density functional perturbation theory and the finite-difference approach to calculate the Raman tensors by the finite-difference of Born effective charges with respect to the electric field, while the Born effective charges are calculated analytically,[338] improving the computational efficiency. As an application, Raman spectra of 4,4′-bipyridine adsorbed on a Au(111) surface were calculated, reproducing experimental SER and TER spectra.

## 4. Sensitivity enhancements for characterization of catalysts and catalytic reactions

Owing to the significant developments in the use of resonance, time-gated, UV, surface-enhanced and shell-isolated nanoparticle enhanced Raman spectroscopy and their increasing importance for applications in heterogeneous catalysts, in the following, important findings of the past decade will be discussed in the context of selected examples from the literature. The

aim is to provide an overview of the various features that resonance, UV, and surface-enhanced Raman spectra can provide, including increased sensitivity to surface and adsorbate species, selective enhancements, fluorescence reduction, and defect characterization. Other techniques that have been employed to enhance the sensitivity of Raman spectroscopy, such as tip-enhanced Raman spectroscopy (TERS) and coherent anti-Stokes Raman scattering (CARS), will be discussed later in the context of spatially resolved analysis.

### 4.1 Resonance and UV Raman spectroscopy

As rationalized by the Kramers–Heisenberg equation discussed above (see eq. 2), resonance Raman effects may lead to an increase of the Raman intensity by several orders of magnitude. In practice, however, self-absorption effects need to be taken into account.

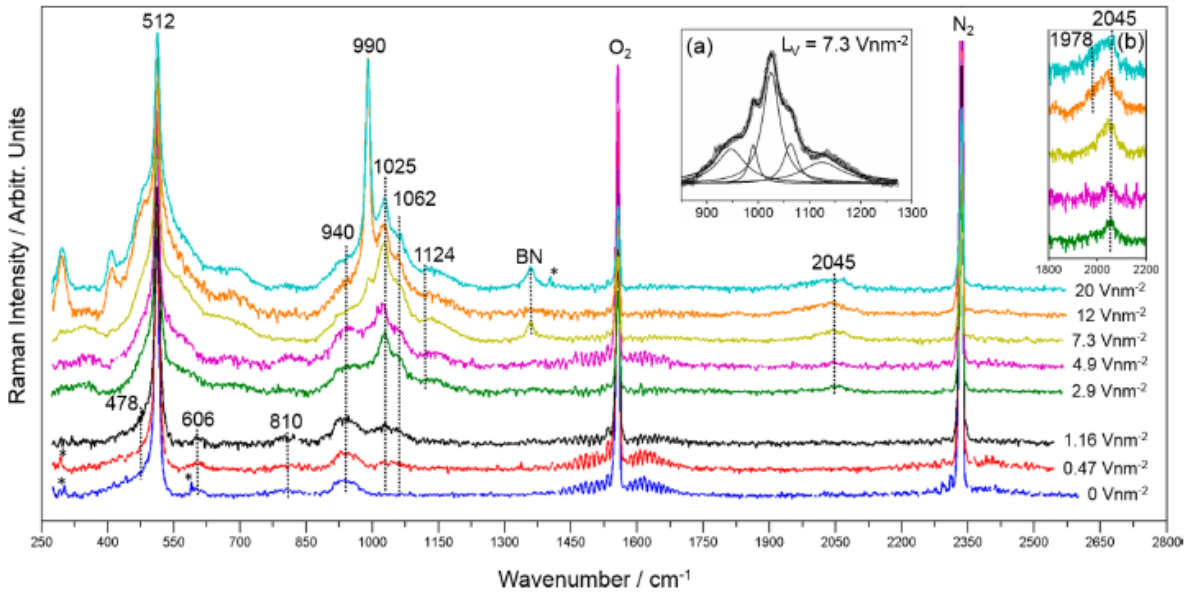


**Fig. 16** Raman spectra at 256.7 nm excitation from wafer-based $VO_x/SiO_2/Si(100)$ planar samples demonstrating the sensitivity of UV resonance Raman spectroscopy. Spectra were taken at 220°C, offset, and normalized to the Si phonon at 512 $cm^{-1}$. Marked peaks are spectroscopic artefacts from cosmic radiation. Inset (a) illustrates the fitting analysis for the sample with a loading of 7.3 V $nm^{-2}$, while inset (b) gives an enlarged view of the overtone

region. Reproduced with permission from ref. 98, copyright 2016, American Chemistry Society.

In the following, the potential of UV and/or resonance Raman spectroscopy for applications in catalysis will by highlighted by means of examples from the literature. There are only a few techniques that provide sufficient sensitivity for vibrational analysis of surface species on planar model systems while at the same time allowing *in situ* experiments at elevated temperatures in air. With regard to Raman techniques, these include resonance Raman (RR) spectroscopy,[339,98] surface-enhanced Raman spectroscopy (SERS), and tip-enhanced Raman spectroscopy (TERS).[340,74,77] As will be discussed below, SERS is not applicable to metal-free samples, and TERS requires specific instrumentation. In addition, sum-frequency generation (SFG) and infrared reflection−absorption spectroscopy (IRAS) are alternative techniques for the investigation of model catalysts. However, IRAS is only suitable on reflecting metal surfaces,[341] and SFG is a surface-specific technique based on a second-order nonlinear process forbidden in centrosymmetric media.[342] The increased sensitivity of UV resonance Raman spectroscopy has recently been demonstrated by Waleska and Hess for planar $VO_x/SiO_2/Si(100)$ model catalysts prepared by controlled spin-coating impregnation,[98] mimicking pore-volume impregnation typically used for powder catalysts.[343] Figure 16 presents UV Raman spectra at 256.7 nm excitation from wafer-based $VO_x/SiO_2/Si(100)$ planar samples as a function of vanadium loading, recorded at 220°C in air. As described above, samples were irradiated with reduced intensity (see Fig. 5) and subjected to continuous movement using an *xyz*-stage. Besides the strong Si signal at 512 $cm^{-1}$, and the $SiO_2$-related features at ~478, 606, and 810 $cm^{-1}$, all Raman spectra show vanadium oxide features at 1025, 1062, and at around 940 $cm^{-1}$ (with a contribution from Si), due to V=O (vanadyl), V–O–Si out-of-phase and V–O–Si in-phase stretching vibrations of tetrahedrally coordinated vanadium,

respectively, as well as vanadyl-related overtone features at around 2045 $cm^{-1}$ (see inset). Previously, Mojet *et al.* had investigated similar model systems for dispersed molybdena using UV Raman spectroscopy.[339] The increased sensitivity of UV resonance Raman spectroscopy has also been demonstrated for $VO_x/SiO_2$ and $TiO_2/SiO_2$ powder samples based on silica SBA-15, which allow structural analysis over a wide range of vanadium (0.00001−0.7 V/$nm^2$) and titanium (0.001–0.7 Ti/$nm^2$) loadings.[120]

Raman spectroscopy has been shown to be a powerful tool to probe the defect chemistry of ceria materials. In general, defects in ceria can be modified by reduction or nanostructuring of undoped ceria, or by doping. As a result, in the Raman spectra, shifts of the $F_{2g}$ mode related to changes in the lattice constant, a splitting of the $F_{2g}$ mode occurs, and additional features can be observed at positions with lower and higher wavenumbers than the $F_{2g}$ mode.[260,184,183,78] Defect-related features in undoped and doped ceria materials can be resonantly enhanced by visible[344] and, in particular, UV excitation (e.g. at 325 or 368 nm).[271,188,345,112,272] For illustration, Fig. 17 shows UV resonance Raman spectra of ceria nanocrystals (A/B) by Wu *et al.* and gadolinium-doped ceria materials (C) by Taniguchi *et al.*. The 325 nm Raman spectra of the ceria nanocrystals, that is, nanorods (a), nanocubes (b), and nano-octahedra (c), all calcined at 673 K, are characterized by (i) a 2LO band at 1179 $cm^{-1}$, which is as strong as the $F_{2g}$ mode at 462 $cm^{-1}$, (ii) a 3LO band at around 1760 $cm^{-1}$, underlining the resonance conditions, and (iii) a defect band at around 592 $cm^{-1}$ with intensity comparable to the $F_{2g}$ mode.[188] For the relative intensity ratio I(D)/I($F_{2g}$), the sequence nanorods > nanocubes > nanooctahedra was obtained (see Fig. 17), indicating that nanorods exhibit the most intrinsic defect sites.

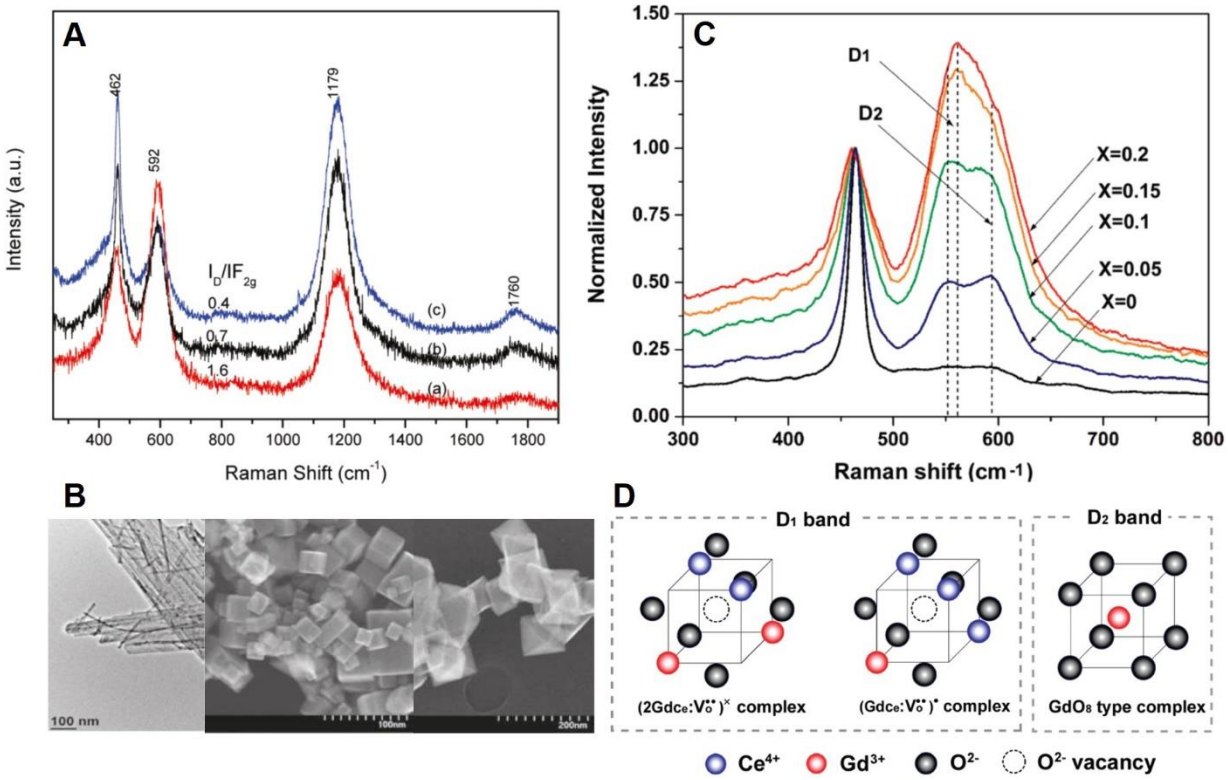


**Fig. 17** UV Raman spectra (325 nm) **(A)** of nanorods (a), nanocubes (b), and nanooctahedra (c). TEM images of the nanocrystals are shown in **B**. Normalized UV Raman spectra (363.8 nm) of $Ce_{1-x}Gd_xO_{2-x/2}$ samples annealed at 1000°C with $F_{2g}$ band intensity **(C)** together with the corresponding D1 and D2 structures **(D)**. Reproduced with permission from ref. 188, copyright 2010, American Chemistry Society and from ref. 271, copyright 2009, American Chemistry Society.

Figure 17C shows 363.8 nm Raman spectra of the D band region of gadolinium-doped $Ce_{1-x}Gd_xO_{2-x/2}$ materials ($0.2 \leq x \leq 0.2$) normalized by the $F_{2g}$ band intensity.[271] The D band is split into two bands (D1, D2), centered on around 550 and 600 cm$^{-1}$, respectively. With increasing $Gd^{3+}$ concentration, the relative intensity ratio $I$(D1)/$I$(D2) shows an increase and the D1 feature shifts to higher wavenumbers. According to the authors, the D1 band is attributed to the presence of oxygen-vacancy defects leading to a symmetry different from that of the $O_h$ point group, whereas the D2 band is assigned to defect spaces with $O_h$ symmetry containing a

dopant cation in 8-fold coordination of $O^{2-}$ but no oxygen vacancy (see Fig. 17D). The use of a 244 nm laser revealed lower sensitivity to defects than 325 and 363.8 nm excitation, indicative of a defect-related electronic absorption band in the middle to near UV range.

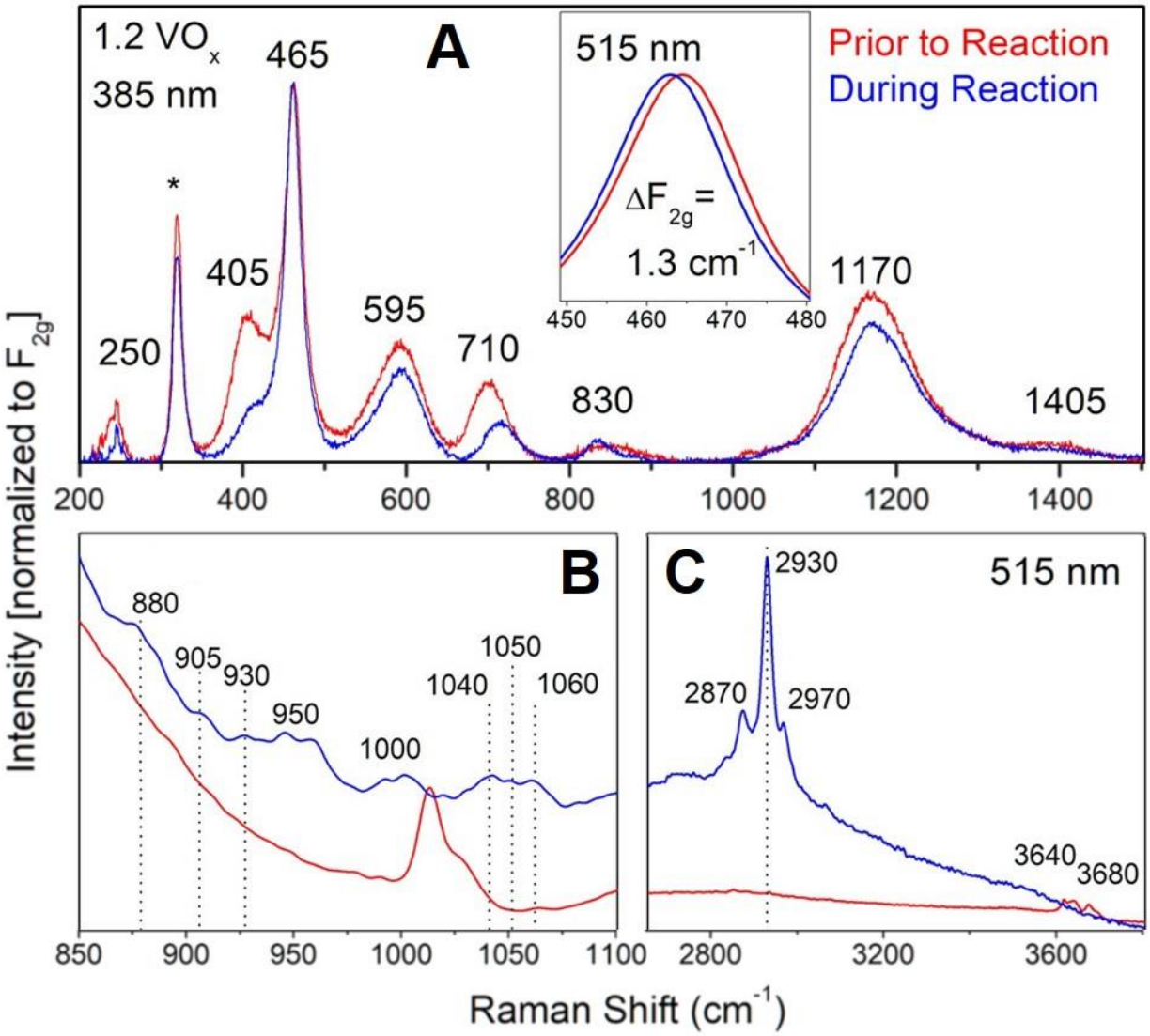


**Fig. 18** *Operando* UV (385 nm, **A**) and visible (515 nm, **B**/**C**) Raman spectra of 1.2 $VO_x/CeO_2$ during oxidative dehydrogenation of ethanol at 100°C in 1% ethanol/8% $O_2$/91% $N_2$ flow compared to *in situ* Raman spectra prior to reaction in 8% $O_2$/92% $N_2$ flow. Raman spectra were normalized to the $F_{2g}$ band at 465 $cm^{-1}$, and offset for clarity. The artefact (marked with an asterisk) at 320 $cm^{-1}$ is due to the $CaF_2$ window of the reaction cell. The inset in A gives an

enlarged view of the 515 nm spectrum in the $F_{2g}$ region. Reproduced with permission from ref. 104, copyright 2020, American Chemistry Society.

Resonance Raman effects have been exploited in a targeted manner to study the catalyst structure[88,111,116,201] and structural dynamics of catalytic reactions[121,104] by making use of multi-wavelength Raman spectroscopy. Very recently, this approach has been applied to study ceria-supported vanadium oxide ($VO_x/CeO_2$) catalysts during oxidative dehydrogenation (ODH) of ethanol under *operando* conditions (using 257, 385, 515, and 633 nm excitation) to provide direct experimental evidence for active support participation in oxide catalysis.[104] In particular, 385 and 515 nm excitation have been shown by Ober *et al.* to allow the selective enhancement of ceria and vanadia vibrational features, respectively, as illustrated in the following. Figure 18 shows *operando* UV (A) and visible (B/C) Raman spectra during oxidative dehydrogenation of ethanol over 1.2 wt% $VO_x/CeO_2$ at 100°C, compared to *in situ* spectra recorded under oxidative conditions. The inset in A gives an enlarged view of the 515 nm spectrum in the $F_{2g}$ region, indicating subsurface reduction under reaction conditions (see Section 3.2). Laser excitation at 385 nm allows dedicated monitoring of the structural dynamics of the ceria surface phonon at around 405 $cm^{-1}$ and the Ce–O–V interface mode at around 710 $cm^{-1}$. Upon exposure of the sample to reaction conditions, the 405 $cm^{-1}$ feature in the spectra strongly decreases and the 710 $cm^{-1}$ band shows an intensity decrease and a blueshift (see Fig. 18A), indicating surface reduction and modification/consumption of Ce–O–V linkages, respectively. Complementary information is available for excitation at 515 nm, as now vanadia-related modes experience more enhancement than at 385 nm. In fact, as shown in Fig. 18B, upon switching from oxidative to reactive conditions, the vanadia-related features at around 1015 and 1030 $cm^{-1}$ experience a substantial loss in intensity and a downward shift to 1000 $cm^{-1}$ due to the coordination of ethanol and/or water to the vanadia structure. Besides, a series of new Raman

bands is detected at around 880, 905, 930, 950, 1040, 1050, and 1060 $cm^{-1}$ under reaction conditions (see Fig. 18B), which are due to C–C and C–O stretching modes and suggest the presence of different ethoxy species. Detailed analysis of the high-wavenumber region (see Fig 18C) reveals the disappearance of O–H stretching bands at around 3640 and 3680 $cm^{-1}$ and the appearance of C–H stretching bands at around 2870 $\nu_s(CH_2)$, 2930 $\nu_s(CH_3)$, and 2970 $cm^{-1}$ $\nu_{as}(CH_3)$, suggesting the formation of ethoxy species.

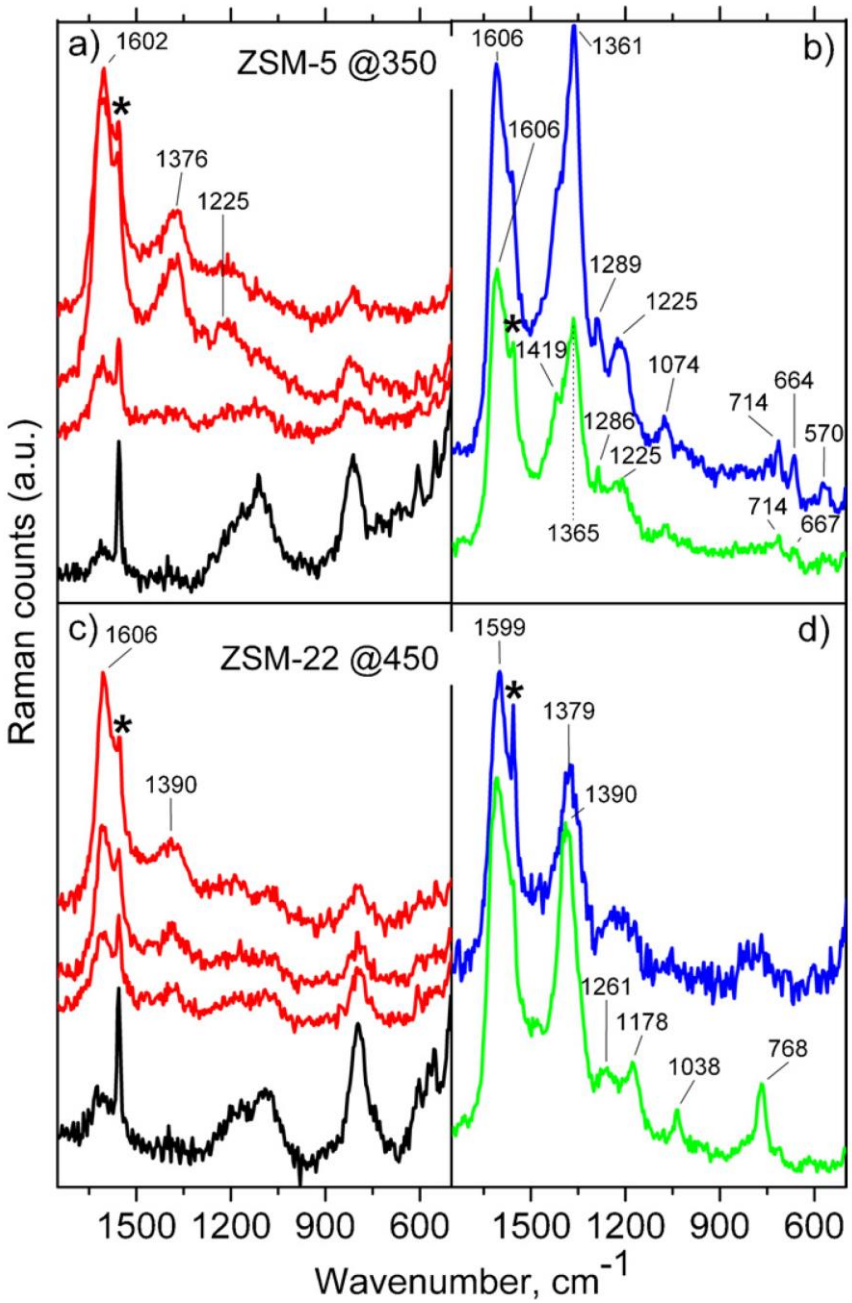

**Fig. 19** *Operando* 244 nm Raman spectra of ZSM-5 and ZSM-22 during MeOH conversion to hydrocarbons (MTH) at 350°C and 450°C, respectively, after (a),(c) activation in air at 550°C (black) and three successive MeOH pulses (red), and after (b),(d) a long MeOH pulse (blue) and subsequent flushing with He (green). Reproduced with permission from ref. 101, copyright 2013, Elsevier.

It is well known that fluorescence can hamper the Raman spectroscopic investigation of zeolites or compounds with similar framework structures, and sometimes in hydrocarbon environments.[31,73] As discussed above, from the experimental point of view (see Section 2.3), fluorescence can be largely reduced or even completely avoided by UV excitation, thus significantly increasing the sensitivity of Raman spectroscopy. Besides, the use of UV radiation further enhances the Raman signal due to the increased scattering intensity (see eq. 1). Beato *et al.* have demonstrated the potential of UV Raman spectroscopy for zeolite studies in a study on methanol to hydrocarbon (MTH) conversion over ZSM zeolites.[101] For illustration, Fig. 19 shows *operando* UV-Raman spectra (at 244 nm excitation) of ZSM-5 (ZSM-22) during MTH at 350°C (450°C). To prevent any UV laser-induced processes, a fluidized bed approach was employed (see Fig. 6). In fact, without movement of the particles, and at the same laser power, decomposition of methanol was observed, resulting in the appearance of a broad band at around 1560 $cm^{-1}$ due to coke-like species, originating from laser-induced polycondensation and dehydration reactions of methanol. Focusing on ZSM-5, pre-treated in air at 550°C to remove all pre-adsorbed molecules, exposure to methanol pulses leads to the growth of hydrocarbon-related Raman bands, first at 1602 $cm^{-1}$ and then particularly at 1376 $cm^{-1}$, while at the same time the intensity of the framework vibrations of ZSM-5 is strongly reduced (see Fig. 19). This behaviour is attributed to hydrocarbon molecules starting to build up in the pores of the zeolite. In detail, the band at 1602 $cm^{-1}$ is associated with the initial adsorption of non-cyclic olefins

(e.g. butadienes or pentadienes) being subsequently transformed into aromatic molecules via cyclization reactions (see Section 3.3). The Raman band at around 1360 $cm^{-1}$ is characteristic of the aromatic breathing mode of benzenes, which together with other characteristic low-wavenumber bands is indicative of filling of the zeolite pores with polymethylated benzenes and naphthenes. Flushing with He at reaction temperature shows that only a small fraction of these species are large enough to be bound more strongly to the zeolite surface. For ZSM-22 a similar overall behaviour is observed, however, there are differences regarding the content and further reaction of aromatic molecules owing to the more space-restricted 1D structure.[101]

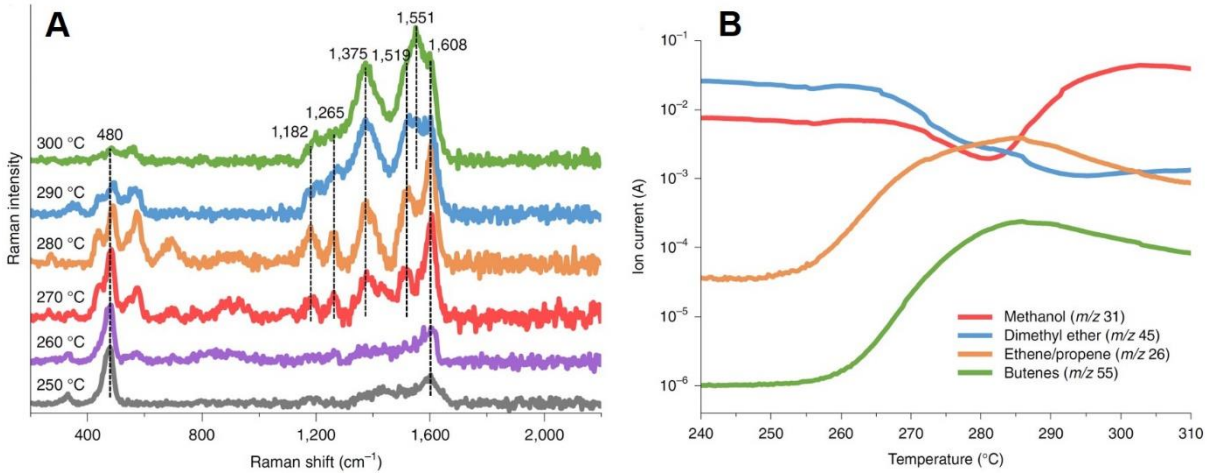


**Fig. 20** *Operando* Kerr-gated Raman spectroscopy over SSZ-13 zeolite during MTO reaction. **(A)** Temperature-dependent Raman spectra at 400 nm excitation. **(B)** Mass traces of methanol and the reaction products. For details see text. Reproduced with permission from ref. 346, copyright 2020, Springer Nature.

Very recently, time-gated Raman spectroscopy has been applied to SSZ-13 zeolites to monitor the formation of hydrocarbon species at various stages of the methanol to olefin (MTO) reaction (see Fig. 20).[346] To circumvent fluorescence, which is inherent to zeolite catalysts, visible laser excitation was combined with a Kerr-gated spectrometer, which collects the

Raman signal but rejects fluorescence emission, based on the temporal differences between the two processes.[347] Besides, the formation of colored hydrocarbons is expected to give rise to resonance enhancement of the Raman signal. Figure 20A shows the temperature-dependence of *operando* Kerr-gated Raman spectra during MTO reaction over SSZ-13 zeolite.[346] As indicated by the corresponding mass spectra in Fig. 20B, methanol conversion substantially increases above 260°C, leading to the formation of new major bands at 1608, 1519, 1375, and 576 $cm^{-1}$, which are attributed to methylated benzenium ions in good agreement with dynamical simulations. The decreasing methanol conversion at 290°C is accompanied by the appearance of a new band at 1551 $cm^{-1}$, which further grows in intensity as the temperature is increased (see Fig. 20) and is assigned to extended polyenes with no or small branches. Such polyenes show almost no mobility and are identified as crucial intermediates towards formation of polycyclic aromatic hydrocarbons (PAHs).

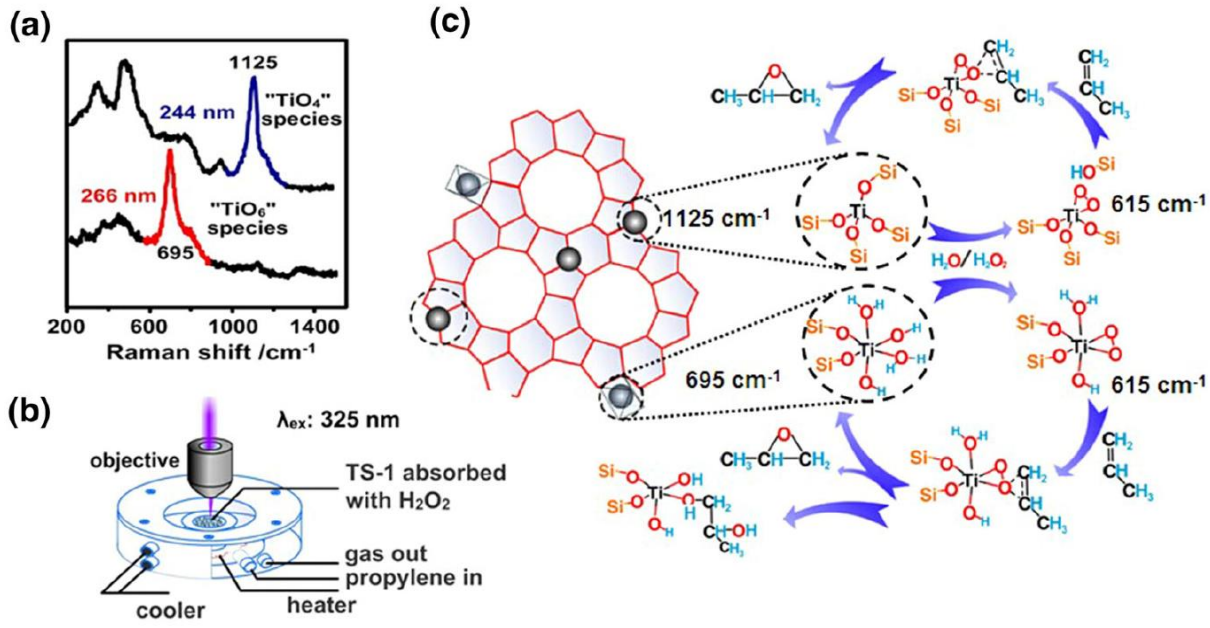


**Fig. 21 (a)** Characterization of titanium species in TS-1 using UV resonance Raman spectroscopy. **(b)** *In situ* UV Raman cell for characterizing propylene epoxidation. **(c)** Proposed reaction pathways during propylene oxidation over $TiO_4$ and $TiO_6$ species. Reproduced with permission from ref. 72, copyright 2015, Springer.

In a comprehensive study, Guo *et al.* employed UV resonance Raman spectroscopy to study the structure and active titanium species in TS-1 zeolite, which has been widely used for partial oxidation reactions with $H_2O_2$ as an oxidant under mild conditions.[348,349] It is shown that with 244 nm excitation mainly framework titanium ($TiO_4$) is detected via Ti–O–Si stretching vibrations at 490, 530, and 1125 $cm^{-1}$, while 266 nm excitation gives access to another titanium species in octahedral coordination ($TiO_6$), mainly via Ti–O bending and stretching at 270 and 695 $cm^{-1}$, respectively (see Fig 21a).[195] The role of the two titanium species in propylene epoxidation was investigated by *in situ* Raman spectroscopy with a 325 nm wavelength laser (Fig. 21b). Interestingly, both titanium species reacted with $H_2O_2$, leading to $\eta^2$ side-on Ti-peroxo formation, characterized by a Raman band at 615 $cm^{-1}$, which has been proposed as an active intermediate in propylene epoxidation.[292] After the '$TiO_4$' species had been exposed to propylene, propylene oxide was detected and the 1125 $cm^{-1}$ band reappeared; on the other hand, for the catalyst with '$TiO_6$' species, the 1,2-propanediol byproduct was also observed, and the Raman band at 695 $cm^{-1}$ did not recover, which was explained by the deactivation of '$TiO_6$' species by the diol byproduct. As a consequence, there have been efforts to increase the concentration of framework titanium in TS-1 by changing the synthesis conditions.[350] Figure 21c summarizes the proposed reaction pathways during oxidation of propylene, including propylene oxide formation over $TiO_4$ and $TiO_6$ species as well as the side reaction to the diol over $TiO_6$ species.

Furfuryl alcohol (FA) is an important building block in the food, polymer, and pharmaceutical industries. It is primarily used as a monomer for the synthesis of polymerized fufuryl alcohol (PFA) via acid-catalysed polycondensation, for applications as adsorbants, adhesives, and membranes. As an example of the use of Raman spectroscopy in the context of biomass-based energy production, Kim *et al.* studied the effects of organic solvents on the

polymerization of FA to PFA using Raman spectroscopy (see Fig. 22a).[351] As shown in Fig. 22b for FA mixed with diluted sulphuric acid catalyst (FS), in the case of visible laser excitation (632.8 nm), the Raman spectrum is dominated by fluorescence. On the other hand, UV Raman spectra (325 nm) provide a good signal-to-noise ratio, allowing the polymerization of FA to be followed, characterized by the disappearance of the C=C stretching mode of aromatic furan groups at 1504 $cm^{-1}$ and the appearance of exocyclic C=C bonds of conjugated diene structures at 1654 $cm^{-1}$ (see Fig. 22c). Quantitative analysis of the peak intensity ratios reveals that the reaction rate significantly decreases with increasing concentration of ethanol or butanol.

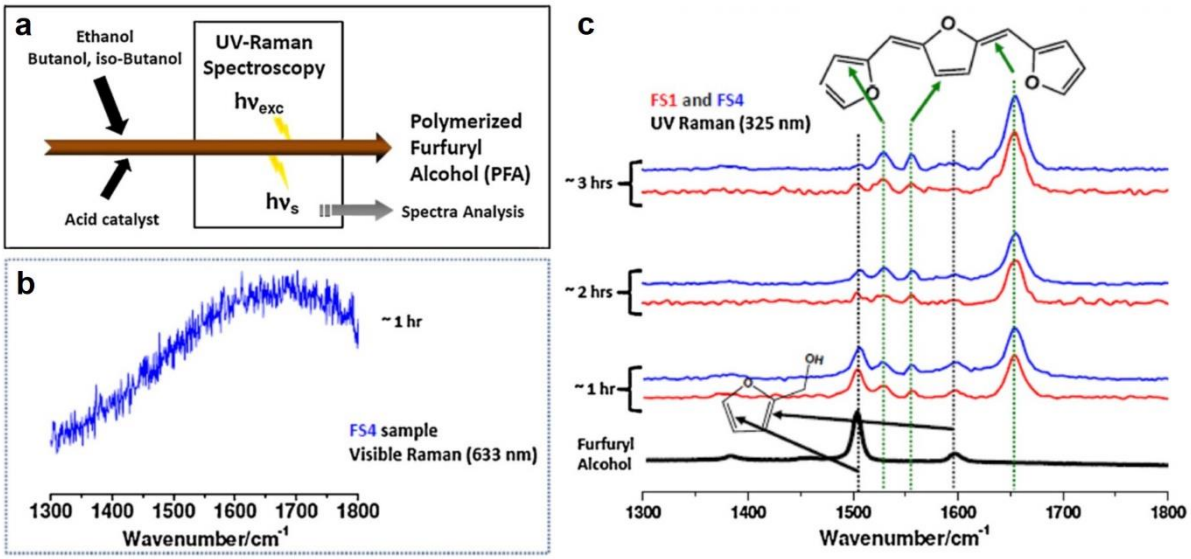


**Fig. 22** Furfuryl alcohol (FA) polymerization reaction at room temperature and ambient pressure. Whereas the visible (632.8 nm) Raman spectrum is obscured by fluorescence (left), UV (325 nm) Raman spectra allow the transformation of endocyclic to exocyclic C=C bonds during FA polymerization to be monitored (right). For details see text. Modified with permission from ref. 351, copyright 2013, Elsevier.

### 4.2 Surface-enhanced Raman spectroscopy

As described in more detail in Section 2.5, surface-enhanced Raman scattering (SERS) can strongly enhance the sensitivity of Raman spectroscopy if molecules are attached to rough metallic nanostructures exhibiting surface plasmon excitations. Following earlier SERS studies,[352-356,145,357-359] there has been continuous interest in using SERS for the characterization of surface reactions and heterogeneous catalysts.[74, 360-366] As an example for applying SERS in the context of environmental catalysis, Muniz-Miranda studied the photocatalytic degradation of the pollutant 4-nitrophenol using Ag-doped titania (anastase) colloid.[364] It is shown that such an approach allows to combine the catalytic properties of titania with the capability of SERS-active metals to follow the course of a surface reaction. Figure 23 shows the spectral changes in the SER spectrum of 4-nitrophenol adsorbed on Ag/titania colloid under UV irradiation (254 nm).[365] In particular, the symmetric stretching band of the nitro group at around 1330 $cm^{-1}$ declines in intensity with increasing irradiation time, which is related to the UV-induced reduction of nitrophenol to aminophenol.

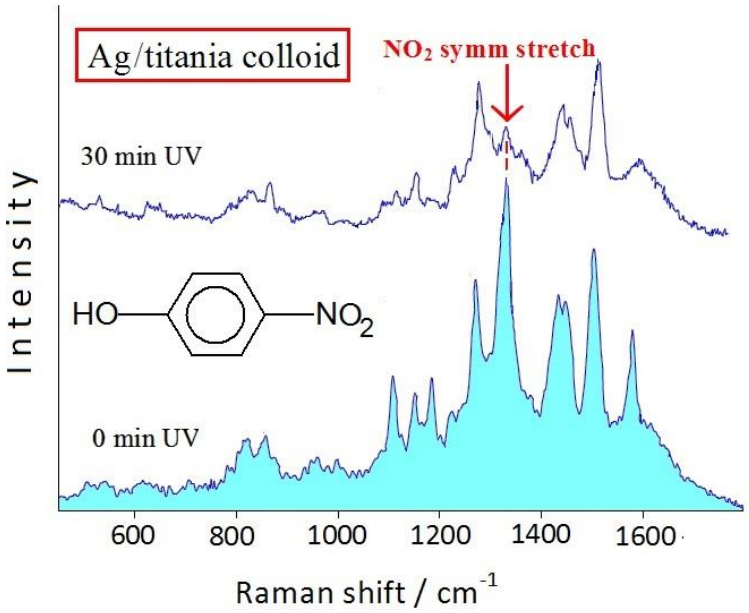

**Fig. 23** SER spectra during degradation of 4-Nitrophenol on Ag/titania colloid under UV radiation. For details see text. Reproduced with permission from ref. 365, copyright 2015, OMICS International.

In the last years, SERS has been employed as a powerful *in situ* vibrational probe in the context of plasmon-assisted/catalysed chemical reactions.[367-372] To this end, Huang *et al.* explored the mechanism of surface plasmon-assisted oxygen activation over Au and Ag nanoparticles supported by metallic (Au, Ag) films, using the selective oxidation of p-aminothiophenol (PATP) to p,p'-dimercaptoazobenzene (DMAB) as a model reaction. The surface plasmon resonance serves two purposes, to activate the reaction and to enhance the Raman signal of surface species via gap-mode SERS (see Fig. 24A). The Raman spectra in Figure 24B show that in the presence of $^3O_2$ (air) on Au film/PATP/Au nanoparticles, the DMAB product is formed, as evidenced by the formation of the characteristic $a_g$ modes at 1140, 1388, and 1434 $cm^{-1}$, whereas in $N_2$ atmosphere no DMAB-related bands are detected. The authors propose the activation of oxygen to include the plasmon-assisted formation of superoxides ($O_2^-$) and their subsequent transformation to surface Au or Ag oxides or hydroxides, responsible for PATP oxidation.

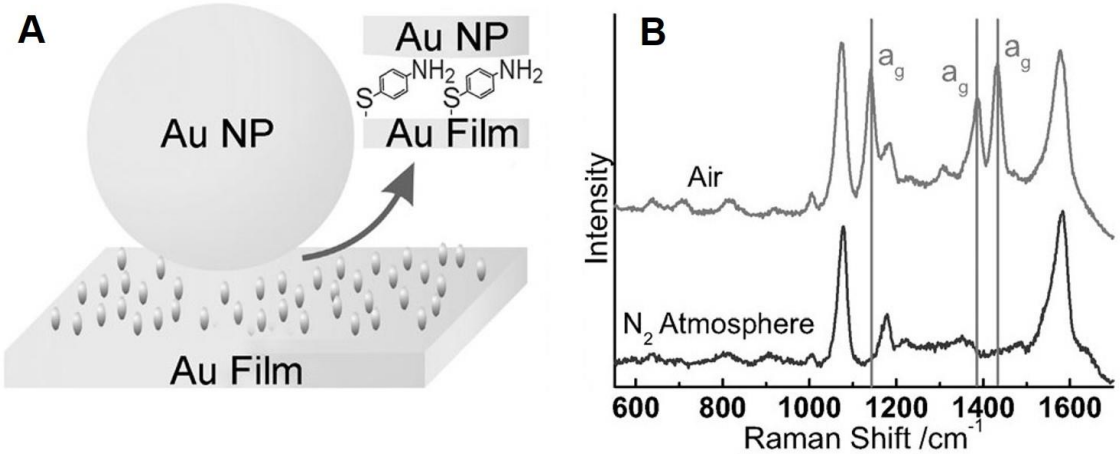

**Fig. 24** Oxidation of p-aminothiophenol (PATP) to p,p'-dimercaptoazobenzene (DMAB) at room temperature. **(A)** Au film/PATP/Au nanoparticles. **(B)** Comparative SER spectra of Au film/PATP/Au nanoparticles recorded in air and $N_2$ atmosphere. The $a_g$ modes correspond to the DMAB product. Modified with permission from ref. 373, copyright 2014, Wiley-VCH.

As discussed above the presence of noble metallic nanostructures used for SERS is not innocent and may lead to an (undesirable) interference with the catalytic reaction. Using shell-isolated nanoparticle-enhanced Raman spectroscopy (SHINERS) this influence can be overcome, because in these core–shell systems the noble metal core provides large enhancement of the Raman signals of nearby molecules, and the inert shell isolates the metal nanoparticle from the environment (see Fig. 8). Owing to its potential, there has been growing interest in using SHINERS for the characterization of heterogeneous catalysts during the last years,[374-383] as will be illustrated by examples from the literature.

Recently, the Tian group used SHINERS to obtain detailed insight into the oxidation of CO over silica-supported PtFe and Pd catalysts under working conditions (*operando* approach). For Raman enhancement, SHIN-based catalysts were prepared, by first coating a Au nanoparticle (diameter: 55, ~120 nm) with an ultrathin conformal silica shell (~2 nm), and then depositing the active catalyst particles (a few nanometres in size) onto the silica surface (see Fig. 25a).[377] The silica shell needs to be free from pinholes to avoid any interaction of reactant molecules or the catalyst with the Au core. Figures 25b and c show SHINER spectra (633 nm excitation) during CO oxidation over Pd nanoparticles as a function of temperature for different ratios of reactants in the feed: $CO/O_2$ = 1/10 (b) and $CO/O_2$ = 1/1 (c). At lower temperatures, there are pairs of peaks at 360 and 1935 $cm^{-1}$ and at 490 and 2061 $cm^{-1}$, which can be attributed to the Pd–C and C–O stretching vibrations of bridged and linear CO adsorbed on Pd, respectively. At higher temperatures their intensity declines, whereas new Raman features are

observed at 860 and 955 $cm^{-1}$ and at 1165 $cm^{-1}$, resulting from peroxide and superoxide species, respectively. Above 110°C, two additional peaks appear, at 433 and 645 $cm^{-1}$, which originate from Pd–O stretching vibrations of surface PdO. While spectra do not vary significantly for changing $CO/O_2$ ratio, the Pd–O and molecular oxygen features are weaker than the CO bands when $CO/O_2$ ratio increases (e.g. at 130°C) as expected. Because the CO oxidation activity also decreases with increasing $CO/O_2$ ratio, CO adsorption has been proposed to inhibit $O_2$ activation on the catalyst, thus leading to a surface preferentially covered by CO. As outlined above, the SHINERS approach significantly increases the sensitivity to enable the *operando* observation of surface and adsorbate species, such as surface oxides, peroxides/superoxides, and adsorbed CO, providing new mechanistic insight into the mode of operation of heterogeneous catalysts.

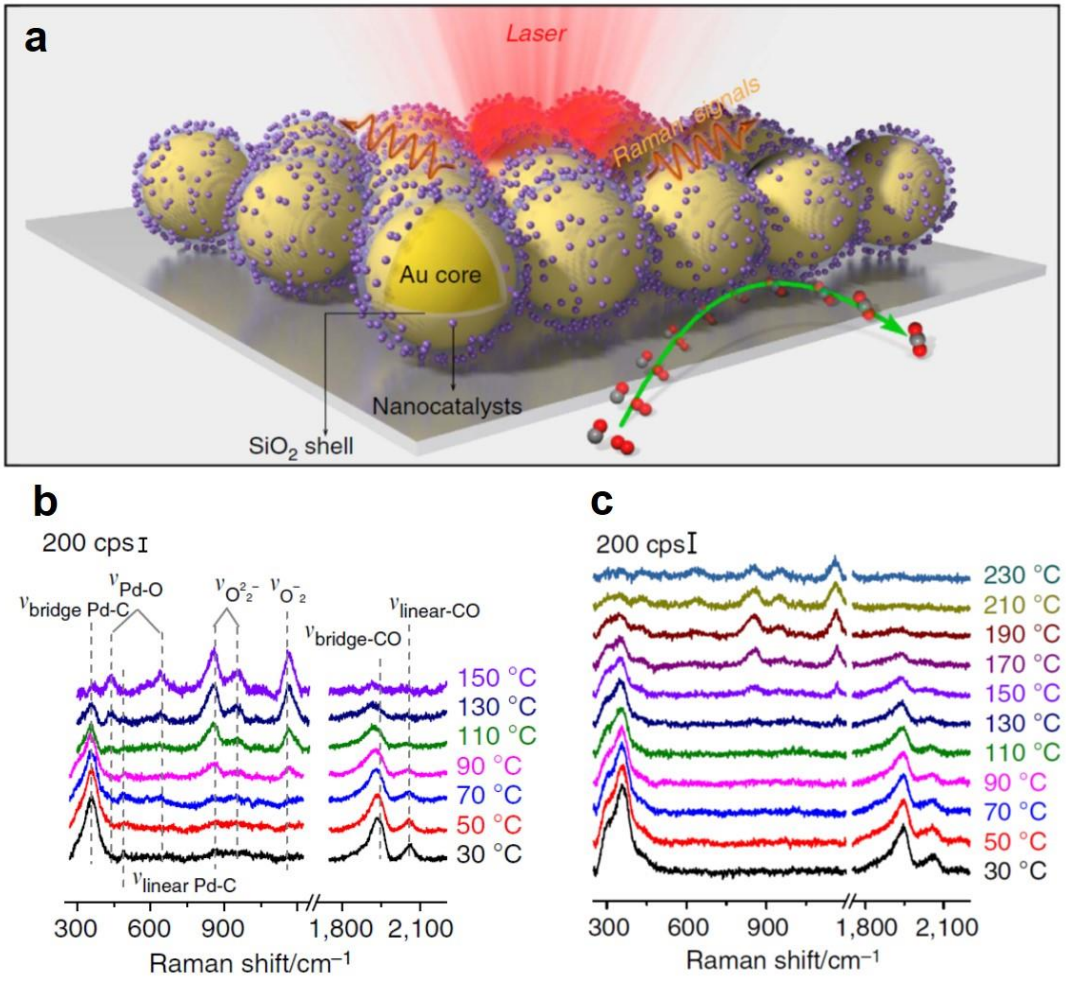

**Fig. 25** *Operando* SHINERS applied to silica-supported PtFe and Pd catalysts. **(a)** Principle of SHINERS based on Au@$SiO_2$ particles. SHINER spectra during CO oxidation over Pd catalysts at different temperatures for **(b)** $CO/O_2$ = 1/10 and **(c)** $CO/O_2$ = 1/1. For details see text. Modified with permission from ref. 377, copyright 2017, Springer.

The observation of CO-related adsorbate features has also been reported by the Weckhuysen group for CO hydrogenation reactions over SHIN-based Rh- and Ru catalysts, as well as Rh–O subsurface species in the case of Rh catalysts.[378] The best Au@$SiO_2$ and Au@$TiO_2$ SHINs in terms of both overall stability (air stability: up to 400°C) and Raman signal intensity at 785 nm laser excitation (enhancement factors: $10^4$–$10^5$) were reported to be 76 nm Au NPs with 2.6 nm $TiO_2$ and 2.2 nm $SiO_2$ coating.

Recently, Hartman *et al.* combined SHINERS with luminescence thermometry for local temperature measurements and applied this approach to the syngas conversion into hydrocarbons and $C_{2+}$ oxygenates over silica-supported Rh and RhFe catalysts (see Fig. 26).[380] For a Rh/Au@$SiO_2$ catalyst/SHINs (see Fig. 26a), the production of methane and propane/propylene was observed starting at around 260°C using mass spectrometry (see Fig. 26b), in addition to $CO_2$ and $H_2O$. *Operando* SHINER spectra in Fig. 26c show a band at ~480 $cm^{-1}$ with a shoulder at ~410 $cm^{-1}$, which have been assigned to the stretching vibration of linear (Rh-CO) and bridged ($Rh_2$-CO) CO adsorbed on Rh. The ratio between the two species changes with temperature (see Fig. 26d), reaching a value of 0.35 at the onset of the reaction at 260°C and a final value of 0.45 at around 300°C. The ratio change results from the intensity decrease at ~480 $cm^{-1}$, suggesting the desorption of linear species, while bridged species stay on the surface. At higher wavenumbers, the *operando* SHINER spectra show C–O stretching features of adsorbed CO and intermediates/reaction products with assignments in Figs. 26e–i. At around 1780 $cm^{-1}$, a (previously unreported) prominent band is observed, which the authors

attribute to tilted carbonyl species on the $Rh/SiO_2$ interface and consider to be probable precursors for the hydrogen-assisted CO dissociation.[380]

Very recently, silica–supported Ni catalysts were studied *in situ* during acetylene hydrogenation of acetylene using $Au@SiO_2$ SHINs.[382] In adsorption experiments with acetylene, a previously unreported band at ~1890 $cm^{-1}$ is observed, which is related to (Ni-)C≡C stretching, and which disappears upon hydrogenation. At the same time, new bands associated with ethylene and ethylidine on Ni were identified. In another recent *in situ* SHINERS study from the same group, $Pt/Au@SiO_2$ catalyst/SHINs were employed to study the sequential gas-phase hydrogenation of phenylacetylene to styrene and ultimately ethylbenzene,[381] demonstrating the potential of SHINERS to study heterogeneously catalysed reactions of more-complex substrate molecules.

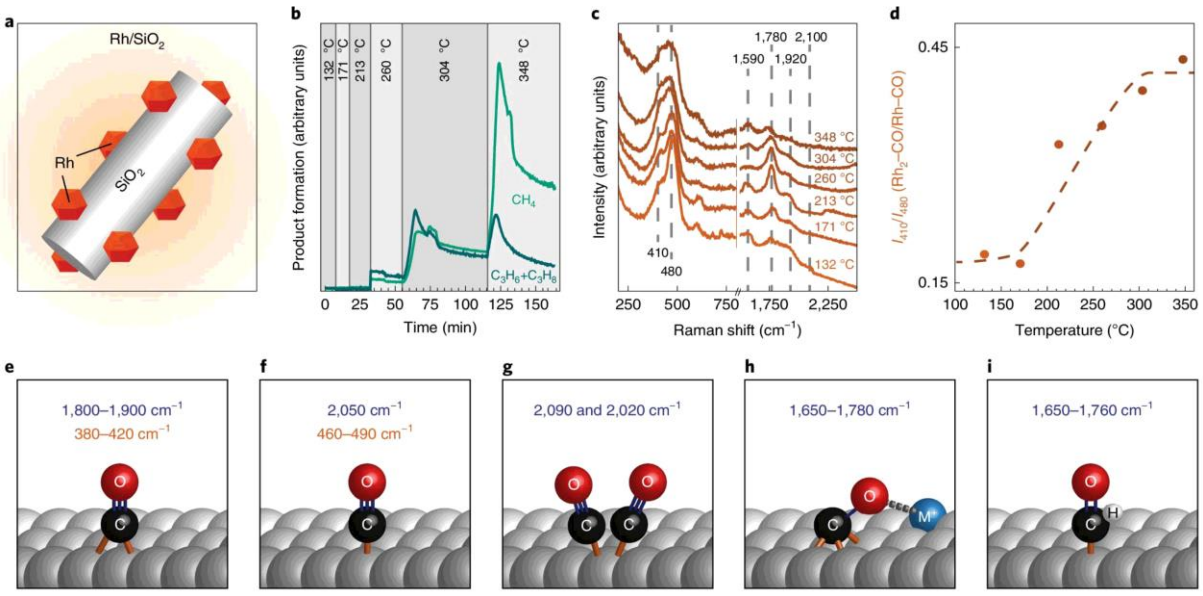


**Fig. 26** *Operando* SHINERS combined with luminescence thermometry applied to silica-supported Rh catalysts. **(a)** $Rh/SiO_2$ catalyst based on $Au@SiO_2$ SHINs. **(b)** Catalytic activity in syngas conversion at different temperatures. **(c)** SHINER spectra at different temperatures, with CO-related features indicated. **(d)** Intensity ratio of bridged and linear CO. **(e)-(i)**

Assignments of adsorbed CO on Rh surfaces. Modified with permission from ref. 380, copyright 2019, Springer Nature.

SHINERS has also been applied to study vanadium and niobium oxide on various supports ($SiO_2$, $Al_2O_3$, $TiO_2$) using Au@$SiO_2$ SHINs, including a detailed analysis of interfacial V−O−Si vibrations (at around 940 $cm^{-1}$) on silica-supported vanadium oxide catalysts in ambient conditions and dehydrated up to 400°C.[383]

As outlined above, the SHINERS approach allows significant signal enhancements over normal Raman spectroscopy as well as surface and interface sensitivity, offering new possibilities for the characterization of catalysts and catalytic processes. Advantages of SHINERS are the strong increase in Raman signal (by a factor of up to $10^8$),[77] which allows hitherto inaccessible surface/adsorbate vibrations to be detected, the broad applicability, and the compatibility with *in situ/operando* measurements. As an effective way of applying SHINERS to heterogeneous catalysis, previous studies have employed SHINs as a support for catalytically active metals (Pt, Pd, Rh, Ru, Ni, etc.), as illustrated in Fig. 25a.[77] While in most catalytic studies Au@$SiO_2$ SHINs are applied, other SHINs, such as Au@$Al_2O_3$,[137] Au@$TiO_2$,[378] or Au@$MnO_2$,[384] have been developed. Both $SiO_2$- and $TiO_2$-based SHINs have been reported to be stable up to ~400°C. Future work may be devoted to the high-temperature stability and the development of new robust shell materials.

Recently, tip-enhanced Raman spectroscopy (TERS) has been employed for the photo-induced initiation of catalytic reactions and their spatiotemporal analysis with enhanced sensitivity. Details will be described in the following sections on time-resolved and spatially resolved Raman studies.

## 5. Time-resolved studies

There has been significant progress in various areas of time-resolved Raman spectroscopic studies related to heterogeneous catalysts. In the following, I will discuss developments regarding the monitoring of structural dynamics, recently introduced kinetic approaches, and the application of modulation excitation spectroscopy to Raman spectroscopy. The term 'structural dynamics' refers to the monitoring of the catalyst structure as a result of changes in the chemical potential, rather than the observation of the direct atom or molecule movements (ultrafast dynamics) by time-resolved (pump–probe) Raman spectroscopy. However, more recent developments in time-resolved Raman spectroscopy based on surface-enhanced CARS show that the elucidation of surface reactions, including bond breaking and making processes, may be feasible in the future.[385,386]

### 5.1 Structural dynamics

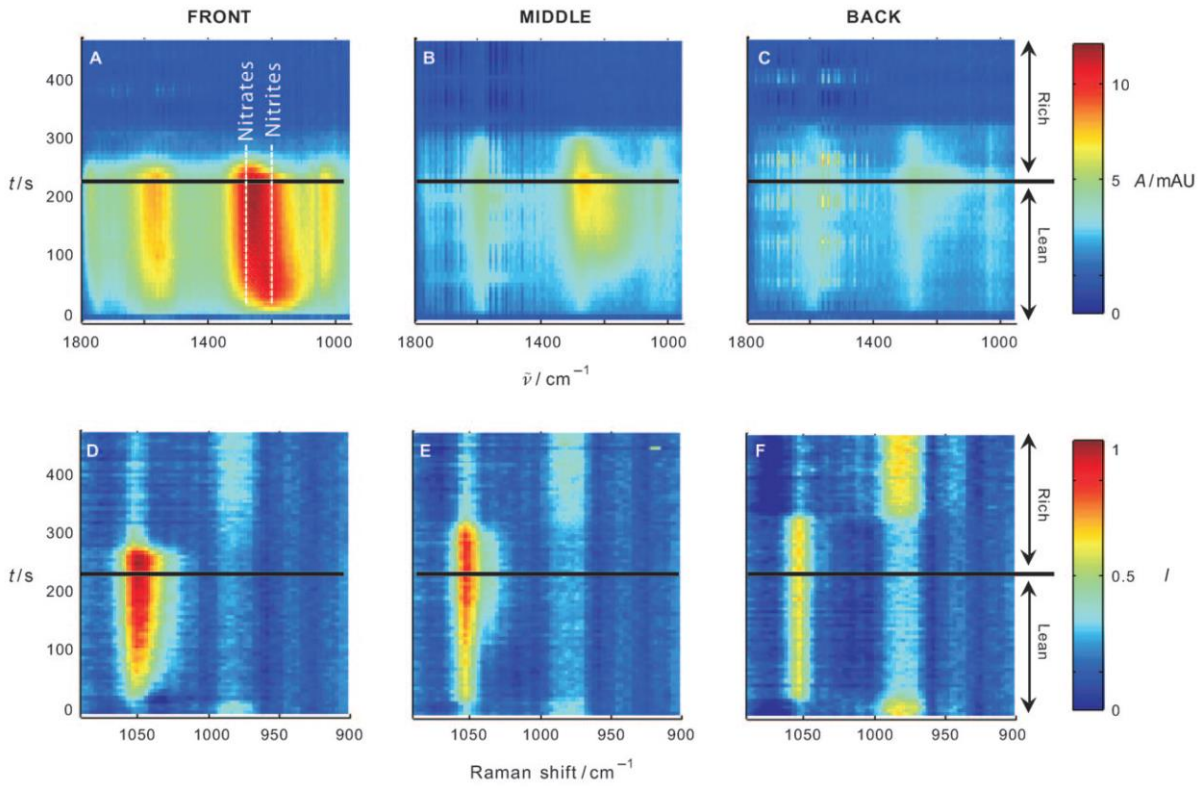

**Fig. 27** Time-resolved DRIFT (A–C) and Raman (D–E) spectra during $NO_x$ storage reduction over a Pt–Ba/$CeO_2$ catalyst (1 wt% Pt, 20 wt% Ba) at 623 K, at the front (left), middle (middle), and back (right) positions of the catalyst bed. Reproduced with permission from ref. 299, copyright 2008, Wiley-VCH.

$NO_x$ storage reduction (NSR) has attracted a great deal of attention owing to its $NO_x$ reduction capability under lean burn conditions of interest for technical applications.[387,388] In a time- and spatially resolved study the NSR over a Pt–Ba/$CeO_2$ catalyst (1 wt% Pt, 20 wt% Ba) was studied using Raman spectroscopy (at 785 nm excitation) in combination with diffuse reflectance infrared Fourier transform spectroscopy (DRIFTS), focusing on the same spot of the catalyst bed through a ZnSe window, which enabled sub-micrometre resolution.[299] Figure 27 depicts time-resolved DRIFT (A–C) and Raman (D–F) spectra during NSR operation at 623 K, that is, by first applying lean conditions ($NO/O_2/He$) for 200 s before switching to $H_2$/He atmosphere, resembling rich conditions. To elucidate the variation in storage behaviour, spectra were taken at the front (left), in the middle (middle), and at the back (right) of the catalyst bed (i.e., 0.5, 3.0, and 5.5 mm from the beginning of the catalyst bed). In fact, on moving from the front to the back of the catalyst bed, nitrite formation was delayed (see DRIFT spectra in Fig. 27A–C), and nitrite and nitrate band intensities were significantly decreased. Under lean conditions, Raman spectra (see Fig. 27D–F) show the presence of $NO_3$ stretching and bending vibrations at 1046 and 725 $cm^{-1}$, respectively, confirming the formation of a $Ba(NO_3)_2$ phase, whereas no $Ba(NO_2)_2$ is detected, thus revealing that the nitrites are merely surface species (see DRIFT spectra). Moreover, the spatially resolved Raman spectra indicate significant differences in the amount of $Ba(NO_3)_2$ formed at the different positions of the catalyst bed, namely, the most barium nitrate was detected at the front and the least at the back. During rich conditions, all nitrate-related Raman bands decreased and finally disappeared (at

about 300 s), indicative of the regeneration of the catalyst. Following the disappearance of the nitrate bands, a Raman band at 985 $cm^{-1}$ increased in intensity, assigned to bulk $Ba(OH)_2$, as evidenced by comparison with reference compounds, and it has been proposed by the authors that $Ba(OH)_2$ formation is promoted by rapid $H_2O$ generation when using hydrogen as the reducing agent.

More recently, in order to explore the detailed interaction between $NO_x$ and ceria in the context of NSR and passive $NO_x$ adsorption (PNA), detailed time-resolved *operando* Raman experiments at visible and NIR Raman excitation (515, 770 nm) have been conducted, partly in combination with UV-vis spectroscopy to allow correction of sample absorption.[300,103,28] The observed structural dynamics during $NO_x$ storage at room temperature provide direct evidence of the involvement of Ce–O surface sites, as their amount strongly influences the $NO_x$ storage capacity, as well as subsurface defects, in addition to identification of nitrite and nitrate adsorbates.[103]

Since their discovery, nanometre-sized gold particles dispersed on metal oxide supports (e.g. $TiO_2$, $CeO_2$) have been shown to be highly active for various reactions, such as low-temperature CO oxidation, preferential CO oxidation, and the (reverse) water–gas shift.[389-393] The oxidation of CO has aroused great interest from the mechanistic point of view, and both the nature of the active site and the role of (reducible) support materials (such as ceria) in catalytic activity have been vigorously debated.[394] To gain new insight into the mode of operation of ceria-supported gold catalysts (0.5 wt% $Au/CeO_2$), in particular the activation of oxygen, we performed a time-dependent *operando* Raman spectroscopic study during room-temperature CO oxidation using 532 nm excitation.[230] Figure 28A shows the temporal evolution of the spectral changes in the peroxide range during the onset of the reaction together with the catalytic activity as measured by gas-phase IR spectroscopy. Apart from peroxide, no other dynamics were observed. Each panel shows two subsequently recorded Raman spectra together with the corresponding difference spectrum. Interestingly, the sequence of difference

spectra clearly shows that initially formed peroxide species located at 847 and 881 $cm^{-1}$ are continuously consumed during the reaction, whereas the 830 $cm^{-1}$ species, which dominates the Raman spectra, is not subject to any significant changes under dynamic conditions. By comparison with the spectra of bare ceria, the peroxide bands at 881 and 847 $cm^{-1}$ have been associated with the gold–ceria interface and the ceria support (e.g., in the vicinity of the gold–ceria interface). As the peroxide bands result from oxygen adsorption on two-electron defect sites (see Section 3.3), their consumption provides clear evidence for the participation of oxygen vacancies in CO oxidation over Au/ceria at room temperature. Summarizing the mechanism, adsorbed molecular oxygen reacts with adsorbed CO, while the second oxygen atom fills the vacancy (lattice oxygen) and is then consumed by reaction with adsorbed CO, in agreement with previous theoretical predictions and recent operando DRIFTS studies.[394-396] To complete the catalytic cycle, oxygen vacancies are replenished by gas-phase oxygen.

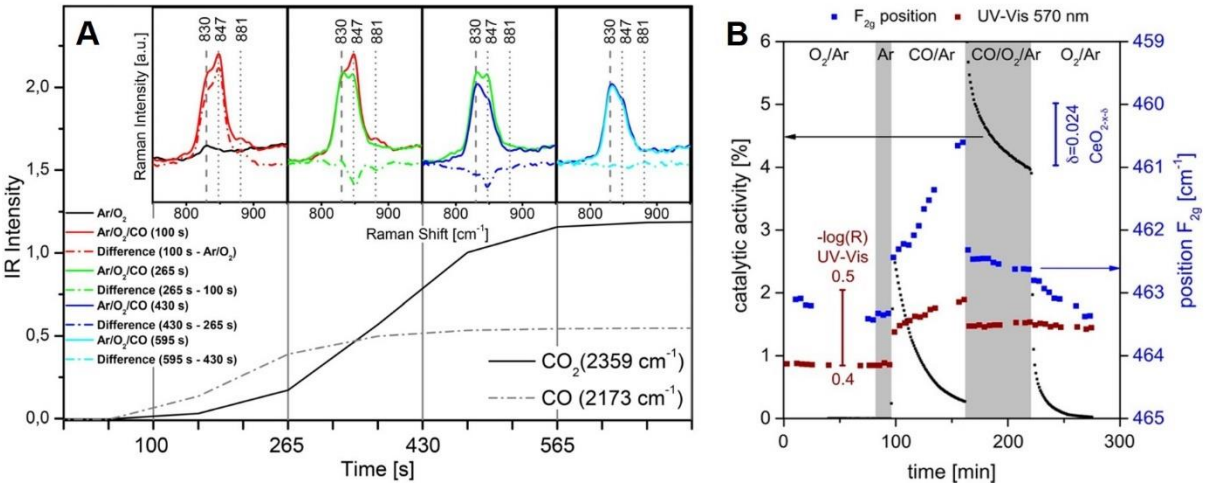


**Fig. 28 (A)** *Operando* Raman spectra of the peroxide range of 0.5 wt% Au/ceria catalyst during the onset of the CO oxidation. Each panel shows two subsequently recorded Raman spectra together with the corresponding difference spectrum. (**B)** Time-dependent Raman and UV-vis *operando* spectroscopic information for the ceria subsurface reduction state of 0.5 wt% $Au/CeO_2$ during CO oxidation after reducing pretreatment. Black squares indicate the catalytic activity of the catalyst, blue squares the position of the $F_{2g}$ Raman mode, and brown squares

the UV-vis reflectivity at 570 nm. Reproduced with permission from ref. 230, copyright 2016, Wiley-VCH and modified from ref. 259, copyright 2018, American Chemistry Society.

To further explore the participation of the ceria support in gold catalysts (0.5 wt% $Au/CeO_2$) during CO oxidation, combined *operando* Raman and UV-vis spectroscopy has been employed to monitor the surface and subsurface defect dynamics of ceria quantitatively and in real time.[259] Figure 28B shows the dependence of catalytic activity on the reduction state of the ceria support, as measured by the $F_{2g}$ position (see Section 3.2) and the absorption at 570 nm. Interestingly, the catalyst reduction is not limited to the $CeO_2$ surface (not shown) but also affects the $CeO_2$ subsurface due to oxygen mobility and charge transfer in $CeO_{2-x}$, underlining the potential of *operando* Raman spectroscopy to make available detailed insights into the support effects of supported metal catalysts.

To overcome the limitations of fluorescence interference often encountered when studying catalytic reactions on extrudates, the use of time-resolved Raman spectroscopy (TRRS) as well as its combination with SERS has been explored, by employing an intensified CCD camera with a measurement gate of about 250 ps.[397] By applying this technique to styrene synthesis with $\gamma$-$Al_2O_3$, Raman spectra of analytes at different depths were accessible, showing the principal applicability of Raman spectroscopy to industrial catalysts.

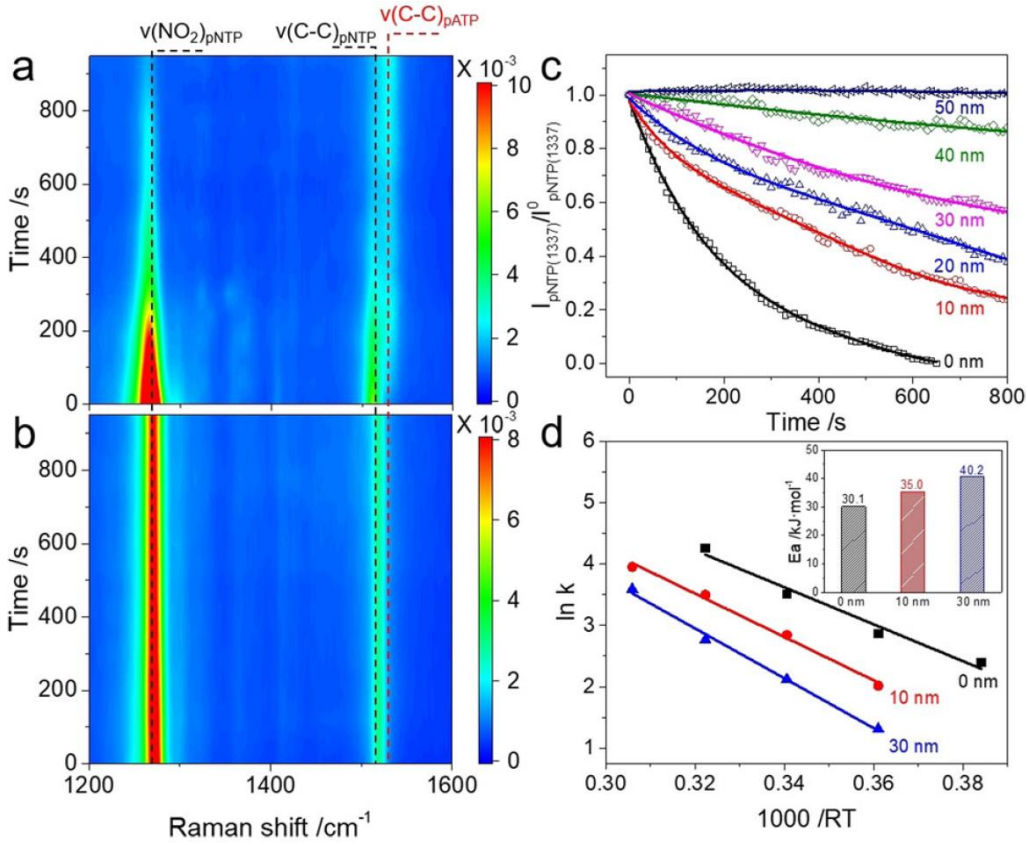


**Fig. 29** *In situ* SER spectra of the hydrogenation of pNTP on **(a)** Au/10 nm $TiO_2$/Pt and **(b)** Au/50 nm $TiO_2$/Pt at 60°C. **(c)** Time-dependent intensity of the Raman band for pNTP (at ca. 1337 $cm^{-1}$) on Au/$TiO_2$/Pt with different thicknesses of $TiO_2$ layer. **(d)** Arrhenius plot and the activation energy (inset) for the hydrogenation of pNTP over Au/$TiO_2$/Pt with different thicknesses of $TiO_2$ layer. Reproduced with permission from ref. 398, copyright 2020, Wiley-VCH.

More recently, the increased sensitivity of SERS has been exploited for monitoring catalytic reactions by time-resolved SERS and SHINERS.[376,379,398] The use of SERS has been demonstrated in the aqueous pNTP (4-nitrothiophenol, 4-nitrobenzenethiol) transformation using $NaBH_4$ as a reducing agent in the presence of Pt-containing catalysts.[399-401] As a very recent example of a solid–gas reaction, Fig. 29 presents *in situ* SERS data of the hydrogenation of pNTP on Au/$TiO_2$/Pt sandwich structures at 60°C by Wei *et al.*.[398] For Au/10 nm $TiO_2$/Pt,

Raman spectra in Fig. 29a show peaks at 1337 and 1570 $cm^{-1}$, attributed to the symmetric stretch of the nitro group and the phenyl ring modes of pNTP, respectively, which decrease gradually during the course of the reaction. This is accompanied by the appearance of a new Raman band at 1586 $cm^{-1}$, which is assigned to the benzene ring mode of pATP (p-aminothiolphenol, 4-aminobenzenethiol), implying the conversion of pNTP into pATP by hydrogen spillover from Pt to $TiO_2$, finally reaching the Au surface, consistent with previous results.[376] Interestingly, for Au/50 nm $TiO_2$/Pt no significant spectral changes are observed during hydrogenation (see Fig. 29b), indicating that the hydrogen spillover distance on $TiO_2$ is less than 50 nm. In fact, as shown in Fig. 29c in more detail, an increase in the $TiO_2$ layer thickness from 0 to 50 nm leads to a gradual decrease of the pNTP hydrogenation rate. The corresponding Arrhenius plots in Fig. 29d demonstrate a slight increase of the activation energy with the layer thickness, underlining the importance of hydrogen spillover for hydrogenation. DFT calculations on water-mediated hydrogen transfer between $TiO_2$ bridge oxygen confirm the magnitude of the activation energy.

Owing to the use of plasmonic nanoparticles for SERS applications, their properties are of relevance for the course of the catalytic reaction, and may be exploited specifically in plasmon-based catalysis.[402,136,403,340] In fact, the excitation of a localized surface plasmon resonance (LSPR) may result in local (photothermal) heating, local field enhancement, and the formation of charge carriers, whereby one or more property may induce chemical transformations. This is illustrated by Fig. 30, which depicts time-resolved SER spectra of the plasmon-induced protonation of 4-mercaptopyridine (4-MPY, 4(1H)-pyridinethione) in the presence of silver nanoparticles monitored under ambient conditions using 532 nm excitation.[404] The spectra of the unprotonated molecule shown in Fig. 30a are characterized by bands at 1006 $cm^{-1}$ (ring breathing), 1092 $cm^{-1}$ (ring breathing/C–S), 1211 $cm^{-1}$ (β(CH)/δ(NH)), and 1575 $cm^{-1}$ (ring stretching), whereas the protonated molecule shows a characteristic ring-breathing feature at 1608 $cm^{-1}$. Figure 30b gives an enlarged view of the

SERS intensity within the wavenumber range 1550–1630 $cm^{-1}$. To initiate the protonation a minimum intensity of the surface plasmon is required, which can be controlled by either the incident laser power or the excitation wavelength. Using tip-enhanced Raman spectroscopy (TERS) from a silver-coated AFM tip (~10 nm) positioned above a transparent gold nanoplate with a monolayer of 4-MPY, a much faster (instantaneous) protonation was observed than with SERS.[404] This behaviour has been explained by the increased enhancement due to the field confinement in the Ag particle–on–Au metal surface geometry ('gap-mode'), in addition to the efficient electron transfer from tip to sample induced by the tip–sample nanogap.[405,406]

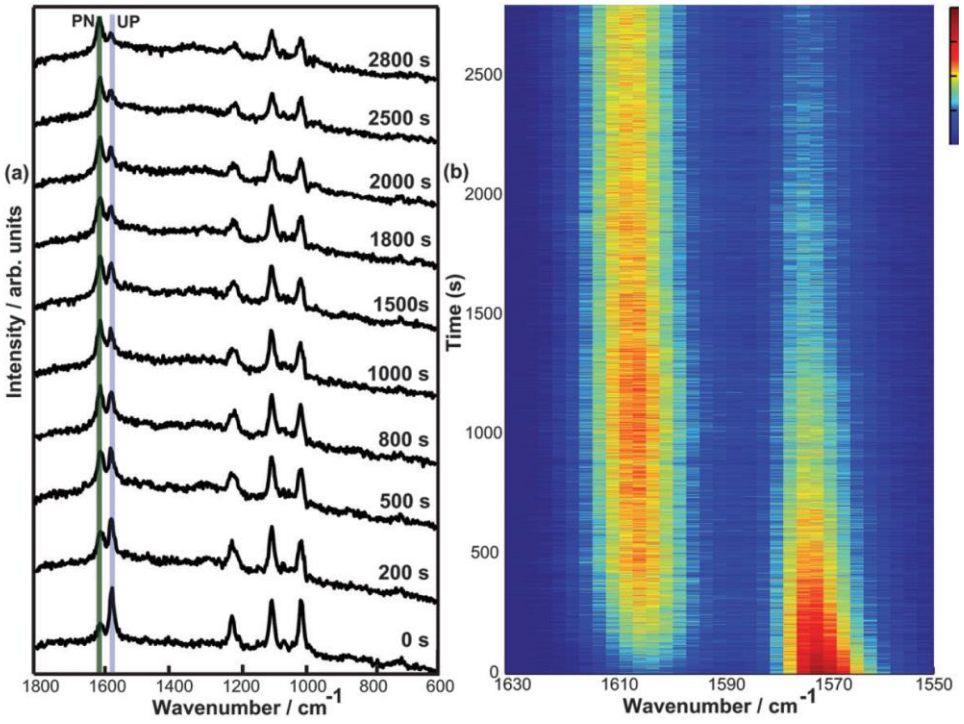


**Fig. 30 (a)** Selected time-dependent SERS spectra of 4-MPY under 532 nm/125 mW laser radiation, acquisition time of 1 s. **(b)** SERS intensity plot of the full series in the wavenumber range 1550–1630 $cm^{-1}$. UP and PN refer to unprotonated and protonated N. For details see text. Reproduced with permission from ref. 404, copyright 2014, Royal Society of Chemistry. Wiley-VCH.

The increased sensitivity of TERS has been utilized by van Schrojenstein Lantman to monitor the plasmon-induced reduction of a self-assembled monolayer of pNTP molecules adsorbed on gold nanoplates.[145] The catalytic reaction was induced at the apex of the tip with 532 nm excitation, while 633 nm laser light was used to follow the transformation from pNTP to p,p′-dimercaptoazobisbenzene (DMAB, 4-(dimethylamino)benzaldehyde). The use of two different wavelengths means the reactants and the photo-induced reaction are probed separately, that is, other molecular effects such as monolayer diffusion can also be studied. In contrast to SERS, the TERS technique with its spatial resolution enables the study of chemical reactions on a single-particle level (see Section 6).

### 5.2 Kinetic approaches

Knowledge of spatial concentration gradients in reactors is important for a detailed understanding of the outcome of heterogeneous catalytic reactions.[407] While earlier work had reported spectroscopic profiling for fixed bed reactors,[408,409] a simultaneous measurement of spatially resolved kinetic and spectroscopic profiles in a fixed bed tubular reactor has become accessible by a new capillary-based experimental approach (see Section 2.6).[165] The potential of this approach has been demonstrated by Geske *et al.* for ethane ODH measured throughout a $MoO_x/\gamma$-$Al_2O_3$ (50 wt%) catalyst bed at 1 bar. Figure 31 presents the species and temperature profiles (A) and Raman spectra recorded along the catalyst bed (B). As shown in Fig. 31A, the main reaction products in the oxidation zone are $H_2O$, $C_2H_4$, CO, and $CO_2$. The formation of $H_2$ is only detected when gas-phase oxygen is largely consumed. The *in situ* Raman spectra (at 647 nm excitation) shown in Fig. 32B were recorded with a spatial resolution of about 1 mm and are characterized by O=Mo (993 $cm^{-1}$) and Mo–O–Mo (821 $cm^{-1}$) vibrations, which are characteristic for $MoO_3$. Interestingly, the combined spatially resolved kinetic and

spectroscopic measurement shows that the $MoO_3$ Raman signals vanish at the position where gas-phase oxygen is almost fully consumed (at around 19 mm). The decrease of the Raman signal is attributed to the reduction of the catalyst to $MoO_2$, originating from the much lower Raman cross section of the dioxide and strong self-absorption.[410] However, detailed analysis of the Raman spectra reveals the coexistence of the trioxide and the dioxide phase at the position of full oxygen conversion,[411] as further confirmed by *ex situ* XRD analysis. Summarizing, the results of the combined kinetic and spectroscopic measurements demonstrate that ethane ODH occurs only in the presence of gas-phase oxygen, while further oxidation of ethylene to $CO_2$ results from a subsequent reaction step by lattice oxygen of $MoO_3$. In the absence of gas-phase oxygen, which leads to a reduction of $MoO_3$ to $MoO_2$, deep oxidation of ethylene to $CO_2$ is the only reaction observed; oxidation of CO and $C_2H_6$ by lattice oxygen does not occur.

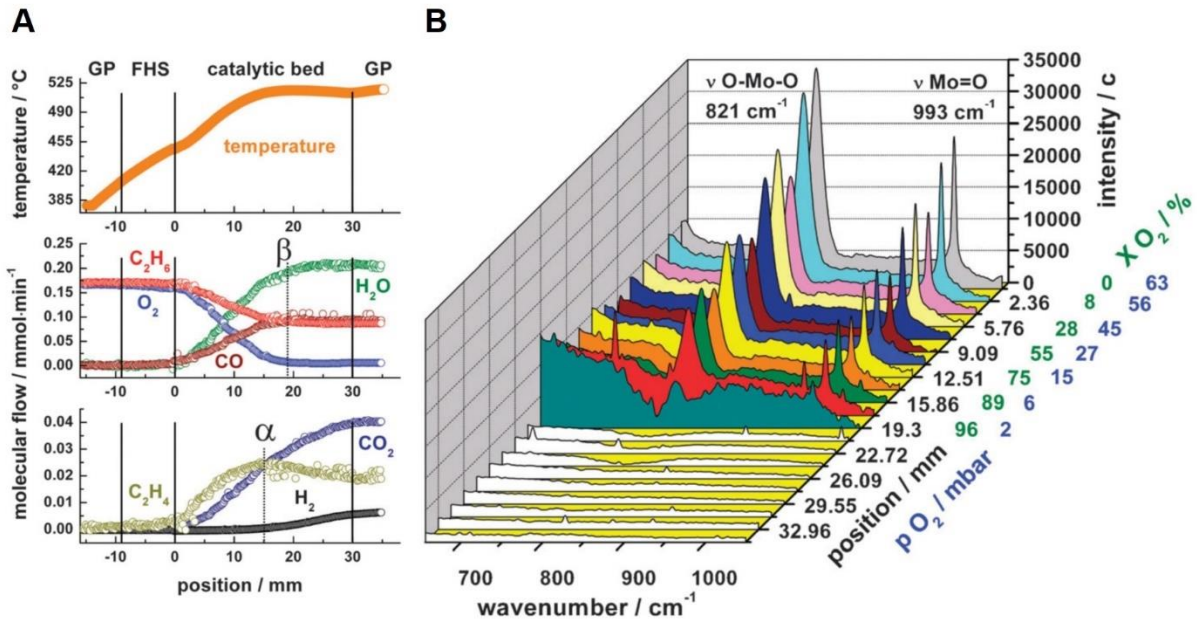


**Fig. 31** **(A)** Species and temperature profiles for ethane ODH measured throughout a $MoO_x/\gamma$-$Al_2O_3$ sphere bed at $p$ = 1 bar. Point α marks the maximum $C_2H_4$ concentration, Point β marks the position of complete $O_2$ conversion. GP denotes the gas phase before and after the catalyst bed and FHS the ceramic front heat shield. **(B)** Corrected *in situ* Raman spectra along the

catalyst bed. $MoO_3$ Raman signals vanish at the position where gas-phase oxygen is almost fully consumed. Reproduced with permission from ref. 165, copyright 2013, Royal Society of Chemistry.

Earlier work had reported on combined *in situ* Raman and kinetic investigations to identify intermediate species in ethanol ODH over supported molybdenum oxide catalysts.[412,413] Recently, a novel Raman spectro-kinetic approach has been introduced by Moncada *et al.*, by combining *operando* Raman spectra with transient reaction kinetics, allowing redox reaction rates to be measured directly from Raman spectra.[210] Using such an approach, rates can be correlated to a specific catalytic site, in contrast to integral reaction rates obtained by gas-phase analysis. The potential of the approach has been demonstrated for the redox properties of vanadium oxide in supported $(VO_x)/(NbO_y)/SiO_2$ catalysts. To this end, Fig. 32 shows the evolution of the vanadyl (V=O) stretching vibration during (re)oxidation at 500°C after a previous reduction treatment using $H_2$ at 500°C overnight. Figure 32A shows the dependence of reoxidation rate on niobia loading, while Figure 32B provides the detailed Raman spectra (at 405 nm excitation) as a function of oxygen pulse number for the $4V/1.4Nb/SiO_2$ catalyst. In summary, the results from the Raman spectro-kinetic measurements reveal that vanadium and niobium oxide exhibit synergetic effects, that is, that the presence of niobia at the lowest loadings accelerates the formation of the V=O group during oxidation.

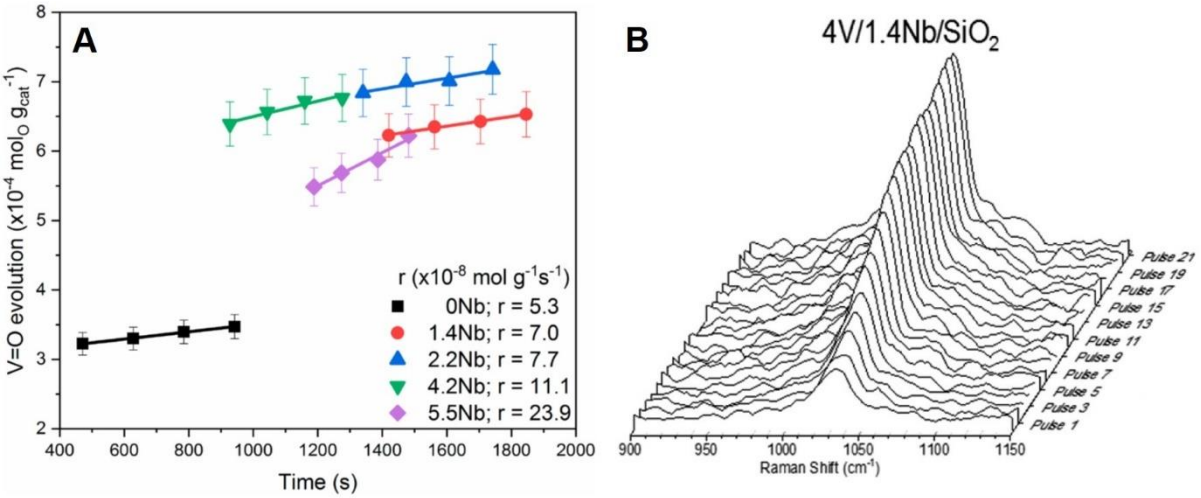


**Fig. 32** **(A)** Evolution of the vanadyl group monitored by Raman spectroscopy during oxidation of $(VO_x)/(NbO_y)/SiO_2$ catalysts. **(B)** Detailed Raman spectra as a function of pulse number for $4V/1.4Nb/SiO_2$ (right). Reaction conditions: $N_2$ (carrier) flow, 30 mL $min^{-1}$; temperature, 500°C; concentration, 50% $O_2/N_2$; pulses of 100 μL. The legend shows the rate of oxidation obtained from the slope of the curves. Modified with permission from ref. 210, copyright 2018, American Chemical Society.

While studies of heterogeneous catalysts in the liquid phase are not addressed in this review, I would like to mention in passing that there are a large number of studies using Raman spectroscopy to monitor liquid-phase reactions and obtain kinetic data, a few examples of which are given as references.[414-419,351,420,421] Some of these approaches may also be of interest for Raman studies of solid/gas reactions such as microreactor-based high-throughput testing of catalysts.[421] In fact, microreactors[422-425] and high-throughput systems[426] have been employed separately for Raman spectroscopic characterization of catalysts in solid/gas reactions.

### 5.3 Modulation excitation spectroscopy

As discussed above, steady-state Raman experiments can reveal important structural information on heterogeneous catalysts. However, it has been a challenge to isolate the structure

of perturbed (responsive) from spectator (stationary) species. Strategies to overcome that limitation are based on experiments under transient conditions, such as the modulated excitation (ME) technique.[427-430] In modulation excitation spectroscopy (MES), the concentration of one reactant (or the temperature, etc.) is varied periodically while simultaneously spectra are recorded with sufficient time resolution. The spectra in the time domain are then converted into the phase domain – referred to as phase-sensitive detection (PSD) – containing only signals of those species responding to the applied modulation. Hence, signals of spectator species can be efficiently removed, increasing the sensitivity towards the perturbed species.

Very recently, Nuguid *et al.* have applied the MES-PSD approach to Raman spectroscopy to enhance the mechanistic understanding of $V_2O_5/TiO_2$ catalysts in the selective catalytic reduction (SCR) of NO with $NH_3$ at 250°C.[208] This is illustrated in Fig. 33, which presents time-resolved Raman spectra (at 785 nm excitation) of a 2 wt% $V_2O_5/TiO_2$ catalyst (2 $VO_x/nm^2$), dominated by the characteristic features of $TiO_2$ anatase at 395 $cm^{-1}$ ($B_{1g}$), 516 $cm^{-1}$ ($B_{1g}$, $A_{2g}$), and 636 $cm^{-1}$ ($E_g$), whereas the weak band at ~800 $cm^{-1}$ is the overtone of the $B_{1g}$ mode (see Fig. 33a). The presence of amorphous vanadium oxide is evidenced by features in the vanadyl region (1010−1040 $cm^{-1}$) and the absence of a band at around 995 $cm^{-1}$, characteristic of crystalline $V_2O_5$ (see Fig. 33b). To perform MES experiments, the $NH_3$ reactant was periodically switched on and off, leading to periodic changes in the SCR activity. Under the conditions of the experiment (250°C, NO steady-state conversion: 26%) the surface of the catalyst was populated mainly by adsorbed $NH_3$ and water. While the time-resolved spectra do not indicate any significant spectral changes, after PSD, both $VO_x$ and $TiO_2$ signals responded to the changes in the gas-phase composition (see Figs. 33c and d), implying the participation of both the $VO_x$ species and the $TiO_2$ support in the SCR process. It should be noted that the broad vanadyl feature in the time-resolved spectra is present as a narrower and

well-defined peak in the phase-resolved spectra (see Fig. 33d), indicating that only some of the $VO_x$ species were actively participating in the reaction.

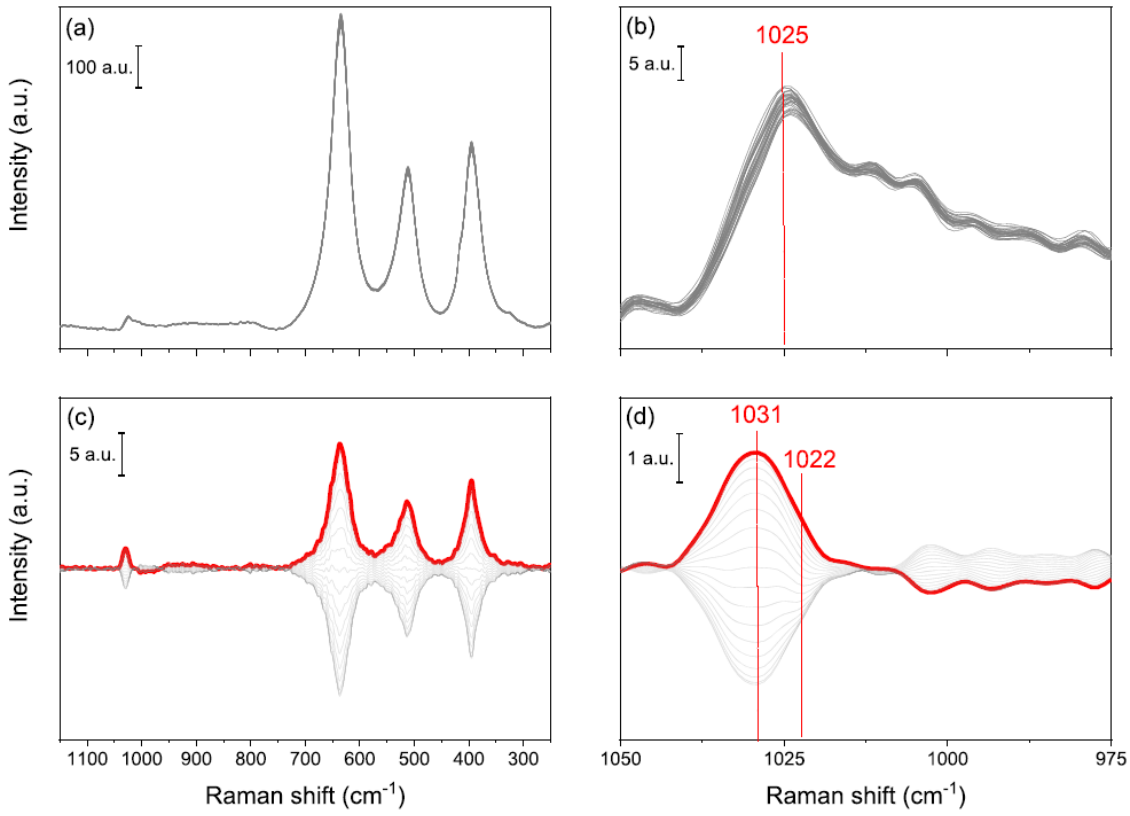


**Fig. 33 (a, b)** Time-resolved Raman spectra and **(c, d)** corresponding phase-resolved spectra of 2 wt% $V_2O_5/TiO_2$ at 250°C during 30 s pulses of 500 ppm $NH_3$ in a gas feed of 500 ppm NO, 2 vol% $H_2O$, and 5 vol% $O_2$ balanced in Ar. Modified with permission from ref. 208, copyright 2019, American Chemical Society.

Interestingly, in contrast to steady-state experiments, in which the vanadyl mode is located at ~1016−1026 $cm^{-1}$, in the phase-resolved spectra the maximum occurs at 1031 $cm^{-1}$, typical for $VO_x$ species in oxygen flow, that is, in the absence of adsorbates. The perturbed $VO_x$ species are therefore proposed to be coordinatively unsaturated, as opposed to the majority of vanadium oxide, which is redshifted to ~1026 $cm^{-1}$, indicating its engagement in

adsorption/coordination (see Figs. 33b and d). In the phase-resolved spectra, the authors identify a smaller $VO_x$ feature at around 1022 $cm^{-1}$, which varies asynchronously with the main contribution and is suggested to originate from $VO_x$ bound to a ligand, probably $NH_3$. Summarizing, the application of Raman MES and PSD has contributed to the mechanistic understanding of the SCR reaction by providing information not accessible by steady-state Raman experiments. Due to its potential to provide insight into the dynamical behaviour of heterogeneous catalysts, it is expected that the Raman MES-PSD approach will be further developed and applied to other catalytic processes in the near future.

## 6. Spatially-resolved analysis of catalytic materials

Since the introduction of Raman microscopy more than 30 years ago,[33] spatially resolved Raman analysis has undergone dramatic developments during recent years, now enabling a spatial resolution below 1 nm sufficient to resolve even single molecules.[431-435] In the following, more recent advances regarding the spatially resolved characterization of catalytic materials will be discussed, including the use of coherent anti-Stokes Raman scattering (CARS) microscopy, stimulated Raman scattering (SRS) microscopy, tip-enhanced Raman spectroscopy (TERS), and shell-isolated TERS. Older developments in the field have been reviewed in 2010[436] and 2012,[68] and, with respect to TERS-related developments, in 2010[65] and 2016.[74]

More recent research activities in spatially resolved analysis have largely focused on the use of nonlinear and plasmon-enhanced Raman scattering. In the past, the orientation of guest molecules inside zeolite pores has been studied using a variety of experimental techniques, including IR, Raman, second harmonic generation (SHG), single and two-photon fluorescence, and UV-vis spectroscopy.[437-440,67] For spatially resolved imaging, nonlinear fluorescence and

SHG microscopy approaches,[441,442] as well as CARS microscopy,[443] have been employed. For an introduction to the principle of CARS please refer to Section 2.5. Domke *et al.* have applied mupliplex CARS (mCARS)[444] to the 3D characterization of the local geometric structure of 2-chlorothiophene (2CT) in zeolite ZSM-5 pores,[445] which is of interest in the context of catalytic desulphurization of fuels.

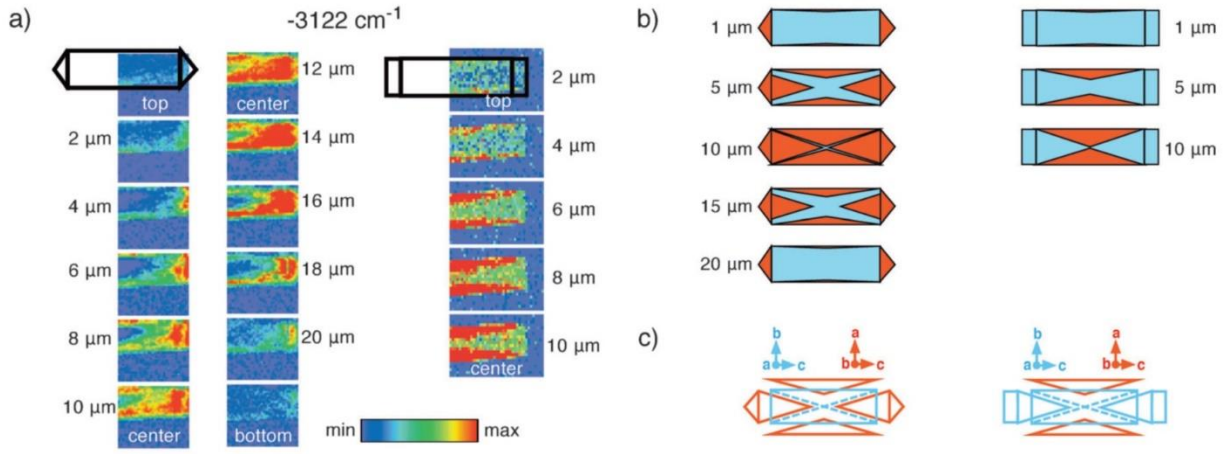


**Fig. 34** (**a)** Observed patterns of the relative intensity of the 3122 $cm^{-1}$ band in 2D slices of 2-chlorothiophene/H-ZSM-5 viewed along the roof top (left) or perpendicular to the roof top (right), moving down from the top to the centre to the bottom of the crystal with a step size of $D_z$ = 2 mm; beam polarization perpendicular to the *c*-axis. (**b)** Expected intensity patterns for the respective beam polarizations with respect to the orientation of the zeolite's subunits as depicted in **(c)**. Modified with permission from ref. 445, copyright 2012, Wiley-VCH.

Figure 34 depicts 2D slices of 2CT/H-ZSM-5 viewed along the roof top (a, left) or perpendicular to the roof top (a, right), based on the relative intensity of the C–H stretching mode of 2CT at 3122 $cm^{-1}$. The observed patterns are spatially inhomogeneous at different crystal depths, representing the expected intensity patterns (Fig. 34b), based on the segmented structure of the ZSM-5 particle (Fig. 34c). From the spectroscopic information, the molecular

ordering of 2CT has been proposed as head-to-tail with the molecular plane in the *bc* plane of the zeolite (straight pores). Future applications of this approach may include kinetic studies on the diffusion of reactants within zeolite pores. Moreover, by expanding the CARS approach towards time-resolved Raman experiments and by combination with enhancement effects from SERS, even elementary steps of surface reactions may be accessible.[385,386]

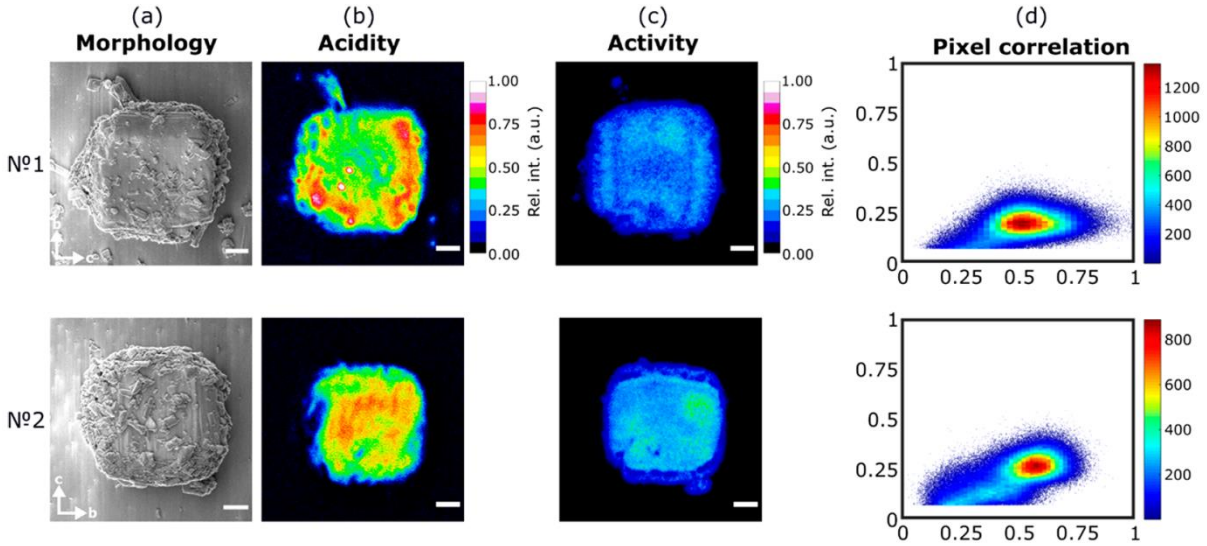


**Fig. 35** **(a)** SEM images of mordenite crystals. **(b)** SRS images (1006 $cm^{-1}$) of pyridinium ion adsorbed at Brønsted acid sites in the crystals after evacuation at 150°C. **(c)** CFM image of the furfuryl alcohol oligomers formed after 20 min of reaction. **(d)** Correlation of catalytic activity (y-axis) with acid site density (x-axis). The heat map indicates the corresponding amount of correlations per bin. The scale bar in all images is 2 µm. For details see text. Modified with permission from ref. 194, copyright 2020, American Chemical Society.

Very recently, Fleury *et al.* employed SRS microscopy in combination with SEM and confocal fluorescence microscopy (CFM) to characterize dealuminated mordenite zeolite particles regarding their acid site distribution and local activity performance,[194] continuing their previous SRS studies on zeolites.[446,447] SRS microscopy was performed by using the signal

beam (700−980 nm) from the OPO and the fundamental 1064 nm beam as pump and Stokes beam, respectively. Figure 35 shows results for mordenite crystals after mild (n°1) and more extensive (n°2) dealumination. Crystals were sequentially analyzed with SRS microscopy to gain insight into the Brønsted acid site distribution (See Fig. 35b), with SEM to reveal the detailed crystal morphology (see Fig. 35a), and by CFM to image the catalytic activity of the furfuryl alcohol oligomerization (see Fig. 35c). While there are no apparent changes in the SEM images, SRS microscopy reveals intra- and interparticle heterogeneities in the distribution Brønsted acid sites assigned to local variations in the extent of the dealumination of the crystals. As shown in Fig. 35d, these local differences in acidity are correlated with the activity in a nontrivial manner, highlighting the critical role of diffusion, which is not captured by the equilibrium conditions used for the acid site probing with pyridine.

As introduced in Section 2.5, tip-enhanced Raman spectroscopy (TERS) is a variation of SERS, where the enhancement originates from a metallic scanning probe microscopy (SPM) tip. Previous TERS studies related to heterogeneous catalysts have demonstrated the high sensitivity and spatial resolution of chemical information.[144-151] The use of TERS to monitor photocatalytic reactions has been illustrated above in the context of time-resolved Raman studies (see Section 5.1).[404,145]

While this review focuses on gas–solid catalytic reactions, there have been significant developments in solution-based TERS, which will have an impact on other areas of catalysis, and will therefore be described in the following. In fact, to overcome the limitation of metallic tips, which can potentially interfere with the reaction under study, as well as the influence of contaminations, recently, metallic Ag and Au TERS tips protected by a thin 2 nm $SiO_2$ layer produced by atomic layer deposition (ALD), that is, shell-isolated TERS tips, have been introducedby Huang *et al.*.[448] Figure 36 compares TER spectra using bare or silica shell-isolated Au tips in a solution containing pyridine to detect [4′-(4-pyridinyl)-4-biphenylyl]methanethiol (4-PBT) self-assembled on Au(111). Interestingly, in the presence of

the silica shell, no signals from pyridine and other impurities are observed. Besides, using the shell-isolated tips, both fluorescence signals and tip-enhanced Raman spectra can be obtained simultaneously, and their relative intensity can be tuned by variation of the shell thickness.[448]

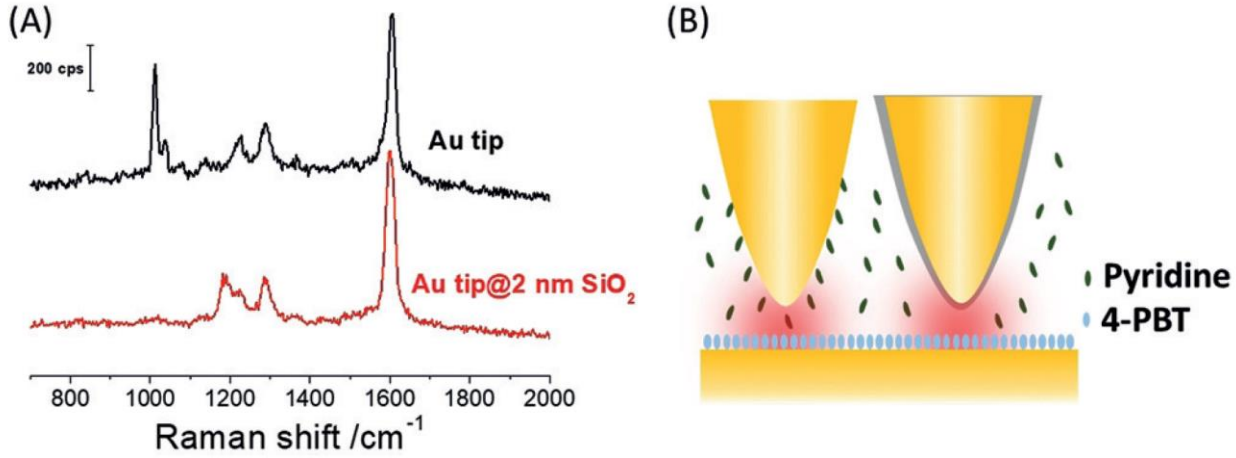


**Fig. 36** (**A)** TERS spectra of 4-PBT assembled on Au(111) acquired by a bare Au tip (black line) and a Au tip@2 nm $SiO_2$ (red line) in an aqueous solution containing 5 mm pyridine and 10 mm $NaClO_4$. The laser wavelength was 633 nm with 0.25 mW power. The acquisition time was 1 s. The tunnelling current was 200 pA and the bias voltage was 600 mV. (**B)** Schematic of TERS in a solution using a bare or shell-isolated tip. Modified with permission from ref. 448, copyright 2018, Wiley-VCH.

Very recently, AFM-TERS probes with a multilayer metal coating protected by a ~1–2 nm $ZrO_2$ layer have been applied to the spatially resolved mapping of a catalytic reaction in air and in the liquid phase.[449] Figure 37 displays TERS maps of the plasmon-assisted oxidation of p-aminothiophenol (pATP) to p,p′-dimercaptoazobenzene (DMAB) over a heterogeneous Ag substrate. Characteristic Raman bands of DMAB are located at 1142 $cm^{-1}$ ($\beta_{C-H}$), 1390 $cm^{-1}$ ($\nu_{N=N}$), and 1437 $cm^{-1}$ ($\nu_{N=N}$). Figure 37a presents the map of the 1437 $cm^{-1}$ band intensity of DMAB, showing the strong intensity at the apex position. In comparison, the SERS signal was ~12× weaker than the TERS signal measured at the same sample position with a retracted probe

(see Fig. 37c). This behaviour is indicative of a strong enhancement present at the gap between the Ag tip and Ag metal surface (see Section 5.1). The chemical inertness of the $ZrO_2$-protected TERS probe for the Ag-catalysed conversion of pATP to DMAB was confirmed by control experiments on a thin film of pATP mixed with PMMA (poly(methyl methacrylate) spin-coated on a glass substrate showing no DMAB formation. Summarizing, by protection with $ZrO_2$, a chemically inert TERS probe with significantly extended lifetime (from hours to months) has been developed that can be applied for the mapping of plasmon-induced heterogeneous catalytic reactions within a liquid environment with nanoscale spatial resolution. Besides, TERS may be employed for versatile *in situ* characterization of catalysts, including diffusion processes, catalyst heterogeneities, and/or interfacial dynamics.

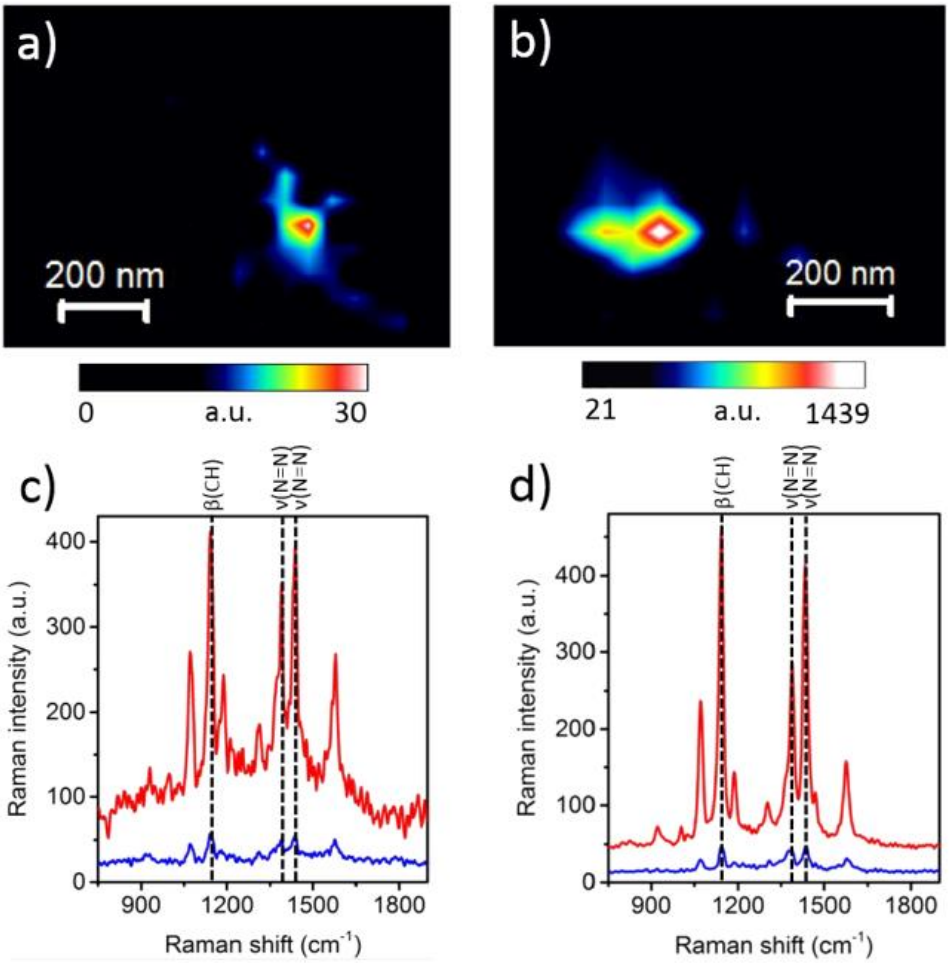

**Fig. 37** Spatially resolved mapping of plasmon-assisted oxidation of p-aminothiophenol (pATP) to p,p′-dimercaptoazobenzene (DMAB) over a heterogeneous Ag substrate using TERS. Maps of pATP → DMAB at the TERS probe apex obtained using the intensity of the 1437 $cm^{-1}$ ($\nu_{N=N}$) DMAB Raman band measured from the pATP self-assembled monolayer (SAM) on the Ag substrate in **(a)** air and **(b)** water. Integration time: 1 s. Laser power: 117 μW. Pixel size: 50 nm. **(c,d)** Corresponding TERS (red) and SERS (blue) spectra measured at the position of maximum DMAB signal in (a) and (b), with the TERS probe in contact and retracted from the sample, respectively. Integration time: 60 s (c) and 1 s (d). Modified with permission from ref. 449, copyright 2019, American Chemical Society.

Very recently, Liu *et al.* applied STM-TERS to investigate the selective hydrogenation of chloronitrobenzenethiol (CNBT) to chloroaminobenzenethiol (CABT) on a bimetallic Pd/Au(111) catalyst at room temperature with ~10 nm spatial resolution.[450] To avoid the influence of photocatalytic reactions during TERS measurements a low-power laser (70 μW, 632.8 nm) was employed. Figure 38A shows TER spectra of the CNBT reactant on Pd before (black trace) and after (red trace) exposure to $H_2$ (1.5 bar, 298 K). As a result of reaction, new Raman peaks appear at 1108 and 1586 $cm^{-1}$, indicating the formation of the CATP product, while the strong CNBT peak at 1336 $cm^{-1}$ disappears. In contrast to Pd, on Au no conversion of CNBT is observed. In Fig. 38B, the peak intensity of the 1336 $cm^{-1}$ mode in TER line scan spectra of CNBT on Pd/Au after exposure to $H_2$ is shown, indicating that the reactive region extends that of the Pd island (see topographic profile in Fig. 38C). The authors attribute this behaviour to hydrogen spillover from Pd to Au, resulting in CNBT hydrogenation not only on Pd but also extended by ~20 nm into Au regions. This study demonstrates the potential of TERS to unravel structure-activity relationships in the context of catalytic surface reactions with ~10 nm chemical spatial resolution.

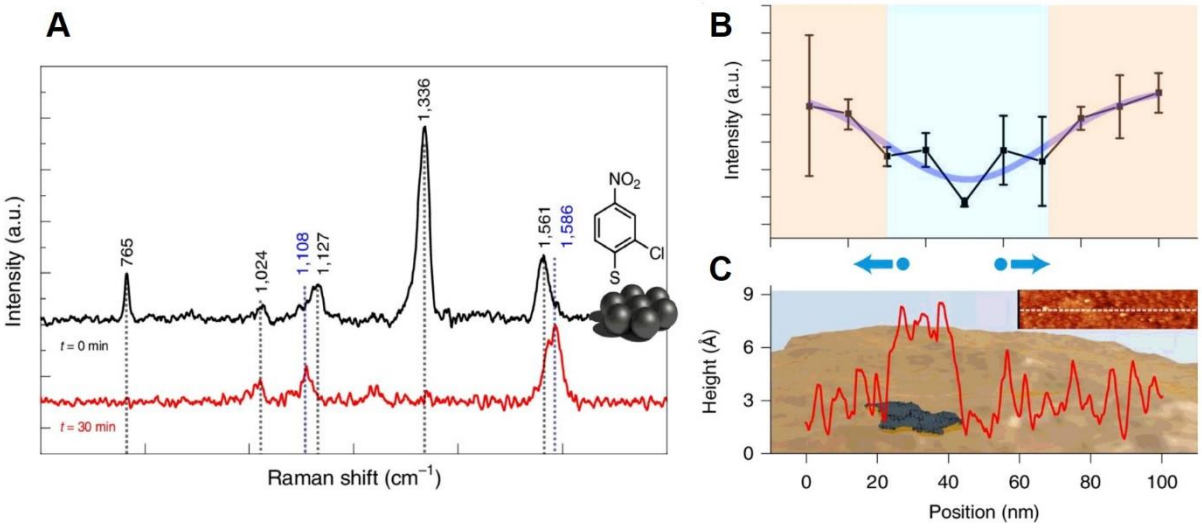


**Fig. 38 (A)** TER spectra of the CNBT reactant on Pd before (black trace) and after (red trace) exposure to $H_2$ (1.5 bar, 298 K). The Raman peaks at 1108 and 1586 $cm^{-1}$ indicate the formation of the CATP product. **(B)** Peak intensity of the 1336 $cm^{-1}$ reactant mode in TER line scan spectra of CNBT on Pd/Au after exposure to $H_2$. The blue regions indicate the reactive region. **(C)** Topographic height profiles (red line) of the surface along the dashed line in the inset of the corresponding STM images, superimposed with a schematic of the surface structure. For details see text. Modified with permission from ref. 450, copyright 2020, Springer Nature.

## 7. Concluding remarks and outlook

In this review, major developments in the use of Raman spectroscopy for the structural, temporal, and spatially resolved analysis of heterogeneous catalysts have been highlighted. A variety of new methodical developments has enabled the application of Raman spectroscopy to an extended number of heterogeneous catalyst systems on a routine basis using excitation wavelengths ranging from the UV to the NIR, including their microscopic analysis and their characterization under *in situ/operando* conditions. Notably, due to developments in efficient

fluorescence avoidance and sensitivity enhancements using UV Raman spectroscopy, characterization of catalyst materials previously difficult to access (e.g. zeolites) has now become possible on a more routine basis using commercial Raman spectrometers.

As an optical technique, Raman spectroscopy allows versatile cell design, such as the design of Raman cells closely mimicking typical plug flow reactors or the use of novel capillary-based approaches as described above. In addition, owing to the (structural) complexity of heterogeneous catalysts, the coupling with other *in situ/operando* methods is of great interest and has reached a high level of sophistication. In fact, Raman spectroscopy has been combined in an *in situ/operando* setup with EPR,[451] IR,[452,299] NMR,[452] UV-vis,[453,454] X-ray absorption spectroscopy (XAS),[455] and diffraction techniques[321] either separately or in combinations, such as EPR/Raman/UV-vis[451] or Raman/UV-vis/XAS.[455] Regarding XPS, to the best of my knowledge, there has been only a combination of *in situ* Raman spectroscopy with quasi *in situ* XPS so far.[456,457] These approaches are of interest to other areas of catalysis such as photo-[458,459] and electro-catalysis.[460-462] Especially the latter field can strongly benefit from *in situ/operando* Raman analysis and its combination with other techniques as has been demonstrated, for example, very recently in mechanistic studies on $CO_2$ reduction and the oxygen reduction reaction (ORR).[463,464]

The above combined approaches may also serve as an inspiration for future developments of *in situ/operando* characterization in other communities (e.g. sensors,[235] energy[465]). Interesting future developments include the combination of vibrational information from *in situ* Raman spectra with quantitative surface composition from *in situ* near ambient pressure (NAP) XPS or surface topography/composition from electron microscopy.

Regarding the (rational) development of improved heterogeneous catalysts, the nature of active sites plays a decisive role and new approaches are needed for their definition. In comparison, the overall level of understanding of the functioning of heterogeneous catalysts is far from that reached routinely in homogeneous catalysis. Based on the developments outlined

above, Raman spectroscopy has the potential to contribute to the further understanding of active sites in heterogeneous catalysts. The dynamic nature of active sites in many catalysts requires Raman spectra to be recorded under *in situ/operando* conditions, which is typically accompanied by little or no interference from the gas phase and is feasible even under high-pressure conditions. During the past decade, various approaches have been developed to increase the sensitivity of Raman spectroscopy by exploiting in particular resonance Raman and plasmon-based enhancements. By applying resonance Raman spectroscopy also minority species have become accessible under *in situ/operando* conditions. To this end, the use of multiple excitation wavelengths, e.g. from a wavelength-tuneable laser, will further extend the range of applications. Regarding plasmon-based signal enhancements, SERS has strongly contributed to the sensitive detection of surface species, increasing the capabilities of Raman spectroscopy to detect reaction intermediates. Recent progress in the development of SERS substrates, including hybrid systems, exploiting both electromagnetic and chemical enhancements, are expected to improve the detection limits and further increase the stability. Importantly, plasmon-based enhancements have become more widely applicable to heterogeneous catalysts due to the development of shell-isolated nanoparticle enhanced Raman spectroscopy (SHINERS). In fact, the potential of SHINERS for catalyst characterization has only begun to be explored, with potential applications in supported-metal and metal oxide catalysts. As the plasmon-based approaches focus on surface properties, the analytically challenging distinction between surface and subsurface features of bulk catalysts should be facilitated.

During the past decade there has been a large increase in the number of studies on heterogeneous catalysts that combine Raman spectroscopy with theory. To this end both classical and quantum chemical calculations have been employed to facilitate band assignments and to enable a more detailed understanding of structural changes during catalytic reactions. Moreover, there has been considerable progress in the theoretical description of resonance

Raman and surface-enhanced Raman spectra. In fact, as demonstrated more recently for vanadium oxide models, TD-DFT calculations allow correlations of electronic excitations of structural fragments/bonds to vibrational features in resonance Raman spectra. Regarding the theoretical description of molecules on metal surfaces and therefore SER spectra, besides cluster models progress has been made in the application of the framework of periodic boundary conditions to the electronic structure of metals, giving access to Raman intensities of thiols on gold surfaces, for example.

Owing to improved Raman instrumentation and the utilization of sensitivity enhancements, there have been an increasing number of time-resolved studies monitoring dynamical processes at the (sub)surface and in the bulk of catalysts. More recently, new approaches have been developed to combine spatially resolved kinetic analysis with Raman spectra and to correlate rates with specific sites. In the past, transient methods have been developed to differentiate between active and spectator species. Very recently, Raman modulation excitation spectroscopy combined with phase-sensitive detection (MES-PSD) has been successfully applied to titania-supported vanadia catalysts used for ammonia SCR to provide new mechanistic insights into the role of the titania support and vanadia phase, and further applications of this approach to other heterogeneous catalysts are expected in the near future. While modulation excitation spectroscopy probes chemical dynamics of catalysts on the timescale of seconds, femtosecond time-resolved Raman spectroscopy enables the elucidation of the ultrafast dynamics of surface reactions, that is, the direct monitoring of bond making and breaking. In fact, more recent developments based on the use of surface-enhanced CARS, namely those exploiting a combination of SERS and CARS, have shown that vibrational motion may be resolved by Raman spectroscopy even in the single-molecule limit.[386] While these experiments were conducted under well-defined conditions, future progress may allow analysis of catalytically more relevant molecules and reactions.

Exciting new developments concerning spatially resolved Raman spectroscopy have recently been reported that use tip-enhanced Raman spectroscopy (TERS). While previous TERS applications have demonstrated the high sensitivity and nanoscale spatial resolution of the method in the context of catalyst characterization, very recent studies have described the use of protected TERS tips (using e.g. $SiO_2$, $ZrO_2$) to increase the lifetime of the tips and/or to overcome the limitations of metallic tips, which may potentially interfere with the reaction under study, as well as the influence of contaminations. So far, protected TERS tips have been applied to the characterization of adsorbed (bi)phenylthiols and their plasmon-induced reaction, but applications with relevance to heterogeneous catalysis are expected to follow in the near future for silver and gold surfaces. To this end, to further enhance the Raman signal, a combination of tip-enhancement effects with CARS microscopy may be of great interest, which has been demonstrated for vibrational imaging of DNA network structures but has not been applied to adsorption or surface reactions so far.[466]

The above developments in signal enhancement enable not only a significant expansion in the applicability of Raman spectroscopy to the characterization of catalyst materials, but also open up new exciting possibilities of monitoring catalytic reactions with improved temporal and spatial resolution. Considering these opportunities, there is indeed a bright future for Raman spectroscopy in heterogeneous catalysis.

**Acknowledgements**

Financial assistance has been provided by grants from the Deutsche Forschungsgemeinschaft (DFG) and the Alexander von Humboldt foundation.

**References**


1 B. Schrader, *Infrared and Raman Spectroscopy: Methods and Applications*, John Wiley & Sons, Chichester, UK, 1995.

2 J. R. Ferraro, *Introductory Raman Spectroscopy*, Academic Press, New York, 1994.

3 *Raman Microscopy: Developments and Applications*, ed. G. Turrell and J. Corset, Academic Press, New York, 1996.

4 *Analytical Raman Spectroscopy*, ed. J. G. Grasselli and B. J. Bulkin, John Wiley & Sons, Chichester, UK, 1991.

5 J. J. Laserna, *Modern Techniques in Raman Spectroscopy*, John Wiley & Sons, Chichester, UK, 1996.

6 R. L. McCreery, *Raman Spectroscopy for Chemical Analysis*, John Wiley & Sons, Chichester, UK, 2000.

7 E. Smith and G. Dent, *Modern Raman Spectroscopy - A Practical Approach*, John Wiley & Sons, Chichester, UK, 2004.

8 R. P. Cooney, G. Curthoys and T. T. Nguyen, in *Advances in Catalysis, vol. 24*, ed. D. D. Eley, H. Pines and P. B. Weisz, Academic Press, New York, 1975, pp. 293–342.

9 T. A. Egerton and A. H. Hardin, *Catal. Rev.*, 1975, **11**, 71–116.

10 M. J. F. Leroy, M. Burgard, and A. Müller, *Bull. Soc. Chim. Fr.*, 1971, **4**, 1183.

11 A. Müller, N. Weinstock and H. Schulze, *Spectrochim. Acta*, 1972, **28A**, 1075.

12 W. Organowski, J. Hanuza, B. Jezowska-Trzebiatowska and J. Wrzyszcz, *J. Catal.*, 1975, **39**, 161–172.

13 G. T. Pott and W. H. J. Stork, in *Preparation of Catalysts I*, ed. B. Delmon, P. A. Jacobs and G. Poncelet, Elsevier, Amsterdam, 1976, pp. 537–553.

14 F. P. J. M. Thomas, R., Moulijn, J.A., Kerkhof, *Recl. des Trav. Chim. der Pays-Bas*, 1977, **96**, 134.

15 F. R. Brown, L. E. Makovsky and K. H. Rhee, *J. Catal.*, 1977, **50**, 162–171.

16 H. Knözinger and H. Jeziorowski, *J. Phys. Chem.*, 1978, **82**, 2002–2005.

17 F. R. Brown, L. E. Makovsky and K. H. Rhee, *J. Catal.*, 1977, **50**, 385–389.

18 J. Medema, C. van Stam, V. H. J. de Beer, A. J. A. Konings and D. C. Koningsberger, *J. Catal.*, 1978, **53**, 386–400.

19 F. Roozeboom, J. Medema and P. J. Gellings, *Z. Phys. Chem. N. F.*, 1978, **111**, 215–224.

20 W. N. Delgass, G. L. Haller, R. Kellerman and J. H. Lunsford, *Spectroscopy in Heterogeneous Catalysis*, Academic Press, New York, 1979, ch. 3, pp. 59–85.

21 H.-P. Boehm, H. Knözinger, in *Catalysis: Science and Technology*, ed. J. R. Anderson and M. Boudart, Springer, Berlin, Heidelberg, 1983, ch. 2, pp. 39–207.

22 Y. I. Yermakov, B. N. Kuznetsov and V. A. Zakharov, *Catalysis by Supported Complexes*, Elsevier, Amsterdam, 1981.

23 G. L. Schrader and C. P. Cheng, *J. Catal.*, 1983, **80**, 369–385.

24 L. Wang and W. K. Hall, *J. Catal.*, 1983, **82**, 177–184.

25 S. S. Chan, I. E. Wachs, L. L. Murrell, L. Wang and W. K. Hall, *J. Phys. Chem.*, 1984, **88**, 5831–5835.

26 J. M. Stencel, L. E. Markovsky, T. A. Sarkus, J. de Vries, R. Thomas and J. A. Moulijn, *J. Catal.*, 1984, **90**, 314–322.

27 S. Kuba and H. Knözinger, *J. Raman Spectrosc.*, 2002, **33**, 325–332.

28 A. Filtschew and C. Hess, *J. Phys. Chem. C*, 2017, **121**, 19280–19287.

29 L. Dixit, D. L. Gerrard and H. J. Bowley, *Appl. Spectrosc. Rev.*, 1986, **22**, 189–249.

30 G. Mestl and H. Knözinger, in *Handbook of Heterogeneous Catalysis*, 2nd ed., ed. G. Ertl, H. Knözinger, F.Schüth and J. Weitkamp, Wiley-VCH, Weinheim, Germany, 2008, ch. 3.1.3.8.

31 I. E. Wachs, in *Handbook of Raman Spectroscopy: From the research laboratory to the process line*, ed. I. R. Lewis and H. G. M. Edwards, Marcel Dekker, New York,

2001, ch. 20, pp. 799–834

32 W. Kiefer and H. J. Bernstein, *Appl. Spectrosc.*, 1971, **25**, 609–613.

33 M. Delhaye and P. Dhamelincourt, *J. Raman Spectrosc.*, 1975, **3**, 33–43.

34 M. Fleischmann, P. J. Hendra, A. J. McQuillan, R. L. Paul and E. S. Reid, *J. Raman Spectrosc.*, 1976, **4**, 269.

35 J. G. Grasselli, M. A. S. Hazle and L. E. Wolfram, in *Molecular Spectroscopy*, ed. A. R. West, Heyden & Son, London, 1977, ch. 14, p. 200.

36 E. Payen, J. Barbillat, J. Grimblot and J. P. Bonnelle, *Spectrosc. Lett.*, 1978, **11**, 997–1011.

37 T. Takenaka, *Adv. Colloid Interface Sci.*, 1979, **11**, 291.

38 M. A. Chesters and N. Sheppard, *Chem. Brit.*, 1981, **17**, 521.

39 B. A. Morrow, in *Vibrational Spectroscopy of Adsorbed Species*, ed. A. T. Bell and M. L. Hair, Washington, D.C., 1981, p. 119.

40 T. T. Nguyen, *J. Singapore Natl. Acad. Sci.*, 1983, **10**–**12**, 84.

41 N. Sheppard and J. Erkelens, *Appl. Spectrosc.*, 1984, **38**, 471–485.

42 J. R. Bartlett and R. P. Cooney, in *Spectroscopy of Inorganic-Based Materials*, Advances in Spectroscopy, Vol. 14, ed. R. J. H. Clark and R. E. Hester, Wiley, Chichester, UK 1987, p. 187.

43 J. M. Stencel, *Raman Spectroscopy for Catalysis*, Van Nostrand Reinhold Catalysis Series, Springer, New York, 1990.

44 I. E. Wachs and K. Segawa, in *Characterization of Catalytic Materials*, ed. I. E. Wachs, Butterworth-Heinemann, Boston, 1992.

45 G. Mestl, H. Knözinger and J. H. Lunsford, *Ber. Bunsenges. Phys. Chem.*, 1993, **97**, 319–321.

46 E. Garbowski and G. Coudurier, in *Catalyst Characterization: Physical Techniques for Solid Materials*, ed. B. Imelik and J. C. Vedrine, Springer, New York, 1994, ch. 3, pp.

45–60.

47 E. Payen and S. Kasztelan, *Trends Phys. Chem.*, 1994, **4**, 363–384.

48 H. Knözinger, *Catal. Today*, 1996, **32**, 71–80.

49 I. E. Wachs, *Catal. Today*, 1996, **27**, 437–455.

50 H. Knözinger and G. Mestl, *Top. Catal.*, 1999, **8**, 45–55.

51 W. H. Weber, in *Raman Applications in Catalysts for Exhaust-Gas Treatment*, ed. W. H. Weber and R. Merlin, Springer, Berlin, Heidelberg, 2000, pp. 233–270.

52 I. E. Wachs, *Top. Catal.*, 1999, **8**, 57–63.

53 G. Mestl, *J. Mol. Catal. A Chem.*, 2000, **158**, 45–65.

54 P. C. Stair, *Curr. Opin. Solid State Mater. Sci.*, 2001, **5**, 365–369.

55 M. A. Bañares and I. E. Wachs, *J. Raman Spectrosc.*, 2002, **33**, 359–380.

56 G. Mestl, *J. Raman Spectrosc.*, 2002, **33**, 333–347.

57 M. J. Weaver, *J. Raman Spectrosc.*, 2002, **33**, 309–317.

58 B. M. Weckhuysen, *Chem. Commun.*, 2002, **2**, 97–110.

59 B. M. Weckhuysen, *Phys. Chem. Chem. Phys.*, 2003, **5**, 4351.

60 M. A. Bañares, *Catal. Today*, 2005, **100**, 71–77.

61 H. Tian, I. E. Wachs and L. E. Briand, *J. Phys. Chem. B*, 2005, **109**, 23491–23499.

62 I. E. Wachs, *Catal. Today*, 2005, **100**, 79–94.

63 P. C. Stair, in *Advances in Catalysis, vol. 51*, ed. B. C. Gates and H. Knözinger, Academic Press, New York, 2007, pp. 75–98.

64 M. A. Bañares and G. Mestl, in *Advances in Catalysis, vol. 52*, ed. B. C. Gates and H. Knözinger, Academic Press, New York, 2009, pp. 43–128.

65 H. Kim, K. M. Kosuda, R. P. Van Duyne and P. C. Stair, *Chem. Soc. Rev.*, 2010, **39**, 4820–4844.

66 I. E. Wachs and C. A. Roberts, *Chem. Soc. Rev.*, 2010, **39**, 5002–5017.

67 E. Stavitski and B. M. Weckhuysen, *Chem. Soc. Rev.*, 2010, **39**, 4615–4625.

68 V. Calvino-Casilda, M. A. Bañares, in *Catalysis, vol. 24*, ed. J. J. Spivey and M. Gupta, Royal Society of Chemistry, Cambridge, 2012, pp. 1–47.

69 C. Hess, *Top. Catal.*, 2013, **56**, 1593–1600.

70 G. Mestl and M. A. Bañares, in *In-situ Characterization of Heterogeneous Catalysts*, ed. J. A. Rodriguez, J.C. Hanson, P. J. Chupas, John Wiley & Sons, New York, 2013, pp. 267–292.

71 I. E. Wachs and C. J. Keturakis, in *Comprehensive Inorganic Chemistry II*, ed. J. Reedijk and K. Poeppelmeier, Elsevier, New York, 2nd edn., 2013, pp.131–151.

72 S. Jin, Z. Feng, F. Fan and C. Li, *Catal. Lett.*, 2015, **145**, 468–481.

73 S. Bordiga, C. Lamberti, F. Bonino, A. Travert and F. Thibault-Starzyk, *Chem. Soc. Rev.*, 2015, **44**, 7262–7341.

74 T. Hartman, C. S. Wondergem, N. Kumar, A. van den Berg and B. M. Weckhuysen, *J. Phys. Chem. Lett.*, 2016, **7**, 1570–1584.

75 J. Strunk, M. A. Bañares and I. E. Wachs, *Top. Catal.*, 2017, **60**, 1577–1617.

76 S. Loridant, in *Characterization of Nanomaterials: Advances and Key Technologies*, ed. S. M. Bhagyaraj, O. S. Oluwafemi, N. Kalarikkal and S. Thomas, Elsevier, Cambridge, 2018, ch. 2, pp. 37–60.

77 Y. H. Wang, J. Wei, P. Radjenovic, Z. Q. Tian and J. F. Li, *Anal. Chem.*, 2019, **91**, 1675–1685.

78 S. Loridant, *Catal. Today*, 2020, https://doi.org/10.1016/j.cattod.2020.03.044.

79 F. Fan, Z. Feng and C. Li, *Acc. Chem. Res.*, 2010, **43**, 378–387.

80 R. R. Jones, D. C. Hooper, L. Zhang, D. Wolverson and V. K. Valev, *Nanoscale Res. Lett.*, 2019, **14**, 231.

81 H. Harima, *Microelectron. Eng.*, 2006, **83**, 126–129.

82 D. . Long, *The Raman Effect: A Unified Treatment of the Theory of Raman Scattering by Molecules*, John Wiley & Sons, Chichester, UK, 2002.

83 S. A. Asher, C. R. Johnson and J. Murtaugh, *Rev. Sci. Instrum.*, 1983, **54**, 1657–1662.

84 S. P. A. Fodor, R. P. Rava, R. A. Copeland and T. G. Spiro, *J. Raman Spectrosc.*, 1986, **17**, 471–475.

85 L. D. Ziegler, *J. Chem. Phys.*, 1987, **86**, 1703–1714.

86 S. A. Asher, R. W. Bormett, X. G. Chen, D. H. Lemmon, N. Cho, P. Peterson, M. Arrigoni, L. Spinelli, J. Cannon, *Appl. Spectrosc.*, 1993, **47**, 628–633.

87 J. S. W. Holtz, R. W. Bormett, Z. H. Chi, N. J. Cho, X. G. Chen, V. Pajcini, S. A. Asher, L. Spinelli, P. Owen, M. Arrigoni, *Appl. Spectrosc.*, 1996, **50**, 1459–1468.

88 Z. Wu, S. Dai and S. H. Overbury, *J. Phys. Chem. C*, 2010, **114**, 412–422.

89 C. Moisii, L. J. van de Burgt and A. E. Stiegman, *Chem. Mater.*, 2008, **20**, 3927–3935.

90 F. Fan, K. Sun, Z. Feng, H. Xia, B. Han, Y. Lian, P. Ying, C. Li, *Chem. Eur. J.*, 2009, **15**, 3268–3276.

91 J. Zhang, M. Li, Z. Feng, J. Chen and C. Li, *J. Phys. Chem. B*, 2006, **110**, 927–935.

92 J. Zhang, Z. C. Feng, M. J. Li, J. Chen, Q. Xu, Y.. Lian and C. Li, *Appl. Spectrosc.*, 2007, **61**, 38–47.

93 S. Bykov, I. Lednev, A. Ianoul, A. Mikhonin, C. Munro and S. A. Asher, *Appl. Spectrosc.*, 2005, **59**, 1541–1552.

94 X. J. Zhao, R. P. Chen, C. Tengroth and T. G. Spiro, *Appl. Spectrosc.*, 1999, **53**, 1200–1205.

95 G. Balakrishnan, Y. Hu, S. B. Nielsen and T. G. Spiro, *Appl. Spectrosc.*, 2005, **59**, 776–781.

96 L. Sokolov and I. Mukerji, *J. Phys. Chem. B*, 1998, **102**, 8314–8319.

97 D. Nitsche and C. Hess, *J. Raman Spectrosc.*, 2013, **44**, 1733–1738.

98 P. S. Waleska and C. Hess, *J. Phys. Chem. C*, 2016, **120**, 18510–18519.

99 A. Müller and T. Weber, *Appl. Catal.*, 1991, **77**, 243–250.

100 Y. T. Chua and P. C. Stair, *J. Catal.*, 2000, **196**, 66–72.

101 P. Beato, E. Schachtl, K. Barbera, F. Bonino and S. Bordiga, *Catal. Today*, 2013, **205**, 128–133.

102 M. Signorile, D. Rojo Gama, F. Bonino, S. Svelle, P. Beato and S. Bordiga, *Catal. Today*, 2019, **336**, 203–209.

103 A. Filtschew and C. Hess, *Appl. Catal. B*, 2018, **237**, 1066–1081.

104 P. Ober, S. Rogg and C. Hess, *ACS Catal.*, 2020, **10**, 2999–3008.

105 Y. T. Chua and P. C. Stair, *J. Catal.*, 2003, **213**, 39–46.

106 C. Li and P. C. Stair, in *11th International Congress on Catalysis – 40th Anniversary. Studies in Surface Science and Catalysis, vol. 101*, ed. J. W. Hightower, W. N. Delgass, E. Iglesia, A. T. Bell, Elsevier, Amsterdam 1996, pp. 881–890.

107 B. Chase, *Anal. Chem.*, 1987, **59**, 14, 881A–890A.

108 B. Chase, *J. Chem. Educ.*, 2007, **84**, 75–80.

109 B. Schrader, A. Hoffmann and S. Keller, *Spectrochim. Acta, Part A*, 1991, **47**, 1135–1148.

110 J. P. Holgado, M. D. Soriano, J. Jiménez-Jiménez, P. Concepción, A. Jiménez-López, A. Caballero, E. Rodríguez-Castellón and J. M. L. Nieto, *Catal. Today*, 2010, **155**, 296–301.

111 Z. Wu, A. J. Rondinone, I. N. Ivanov and S. H. Overbury, *J. Phys. Chem. C*, 2011, **115**, 25368–25378.

112 M. Guo, J. Lu, Y. Wu, Y. Wang and M. Luo, *Langmuir*, 2011, **27**, 3872–3877.

113 A. Kubas, J. Noak, A. Trunschke, R. Schlögl, F. Neese and D. Maganas, *Chem. Sci.*, 2017, **8**, 6338–6353.

114 J. Wang, G. Li, X. Ju, H. Xia, F. Fan, J. Wang, Z. Feng and C. Li, *J. Catal.*, 2013, **301**, 77–82.

115 Z. Wu, *Chin. J. Catal.*, 2014, **35**, 1591–1608.

116 Z. Wu, H. S. Kim, P. C. Stair, S. Rugmini and S. D. Jackson, *J. Phys. Chem. B*, 2005,

**109**, 2793–2800.

117 J. S. Woertink, P. J. Smeets, M. H. Groothaert, M. A. Vance, B. F. Sels, R. A. Schoonheydt and E. I. Solomon, *Proc. Natl. Acad. Sci. U. S. A.*, 2009, **106**, 18908–18913.

118 S. Jin, M. Guo, F. Fan, J. Yang, Y. Zhang, B. Huang, Z. Feng and C. Li, *J. Raman Spectrosc.*, 2013, **44**, 266–269.

119 H. S. Kim and P. C. Stair, *J. Phys. Chem. A*, 2009, **113**, 4346–4355.

120 D. Nitsche and C. Hess, *J. Phys. Chem. C*, 2016, **120**, 1025–1037.

121 P. Waleska, S. Rupp and C. Hess, *J. Phys. Chem. C*, 2018, **122**, 3386–3400.

122 R. W. Boyd, *Nonlinear Optics*, Elsevier, New York, 4th edn., 2020.

123 D. Wolverson, in *Characterization of Semiconductor Heterostructures and Nanostructures*, ed. C. Lamberti, Elsevier, Amsterdam, 2008, ch. 8, pp. 249–288.

124 A. Zumbusch, G. R. Holtom and X. S. Xie, *Phys. Rev. Lett.*, 1999, **82**, 4142–4145.

125 H. Kano, H. Segawa, P. Leproux and V. Couderc, *Opt. Rev.*, 2014, **21**, 752–761.

126 M. Fleischmann, P. J. Hendra and A. J. McQuillan, *Chem Phys. Lett.,* 1974, **26**, 163–166.

127 D. L. Jeanmaire and R. P. Van Duyne, *J. Electroanal. Chem. Interfacial Electrochem.*, 1977, **84**, 1-20.

128 R. P. Van Duyne, in *Chemical and Biochemical Applications of Lasers, vol. 4*, ed. C. B. Moore, Academic Press, New York, 1979, pp. 101–185.

129 M. G. Albrecht and J. A. Creighton, *J. Am. Chem. Soc.*, 1977, **99**, 5215–5217.

130 K. Kneipp, H. Kneipp, I. Itzkan, R. R. Dasari and M. S. Feld, *Chem. Rev.*, 1999, **99**, 2957–2975.

131 Z. Q. Tian, B. Ren and D. Y. Wu, *J. Phys. Chem. B*, 2002, **106**, 9463–9483.

132 S. Schlücker, *Angew. Chem., Int. Ed.*, 2014, **53**, 4756–4795.

133 W. Xie and S. Schlücker, *Rep. Prog. Phys.*, 2014, **77**, 116502.

134 P. G. Etchegoin, *Phys. Chem. Chem. Phys.*, 2009, **11**, 7348–7349.

135 R. Long, Y. Li, L. Song and Y. Xiong, *Small*, 2015, **11**, 3873–3889.

136 C. Zhan, X. J. Chen, Y. F. Huang, D. Y. Wu and Z. Q. Tian, *Acc. Chem. Res.*, 2019, **52**, 2784–2792.

137 J. F. Li, Y. F. Huang, Y. Ding, Z. L. Yang, S. B. Li, X. S. Zhou, F. R. Fan, W. Zhang, Z. Y. Zhou, D. Y. Wu, B. Ren, Z. L. Wang and Z. Q. Tian, *Nature*, 2010, **464**, 392–395.

138 J. R. Anema, J.-F. Li, Z.-L. Yang, B. Ren and Z.-Q. Tian, *Annu. Rev. Anal. Chem.*, 2011, **4**, 129–150.

139 R. Narayanan, R. J. Lipert and M. D. Porter, *Anal. Chem.*, 2008, **80**, 2265–2271.

140 S. Ben-Jaber, W. J. Peveler, R. Quesada-Cabrera, E. Cortés, C. Sotelo-Vazquez, N. Abdul-Karim, S. A. Maier and I. P. Parkin, *Nat. Commun.*, 2016, **7**, 12189.

141 D. Glass, E. Cortés, S. Ben-Jaber, T. Brick, W. J. Peveler, C. S. Blackman, C. R. Howle, R. Quesada-Cabrera, I. P. Parkin and S. A. Maier, *Adv. Sci.*, 2019, **30**, 1901841.

142 B.-S. Yeo, J. Stadler, T. Schmid, R. Zenobi and W. Zhang, *Chem. Phys. Lett.*, 2009, **472**, 1–13.

143 C. Blum, L. Opilik, J. M. Atkin, K. Braun, S. B. Kämmer, V. Kravtsov, N. Kumar, S. Lemeshko, J.-F. Li, K. Luszcz, T. Maleki, A. J. Meixner, S. Minne, M. B. Raschke, B. Ren, J. Rogalski, D. Roy, B. Stephanidis, X. Wang, D. Zhang, J.-H. Zhong and R. Zenobi, *J. Raman Spectrosc.*, 2014, **45**, 22–31.

144 K. F. Domke and B. Pettinger, *ChemPhysChem*, 2009, **10**, 1794–1798.

145 E. M. van Schrojenstein Lantman, T. Deckert-Gaudig, A. J. G. Mank, V. Deckert and B. M. Weckhuysen, *Nat. Nanotechnol.*, 2012, **7**, 583–586.

146 N. Kumar, B. Stephanidis, R. Zenobi, A. J. Wain and D. Roy, *Nanoscale*, 2015, **7**, 7133–7137.

147 J. H. Zhong, X. Jin, L. Meng, X. Wang, H. S. Su, Z. L. Yang, C. T. Williams and B. Ren, *Nat. Nanotechnol.*, 2017, **12**, 132–136.

148 N. Martín Sabanés, L. M. A. Driessen and K. F. Domke, *Anal. Chem.*, 2016, **88**, 7108–7114.

149 N. Martín Sabanés, T. Ohto, D. Andrienko, Y. Nagata and K. F. Domke, *Angew. Chem., Int. Ed.*, 2017, **56**, 9796–9801.

150 M. Mattei, G. Kang, G. Goubert, D. V. Chulhai, G. C. Schatz, L. Jensen and R. P. Van Duyne, *Nano Lett.*, 2017, **17**, 590–596.

151 N. Kumar, S. Kalirai, A. J. Wain and B. M. Weckhuysen, *ChemCatChem*, 2019, **11**, 417–423.

152 M. A. Bañares, M. O. Guerrero-Pérez, J. L. G. Fierro and G. G. Cortez, *J. Mater. Chem.*, 2002, **12**, 3337–3342.

153 A. Chakrabarti, M. E. Ford, D. Gregory, R. Hu, C. J. Keturakis, S. Lwin, Y. Tang, Z. Yang, M. Zhu, M. A. Bañares and I. E. Wachs, *Catal. Today*, 2017, **283**, 27–53.

154 C. P. Cheng, J. D. Ludowise and G. L. Schrader, *Appl. Spectrosc.*, 1980, **34**, 146–150.

155 S. S. Chan and A. T. Bell, *J. Catal.*, 1984, **89**, 433–441.

156 G. Mestl, M. P. Rosynek and J. H. Lunsford, *J. Phys. Chem. B*, 1997, **101**, 9321–9328.

157 F. Ben Abdelouahab, R. Olier, N. Guilhaume, F. Lefebvre and J. C. Volta, *J. Catal.*, 1992, **134**, 151–167.

158 N. Zimmerer and W. Kiefer, *Appl. Spectrosc.*, 1974, **28**, 279–281.

159 P. C. Stair, in *In-Situ Spectroscopy in Heterogeneous Catalysis*, ed. J. F. Haw, Wiley-VCH, Weinheim, Germany, 2002, pp. 121–138.

160 M. V. Martínez-Huerta, G. Deo, J. L. G. Fierro and M. A. Bañares, *J. Phys. Chem. C*, 2008, **112**, 11441–11447.

161 M. Mathieu, M. Baltes, K. Cassiers, V. Meynen, P. Cool, P. Van Der Voort, B. M. Weckhuysen, R. A. Schoonheydt and E. F. Vansant, *Spectrochim. Acta, Part A*, 2004,

**60**, 2969–2975.

162 J. J. Bravo-Suárez and P. D. Srinivasan, *Catal. Rev.*, 2017, **59**, 295–445.

163 F. C. Meunier, *Chem. Soc. Rev.*, 2010, **39**, 4602–4614.

164 M. A. Bañares and S. J. Khatib, *Catal. Today*, 2004, **96**, 251–257.

165 M. Geske, O. Korup and R. Horn, *Catal. Sci. Technol.*, 2013, **3**, 169–175.

166 A. Maghsoumi, A. Ravanelli, F. Consonni, F. Nanni, A. Lucotti, M. Tommasini, A. Donazzi and M. Maestri, *React. Chem. Eng.*, 2017, **2**, 908–918.

167 S. B. Rasmussen, R. López-Medina, R. Portela, E. Mikolajska, M. Daturi, P. Ávila and M. A. Bañares, *Catal. Sci. Technol.*, 2015, **5**, 4942–4945.

168 R. Domènech-Ferrer, F. Ziegs, S. Klod, I. Lindemann, R. Voigtländer, L. Dunsch and O. Gutfleisch, *Anal. Chem.*, 2011, **83**, 3199–3204.

169 H. Reymond and P. Rudolf von Rohr, *Rev. Sci. Instrum.*, 2017, **88**, 114103.

170 G. Gouadec and P. Colomban, *Prog. Cryst. Growth Charact. Mater.*, 2007, **53**, 1–56.

171 G. Gouadec and P. Colomban, *J. Raman Spectrosc.*, 2007, **38**, 598–603.

172 M. Šćepanović, M. Grujić-Brojčin, Z. Dohčević-Mitrović and Z. V Popović, *J. Phys. Conf. Ser.*, 2010, **253**, 012015.

173 G. G. Siu, M. J. Stokes and Y. Liu, *Phys. Rev. B - Condens. Matter Mater. Phys.*, 1999, **59**, 3173–3179.

174 A. Diéguez, A. Romano-Rodríguez, A. Vilà and J. R. Morante, *J. Appl. Phys.*, 2001, **90**, 1550–1557.

175 S. Hakkar, S. Achache, F. Sanchette, Z. Mekhalif, N. Kamoun and A. Boumaza, *J. Mol. Eng. Mater.*, 2019, **7**, 1950003.

176 T. Pagnier, M. Boulova, N. Sergent, P. Bouvier and G. Lucazeau, *J. Raman Spectrosc.*, 2007, **38**, 756–761.

177 U. Balachandran and N. G. Eror, *J. Solid State Chem.*, 1982, **42**, 276–282.

178 T. Ohsaka, S. Yamaoka and O. Shimomura, *Solid State Commun.*, 1979, **30**, 345–347.

179 E. Barbarini, I. N. Kholmanov, P. Piseri, C. Ducati, C. E. Bottani, P. Milani, *Appl. Phys. Lett.*, 2002, **81**, 3052–3054.

180 A. Pougin, A. Lüken, C. Klinkhammer, D. Hiltrop, M. Kauer, K. Tölle, M. Havenith-Newen, K. Morgenstern, W. Grünert, M. Muhler and J. Strunk, *Top. Catal.*, 2017, **60**, 1744–1753.

181 J. Zhang, Q. Xu, M. Li, Z. Feng and C. Li, *J. Phys. Chem. C*, 2009, **113**, 1698–1704.

182 F. Tian, Y. Zhang, J. Zhang and C. Pan, *J. Phys. Chem. C*, 2012, **116**, 7515–7519.

183 A. Filtschew, K. Hofmann and C. Hess, *J. Phys. Chem. C*, 2016, **120**, 6694–6703.

184 C. Schilling, A. Hofmann, C. Hess and M. V. Ganduglia-Pirovano, *J. Phys. Chem. C*, 2017, **121**, 20834–20849.

185 P. Shvets, O. Dikaya, K. Maksimova and A. Goikhman, *J. Raman Spectrosc.*, 2019, **50**, 1226–1244.

186 *Morphological, Compositional, and Shape Control of Materials for Catalysis*, ed. P. Fornasiero and M. Cargnello, Elsevier, Amsterdam, 2017.

187 C. Schilling, M. V. Ganduglia-Pirovano and C. Hess, *J. Phys. Chem. Lett.*, 2018, **9**, 6593–6598.

188 Z. Wu, M. Li, J. Howe, H. M. Meyer III and S. H. Overbury, *Langmuir*, 2010, **26**, 16595–16606.

189 S. Chen, D. Li, Y. Liu and W. Huang, *J. Catal.*, 2016, **341**, 126–135.

190 F. Fan, Z. Feng and C. Li, *Chem. Soc. Rev.*, 2010, **39**, 4794–4801.

191 C. Hess, in *Comprehensive Inorganic Chemistry II*, ed. J. Reedijk and K. Poeppelmeier, Elsevier, Amsterdam, 2nd edn., 2013, vol. 7, ch. 10, pp. 231–245.

192 M. Signorile, F. Bonino, A. Damin and S. Bordiga, *J. Phys. Chem. C*, 2016, **120**, 18088–18092.

193 Ö. Attila, H. E. King, F. Meirer and B. M. Weckhuysen, *Chem. Eur. J.*, 2019, **25**, 7158–7167.

194 G. Fleury and M. B. J. Roeffaers, *ACS Catal.* 2020, **10**, 14801−14809.

195 Q. Guo, K. Sun, Z. Feng, G. Li, M. Guo, F. Fan and C. Li, *Chem. Eur. J.*, 2012, **18**, 13854–13860.

196 Q. Wang, Z. Li, M. A. Bañares, L. T. Weng, Q. Gu, J. Price, W. Han and K. L. Yeung, *Small*, 2019, **15**, 1903525.

197 C. Hess, *ChemPhysChem*, 2009, **10**, 319-326.

198 D. Nitsche and C. Hess, *Catal. Commun.*, 2014, **52**, 40–44.

199 D. Maganas, A. Trunschke, R. Schlögl and F. Neese, *Faraday Discuss.*, 2016, **188**, 181–197.

200 P. Ruff, L. Schumacher, S. Rogg and C. Hess, *ACS Catal.*, 2019, **9**, 6349–6361.

201 H.-S. Kim, S. A. Zygmunt, P. C. Stair, P. Zapol and L. A. Curtiss, *J. Phys. Chem. C*, 2009, **113**, 8836–8843.

202 H. Kim, G. A. Ferguson, L. Cheng, S. A. Zygmunt, P. C. Stair and L. A. Curtiss, *J. Phys. Chem. C*, 2012, **116**, 2927–2932.

203 S. Benomar, A. Massó, B. Solsona, R. Issaadi and J. M. López Nieto, *Catalysts*, 2018, **8**, 126.

204 C. Hess, P. Waleska, M. Ratzka, T. V. W. Janssens, S. B. Rasmussen and P. Beato, *Top. Catal.*, 2017, **60**, 1631–1640.

205 A. Iglesias-Juez, M. V. Martínez-Huerta, E. Rojas-García, J. M. Jehng and M. A. Bañares, *J. Phys. Chem. C*, 2018, **122**, 1197–1205.

206 A. E. Lewandowska, M. Calatayud, F. Tielens and M. A. Bañares, *J. Phys. Chem. C*, 2011, **115**, 24133–24142.

207 A. E. Lewandowska, M. Calatayud, F. Tielens and M. A. Bañares, *J. Phys. Chem. C*, 2013, **117**, 25535–25544.

208 R. J. G. Nuguid, D. Ferri, A. Marberger, M. Nachtegaal and O. Kröcher, *ACS Catal.*, 2019, **9**, 6814–6820.

209 W. C. Vining, A. Goodrow, J. Strunk and A. T. Bell, *J. Catal.*, 2010, **270**, 163–171.

210 J. Moncada, W. R. Adams, R. Thakur, M. Julin and C. A. Carrero, *ACS Catal.*, 2018, **8**, 8976–8986.

211 M. O. Guerrero-Pérez, J. M. Rosas, R. López-Medina, M. A. Bañares, J. Rodríguez-Mirasol and T. Cordero, *J. Phys. Chem. C*, 2012, **116**, 20396–20403.

212 F. Rabello de Castro, Y. Lau Lam, M. Hawrylak Herbst, M. Maciel Pereira, T. Crispim da Silva, N. Homs and P. Ramirez de la Piscina, *Eur. J. Inorg. Chem.*, 2013, 241–247.

213 J. E. Molinari and I. E. Wachs, *J. Am. Chem. Soc.*, 2010, **132**, 12559–12561.

214 O. Yalcin, J. E. Molinari Erwin, D. Gerceker, I. Onal and I. E. Wachs, *ACS Catal.*, 2020, **10**, 1566–1574.

215 E. Mikolajska, S. B. Rasmussen, A. E. Lewandowska and M. A. Bañares, *Phys. Chem. Chem. Phys.*, 2012, **14**, 2128–2136.

216 A. E. Stiegman, *J. Phys. Chem. C*, 2011, **115**, 10917–10924.

217 G. Tsilomelekis and S. Boghosian, *Catal. Sci. Technol.*, 2013, **3**, 1869–1888.

218 K. Ding, A. Gulec, A. M. Johnson, T. L. Drake, W. Wu, Y. Lin, E. Weitz, L. D. Marks, P. C. Stair, *ACS Catal.*, 2016, **6**, 5740–5746.

219 J. P. Thielemann, T. Ressler, A. Walter, G. Tzolova-Müller and C. Hess, *Appl. Catal. A*, 2011, **399**, 28–34.

220 J. P. Thielemann and C. Hess, *J. Catal.*, 2012, **288**, 124–126.

221 J. P. Thielemann, G. Weinberg and C. Hess, *ChemCatChem*, 2011, **3**, 1814–1821.

222 J. Gao, Y. Zheng, J.-M. Jehng, Y. Tang, I. E. Wachs and S. G. Podkolzin, *Science*, 2015, **348**, 686–690.

223 G. Tsilomelekis, G. D. Panagiotou, P. Stathi, A. G. Kalampounias, K. Bourikas, C. Kordulis, Y. Deligiannakis, S. Boghosian and A. Lycourghiotis, *Phys. Chem. Chem. Phys.*, 2016, **18**, 23980–23989.

224 S. Lwin, C. Keturakis, J. Handzlik, P. Sautet, Y. Li, A. I. Frenkel and I. E. Wachs, *ACS*

*Catal.*, 2015, **5**, 1432–1444.

225 S. Lwin, Y. Li, A. I. Frenkel and I. E. Wachs, *ACS Catal.*, 2016, **6**, 3061–3071.

226 Y. He, M. E. Ford, M. Zhu, Q. Liu, Z. Wu and I. E. Wachs, *Appl. Catal. B*, 2016, **188**, 123–133.

227 A. Chakrabarti, M. Gierada, J. Handzlik and I. E. Wachs, *Top. Catal.*, 2016, **59**, 725–739.

228 M. Daniel and S. Loridant, *J. Raman Spectrosc.*, 2012, **43**, 1312–1319.

229 Z. Say, E. I. Vovk, V. I. Bukhtiyarov and E. Ozensoy, *Appl. Catal. B*, 2013, **142**–**143**, 89–100.

230 M. Lohrenscheit and C. Hess, *ChemCatChem*, 2016, **8**, 523–526.

231 Q. Wang, K. L. Yeung and M. A. Bañares, *J. Catal.*, 2018, **364**, 80–88.

232 K. Fujiwara, U. Müller and S. E. Pratsinis, *ACS Catal.*, 2016, **6**, 1887–1893.

233 Y. Kang, M. Sun and A. Li, *Catal. Lett.*, 2012, **142**, 1498–1504.

234 S. Berka, V. Fleischer and C. Hess, *Proceedings*, 2019, **14**, 11.

235 A. K. Elger and C. Hess, *Sensors*, 2019, **19**, 5075.

236 M. Zhu, P. Tian, R. Kurtz, T. Lunkenbein, J. Xu, R. Schlögl, I. E. Wachs and Y. F. Han, *Angew. Chem. Int. Ed.*, 2019, **58**, 9083–9087.

237 K. V. Raun, L. F. Lundegaard, J. Chevallier, P. Beato, C. C. Appel, K. Nielsen, M. Thorhauge, A. D. Jensen and M. Høj, *Catal. Sci. Technol.*, 2018, **8**, 4626–4637.

238 K. Routray, W. Zhou, C. J. Kiely and I. E. Wachs, *ACS Catal.*, 2011, **1**, 54–66.

239 F. Zhang, C.-H. Chen, J. C. Hanson, R. D. Robinson, I. P. Herman and S.-W. Chan, *J. Am. Ceram. Soc.*, 2006, **89**, 1028–1036.

240 M. Yashima, H. Arashi, M. Kakihana and M. Yoshimura, *J. Am. Ceram. Soc.*, 1994, **77**, 1067–1071.

241 C. Andriopoulou, A. Trimpalis, K. C. Petallidou, A. Sgoura, A. M. Efstathiou and S. Boghosian, *J. Phys. Chem. C*, 2017, **121**, 7931–7943.

242 H. Richter, Z. P. Wang and L. Ley, *Solid State Commun.*, 1981, **39**, 625–629.

243 I. H. Campbell and P. M. Fauchet, *Solid State Commun.*, 1986, **58**, 739–741.

244 W. H. Weber, K. C. Hass and J. R. McBride, *Phys. Rev. B*, 1993, **48**, 178–185.

245 J. E. Spanier, R. D. Robinson, F. Zhang, S.-W. Chan and I. P. Herman, *Phys. Rev. B*, 2001, **64**, 245407.

246 J. Zuo, C. Xu, Y. Liu and Y. Qian, *Nanostruct. Mater.*, 1998, **10**, 1331–1335.

247 S. Balaji, Y. Djaoued and J. Robichaud, *J. Raman Spectrosc.*, 2006, **37**, 1416–1422.

248 I. Kosacki, T. Suzuki, H. U. Anderson and P. Colomban, *Solid State Ionics*, 2002, **149**, 99–105.

249 J. R. McBride, K. C. Hass, B. D. Poindexter and W. H. Weber, *J. Appl. Phys.*, 1994, **76**, 2435–2441.

250 C. Kittel, *Einführung in die Festkörperphysik*, Oldenbourg Wissenschaftsverlag München, 2013.

251 A. Trovarelli, *Catal. Rev.*, 1996, **38**, 439–520.

252 Y. Ji, T. J. Toops, J. A. Pihl and M. Crocker, in *Appl. Catal. B*, 2009, **91**, 329–338.

253 R. J. Gorte, *AIChE J.*, 2010, **56**, 1126-1135.

254 Y. Li, Q. Sun, M. Kong, W. Shi, J. Huang, J. Tang and X. Zhao, *J. Phys. Chem. C*, 2011, **115**, 14050–14057.

255 I. Al-Shankiti, F. Al-Otaibi, Y. Al-Salik and H. Idriss, *Top. Catal.*, 2013, **56**, 1129–1138.

256 T. Zacherle, A. Schriever, R. A. De Souza and M. Martin, *Phys. Rev. B*, 2013, **87**, 134104.

257 J. Paier, C. Penschke and J. Sauer, *Chem. Rev.*, 2013, **113**, 3949–3985.

258 R. Kopelent, J. A. van Bokhoven, J. Szlachetko, J. Edebeli, C. Paun, M. Nachtegaal and O. V. Safonova, *Angew. Chem. Int. Ed.*, 2015, **54**, 8728–8731.

259 C. Schilling and C. Hess, *J. Phys. Chem. C*, 2018, **122**, 2909–2917.

260 R. Schmitt, A. Nenning, O. Kraynis, R. Korobko, A. I. Frenkel, I. Lubomirsky, S. M. Haile and J. L. M. Rupp, *Chem. Soc. Rev.*, 2020, **49**, 554–592.

261 C. Schilling, A. Hofmann, C. Hess and M. V. Ganduglia-Pirovano, *J. Phys. Chem. C*, 2017, **121**, 20834–20849.

262 Y. Lee, G. He, A. J. Akey, R. Si, M. Flytzani-Stephanopoulos and I. P. Herman, *J. Am. Chem. Soc.*, 2011, **133**, 12952–12955.

263 C. Schilling and C. Hess, *ACS Catal.*, 2019, **9**, 1159–1171.

264 V. V. Pushkarev, V. I. Kovalchuk and J. L. d'Itri, *J. Phys. Chem. B*, 2004, **108**, 5341–5348.

265 J. Guzman, S. Carrettin and A. Corma, *J. Am. Chem. Soc.*, 2005, **127**, 3286–3287.

266 Y. M. Choi, H. Abernathy, H.-T. Chen, M. C. Lin and M. Liu, *ChemPhysChem*, 2006, **7**, 1957–1963.

267 M. Huang and S. Fabris, *Phys. Rev. B*, 2007, **75**, 081404.

268 Y. Zhao, B. T. Teng, X. D. Wen, Y. Zhao, Q. P. Chen, L. H. Zhao and M. F. Luo, *J. Phys. Chem. C*, 2012, **116**, 15986–15991.

269 J. Kullgren, K. Hermansson and P. Broqvist, *Phys. Status Solidi RRL*, 2014, **8**, 600–604.

270 J. Buckeridge, D. O. Scanlon, A. Walsh, C. R. A. Catlow and A. A. Sokol, *Phys. Rev. B*, 2013, **87**, 214304.

271 T. Taniguchi, T. Watanabe, N. Sugiyama, A. K. Subramani, H. Wagata, N. Matsushita and M. Yoshimura, *J. Phys. Chem. C*, 2009, **113**, 19789–19793.

272 O. Kraynis, I. Lubomirsky and T. Livneh, *J. Phys. Chem. C*, 2019, **123**, 24111–24117.

273 A. Banerji, V. Grover, V. Sathe, S. K. Deb and A. K. Tyagi, *Solid State Commun.*, 2009, **149**, 1689–1692.

274 R. Schmitt, J. Spring, R. Korobko and J. L. M. Rupp, *ACS Nano*, 2017, **11**, 8881–8891.

275 A. M. Efstathiou and S. Y. Christou, in *Catalysis by Ceria and Related Materials*, ed.

A. Trovarelli and P. Fornasiero, Imperial College Press, London, 2013, pp. 139–221.

276 R. Di Monte and J. Kašpar, *Catal. Today*, 2005, **100**, 27–35.

277 X. Pan, M.-Q. Yang, X. Fu, N. Zhang and Y.-J. Xu, *Nanoscale*, 2013, **5**, 3601.

278 A. Li Bassi, D. Cattaneo, V. Russo, C. E. Bottani, E. Barborini, T. Mazza, P. Piseri, P. Milani, F. O. Ernst, K. Wegner and S. E. Pratsinis, *J. Appl. Phys.*, 2005, **98**, 074305.

279 G. Liu, H. G. Yang, X. Wang, L. Cheng, H. Lu, L. Wang, G. Q. Lu and H. M. Cheng, *J. Phys. Chem. C*, 2009, **113**, 21784–21788.

280 F. Rossella, P. Galinetto, M. C. Mozzati, L. Malavasi, Y. Diaz Fernandez, G. Drera and L. Sangaletti, *J. Raman Spectrosc.*, 2010, **41**, 558–565.

281 X. Chen, L. Liu, P. Y. Yu and S. S. Mao, *Science*, 2011, **331**, 746–750.

282 B. Santara, P. K. Giri, K. Imakita and M. Fujii, *Nanoscale*, 2013, **5**, 5476–5488.

283 R. Verma and S. K. Samdarshi, *J. Alloys Compd.*, 2015, **629**, 105–112.

284 H. Fukushima, T. Kozu, H. Shima, H. Funakubo, H. Uchida, T. Katoda and K. Nishida, in *2015 Joint IEEE International Symposium on the Applications of Ferroelectrics (ISAF), International Symposium on Integrated Functionalities (ISIF), and Piezoelectric Force Microscopy Workshop (PFM)*, IEEE, Piscataway, NJ, 2015, pp. 28–31.

285 Q. Zhao, L. Fu, D. Jiang, J. Ouyang, Y. Hu, H. Yang and Y. Xi, *Commun. Chem.*, 2019, **2**, 11.

286 Z. Wang, W. Wang, L. Zhang and D. Jiang, *Catal. Sci. Technol.*, 2016, **6**, 3845–3853.

287 P. Waleska and C. Hess, *Catal. Lett.*, 2018, **148**, 2537–2547.

288 M. Che and A. J. Tench, in *Advances in Catalysis, vol. 32*, ed. D. D. Eley, H. Pines and P. B. Weisz, Academic Press, New York, 1983, pp. 1–148.

289 J. H. Lunsford, X. Yang, K. Haller, J. Laane, G. Mestl and H. Knoezinger, *J. Phys. Chem.*, 1993, **97**, 13810–13813.

290 S. C. Su and A. T. Bell, *Catal. Lett.*, 1996, **36**, 15–19.

291 C. Hess and J. H. Lunsford, *J. Phys. Chem. B*, 2003, **107**, 1982–1987.

292 S. Bordiga, A. Damin, F. Bonino, G. Ricchiardi, C. Lamberti and A. Zecchina, *Angew. Chem. Int. Ed.*, 2002, **41**, 4734–4737.

293 Z. X. Gao, H. S. Kim, Q. Sun, P. C. Stair and W. M. H. Sachtler, *J. Phys. Chem. B*, 2001, **105**, 6186–6190.

294 H. Xia, K. Sun, K. Sun, Z. Feng, W. X. Li and C. Li, *J. Phys. Chem. C*, 2008, **112**, 9001–9005.

295 I. G. Denisov, P. J. Mak, T. M. Makris, S. G. Sligar and J. R. Kincaid, *J. Phys. Chem. A*, 2008, **112**, 13172–13179.

296 C. Hess and J. H. Lunsford, *J. Phys. Chem. B*, 2002, **106**, 6358–6360.

297 D. Uy, A. E. O'Neill and W. H. Weber, *Appl. Catal. B*, 2002, **35**, 219–225.

298 D. Uy, A. E. O'Neill, J. Li and W. L. H. Watkins, *Catal. Lett.*, 2004, **95**, 191–201.

299 A. Urakawa, N. Maeda and A. Baiker, *Angew. Chem. Int. Ed.*, 2008, **47**, 9256–9259.

300 A. Filtschew, D. Stranz and C. Hess, *Phys. Chem. Chem. Phys.*, 2013, **15**, 9066.

301 W. Krasser and A. J. Renouprez, *J. Raman Spectrosc.*, 1979, **8**, 92–94.

302 W. Krasser and A. J. Renouprez, *J. Raman Spectrosc.*, 1981, **11**, 425–429.

303 W. Krasser, A. Fadini and E. Rozemüller, *J. Mol. Structure*, 1980, **66**, 135–148.

304 W. Krasser, A. Fadini and A. J. Renouprez, *J. Catal.*, 1980, **62**, 94–98.

305 M. Swanson, V. V. Pushkarev, V. I. Kovalchuk and J. L. d'itri, *Catal. Lett.*, 2007, **116**, 41–45.

306 A. K. Elger, J. Baranyai, K. Hofmann and C. Hess, *ACS Sens.*, 2019, **4**, 1497–1501.

307 M. Ziemba and C. Hess, *Catal. Sci. Technol.*, 2020, **10**, 3720–3730.

308 C. Li and P. C. Stair, *Catal. Lett.,* 1996, **36**, 119–123.

309 D. Uy, A. Dubkov, G. W. Graham and W. H. Weber, *Catal. Lett.*, 2000, **68**, 25–32.

310 Y. Deng, L. R. L. Ting, P. H. L. Neo, Y.-J. Zhang, A. A. Peterson and B. S. Yeo, *ACS Catal.*, 2016, **6**, 7790–7798.

311 F. Tuinstra and J. L. Koenig, *J. Chem. Phys.*, 1970, **53**, 1126–1130.

312 A. C. Ferrari and D. M. Basko, *Nat. Nanotechnol.*, 2013, **8**, 235–246.

313 B. M. Vogelaar, A. D. van Langeveld, S. Eijsbouts and J. A. Moulijn, *Fuel*, 2007, **86**, 1122–1129.

314 C. Li and P. C. Stair, *Catal. Today*, 1997, **33**, 353–360.

315 Y. T. Chua and P. C. Stair, *J. Catal.*, 2003, **213**, 39–46.

316 P. M. Allotta and P. C. Stair, *ACS Catal.*, 2012, **2**, 2424–2432.

317 H. An, F. Zhang, Z. Guan, X. Liu, F. Fan and C. Li, *ACS Catal.*, 2018, **8**, 9207–9215.

318 M. Signorile, F. Bonino, A. Damin and S. Bordiga, *J. Phys. Chem. C*, 2015, **119**, 11694–11698.

319 M. Signorile, D. Rojo-Gama, F. Bonino, P. Beato, S. Svelle and S. Bordiga, *Phys. Chem. Chem. Phys.*, 2018, **20**, 26580–26590.

320 J. J. H. B. Sattler, A. M. Mens and B. M. Weckhuysen, *ChemCatChem*, 2014, **6**, 3139–3145.

321 K. H. Cats and B. M. Weckhuysen, *ChemCatChem*, 2016, **8**, 1531–1542.

322 E. Sartoretti, C. Novara, F. Giorgis, M. Piumetti, S. Bensaid, N. Russo and D. Fino, *Sci. Rep.*, 2019, **9**, 9–13.

323 http://www.shapesoftware.com/.

324 D. Nitsche and C. Hess, *Chem. Phys. Lett.*, 2014, **616**–**617**, 115–119.

325 M. Ziemba, V. Ganduglia-Pirovano and C. Hess, *Faraday Discuss.*, in press, DOI:10.1039/C9FD00133F.

326 Y. Xu, F. Wang, X. Liu, Y. Liu, M. Luo, B. Teng, M. Fan and X. Liu, *J. Phys. Chem. C*, 2019, **123**, 18889–18894.

327 A. E. J. Hoffman, L. Vanduyfhuys, I. Nevjestić, J. Wieme, S. M. J. Rogge, H. Depauw, P. Van Der Voort, H. Vrielinck and V. Van Speybroeck, *J. Phys. Chem. C*, 2018, **122**, 2734–2746.

328 Q. Liang, S. Dwaraknath and K. A. Persson, *Sci. Data*, 2019, **6**, 135.

329 F. Neese, *Wiley Interdiscip. Rev.: Comput. Mol. Sci.*, 2012, **2**, 73–78.

330 Z.-B. Ding, M. Tommasini and M. Maestri, *ChemPlusChem*, 2017, **82**, 924–932.

331 S. M. Morton and L. Jensen, *J. Am. Chem. Soc.*, 2009, **131**, 4090–4098.

332 L. L. Zhao, L. Jensen and G. C. Schatz, *Nano Lett.*, 2006, **6**, 1229–1234.

333 J. E. Moore, S. M. Morton and L. Jensen, *J. Phys. Chem. Lett.*, 2012, **3**, 2470–2475.

334 A. Mohammed, W. Hu, P. O. Andersson, M. Lundquist, L. Landström, Y. Luo and H. Ågren, *Chem. Phys. Lett.*, 2013, **581**, 70–73.

335 W. Hu, G. Tian, S. Duan, L.-L. Lin, Y. Ma and Y. Luo, *Chem. Phys.*, 2015, **453**–**454**, 20–25.

336 D. Karhánek, T. Bučko and J. Hafner, *J. Phys. Condens. Matter*, 2010, **22**, 265005.

337 A. T. Zayak, Y. S. Hu, H. Choo, J. Bokor, S. Cabrini, P. J. Schuck and J. B. Neaton, *Phys. Rev. Lett.*, 2011, **106**, 083003.

338 W. Hu, S. Duan, G. Zhang, Y. Ma, G. Tian and Y. Luo, *J. Phys. Chem. C*, 2015, **119**, 28992–28998.

339 B. L. Mojet, L. Coulier, J. van Grondelle, J. W. Niemantsverdriet and R. A. van Santen, *Catal. Lett.*, 2004, **96**, 1–4.

340 W. Xie and S. Schlücker, *Chem. Commun.*, 2018, **54**, 2326–2336.

341 K. Fukui, I. Oshima, H. Oosterbeek and Y. Iwasawa, *Chem. Phys. Lett.*, 1999, **299**, 158–164.

342 C. Hess, M. Bonn, S. Funk and M. Wolf, *Chem. Phys. Lett.*, 2000, **325**, 139–145.

343 P. C. Thüne and J. W. (Hans) Niemantsverdriet, *Surf. Sci.*, 2009, **603**, 1756–1762.

344 A. Westermann, C. Geantet, P. Vernoux and S. Loridant, *J. Raman Spectrosc.*, 2016, **47**, 1276–1279.

345 T. Taniguchi, T. Watanebe, S. Ichinohe, M. Yoshimura, K. Katsumata, K. Okada and N. Matsushita, *Nanoscale*, 2010, **2**, 1426.

346 I. Lezcano-Gonzalez, E. Campbell, A. E. J. Hoffman, M. Bocus, I. V. Sazanovich, M. Towrie, M. Agote-Aran, E. K. Gibson, A. Greenaway, K. De Wispelaere, V. Van Speybroeck and A. M. Beale, *Nature Mater.*, 2020, **19**, 1081–1087.

347 M. Kögler and B. Heilala, *Meas. Sci. Technol.*, 2021, **32,** 012002.

348 B. Notari, in *Advances in Catalysis, vol. 41*, ed. D. D. Eley, W. O. Haag and B. Gates, Academic Press, New York, 1996, pp. 253–334.

349 W. Fan, R.-G. Duan, T. Yokoi, P. Wu, Y. Kubota and T. Tatsumi, *J. Am. Chem. Soc.*, 2008, **130**, 10150–10164.

350 Q. Guo, Z. Feng, G. Li, F. Fan and C. Li, *J. Phys. Chem. C*, 2013, **117**, 2844–2848.

351 T. Kim, R. S. Assary, H. Kim, C. L. Marshall, D. J. Gosztola, L. A. Curtiss and P. C. Stair, *Catal. Today*, 2013, **205**, 60–66.

352 C. T. Williams, A. A. Tolia, M. J. Weaver and C. G. Takoudis, *Chem. Eng. Sci.*, 1996, **51**, 1673–1682.

353 C. T. Williams, C. A. Black, M. J. Weaver and C. G. Takoudis, *J. Phys. Chem. B*, 1997, **101**, 2874–2883.

354 S. Park, P. Yang, P. Corredor and M. J. Weaver, *J. Am. Chem. Soc.*, 2002, **124**, 2428–2429.

355 K. N. Heck, B. G. Janesko, G. E. Scuseria, N. J. Halas and M. S. Wong, *J. Am. Chem. Soc.*, 2008, **130**, 16592–16600.

356 E. V. Formo, Z. Wu, S. M. Mahurin and S. Dai, *J. Phys. Chem. C*, 2011, **115**, 9068–9073.

357 Y.-F. Huang, H.-P. Zhu, G.-K. Liu, D.-Y. Wu, B. Ren and Z.-Q. Tian, *J. Am. Chem. Soc.*, 2010, **132**, 9244−9246.

358 M. Sun, Y. Huang, L. Xia, X. Chen and H. Xu, *J. Phys. Chem. C*, 2011, **115**, 9629−9636.

359 B. Dong, Y. Fang, X. Chen, H. Xu and M. Sun, *Langmuir*, 2011, **27**, 10677−10682.

360 J. Langer *et al.*, *ACS Nano*, 2020, **14**, 28−117

361 Q. Zhang, D. A. Blom and H. Wang, *Chem. Mater.*, 2014, **26**, 5131−5142.

362 Q. Zhang and H. Wang, *ACS Catal.*, 2014, **4**, 4027−4033.

363 Q. Cui, A. Yashchenok, L. Zhang, L. Li, A. Masic, G. Wienskol, H. Mőhwald and M. Bargheer, *ACS Appl. Mater. Interf.*, 2014, **6**, 1999−2002.

364 M. Muniz-Miranda, *Appl. Catal. B*, 2014, **46**, 147–150.

365 M. Muniz-Miranda, *J. Anal. Bioanal. Tech.*, 2015, **6**, 1000286.

366 Z. Zhang, T. Deckert-Gaudig, P. Singh and V. Deckert, *Chem. Commun.*, 2015, **51**, 3069–3072.

367 H.-K. Choi, W.-H. Park, C.-G. Park, H.-H. Shin, K. S. Lee and Z. H. Kim, *J. Am. Chem. Soc.*, 2016, **138**, 4673−4684.

368 R. L. Gieseking, M. A. Ratner and G. C. Schatz, in *Frontiers of Plasmon Enhanced Spectroscopy; ACS Symposium Series 1245*, American Chemical Society, Washington, DC, 2016; vol. 1, pp 1−22.

369 N. C. Brandt, E. L. Keller and R. R. Frontiera, *J. Phys. Chem. Lett.,* 2016, **7**, 3179−3185.

370 H.-K. Choi, K. S. Lee, H.-H. Shin and Z. H. Kim, *J. Phys. Chem. Lett.*, 2016, **7**, 4099−4104.

371 X. Ren, E. Cao, W. Lin, Y. Song, W. Liang and J. Wang, *RSC Adv.*, 2017, **7**, 31189−31203.

372 C. Zhan, X.-J. Chen, J. Yi, J.-F. Li, D.-Y. Wu and Z.-Q. Tian, *Nat. Rev. Chem.*, 2018, **2,** 216−230.

373 Y.-F. Huang, M. Zhang, L.-B. Zhao, J.-M. Feng, D.-Y. Wu, B. Ren and Z.-Q. Tian, *Angew. Chem.*, 2014, **126**, 2385–2389.

374 S. Guan, O. Donovan-Sheppard, C. Reece, D. J. Willock, A. J. Wain and G. A. Attard, *ACS Catal.*, 2016, **6**, 1822–1832.

375 S.-Y. Ding, J. Yi, J.-F. Li, B. Ren, D.-Y. Wu, R. Panneerselvam and Z.-Q. Tian, *Nat. Rev. Mater.*, 2016, **1**, 16021.

376 H. Zhang, X.-G. Zhang, J. Wei, C. Wang, S. Chen, H.-L. Sun, Y.-H. Wang, B.-H. Chen, Z.-L. Yang, D.-Y. Wu, J.-F. Li and Z.-Q. Tian, *J. Am. Chem. Soc.*, 2017, **139**, 10339–10346.

377 H. Zhang, C. Wang, H.-L. Sun, G. Fu, S. Chen, Y.-J. Zhang, B.-H. Chen, J. R. Anema, Z.-L. Yang, J.-F. Li and Z.-Q. Tian, *Nat. Commun.*, 2017, **8**, 15447.

378 T. Hartman and B. M. Weckhuysen, *Chem. Eur. J.*, 2018, **24**, 3733–3741.

379 T. Hartman, C. S. Wondergem and B. M. Weckhuysen, *ChemPhysChem*, 2018, **19**, 2461–2467.

380 G. Hartman, R. G. Geitenbeek, and B. Weckhuysen, *Nat. Catal.*, 2019, **2**, 986–996.

381 C. S. Wondergem, T. Hartman and B. M. Weckhuysen, *ACS Catal.*, 2019, **9**, 10794–10802.

382 C. S. Wondergem, J. J. G. Kromwijk, M. Slagter, W. L. Vrijburg, E. J. M. Hensen, M. Monai, C. Vogt and B. M. Weckhuysen, *ChemPhysChem*, 2020, **21**, 625–632.

383 C. Z. Cunniff, S. E. Specht, A. M. Love, P. Uchupalanun, J. M. Venegas, C. E. Kruszynski and I. Hermans, *J. Phys. Chem. C*, 2019, **123**, 25220–25227.

384 X.-D. Lin, V. Uzayisenga, J.-F. Li, P.-P. Fang, D.-Y. Wu, B. Ren and Z.-Q. Tian, *J. Raman Spectrosc.*, 2012, **43**, 40–45.

385 D. V. Voronine, A. M. Sinyukov, X. Hua, K. Wang, P. K. Jha, E. Munusamy, S. E. Wheeler, G. Welch, A. V. Sokolov and M. O. Scully, *Sci. Rep.*, 2012, **2**, 1–5.

386 S. Yampolsky, D. A. Fishman, S. Dey, E. Hulkko, M. Banik, E. O. Potma and V. A. Apkarian, *Nat. Photonics*, 2014, **8**, 650–656.

387 S. Roy and A. Baiker, *Chem. Rev.*, 2009, **109**, 4054–4091.

388 G. Liu and P.-X. Gao, *Catal. Sci. Technol.*, 2011, **1**, 552.

389 M. Haruta, T. Kobayashi, H. Sano and N. Yamada, *Chem. Lett.*, 1987, **16**, 405–408.

390 G. Hutchings, *J. Catal.*, 1985, **96**, 292–295.

391 A. S. K. Hashmi and G. J. Hutchings, *Angew. Chem. Int. Ed.*, 2006, **45**, 7896–7936.

392 S. Carrettin, P. Concepción, A. Corma, J. M. López Nieto and V. F. Puntes, *Angew. Chem. Int. Ed.*, 2004, **43**, 2538–2540.

393 Q. Fu, H. Saltsburg, M. Flytzani-Stephanopoulos, *Science*, 2003, **301**, 935–938.

394 C. Schilling, M. Ziemba, C. Hess and M. V. Ganduglia-Pirovano, *J. Catal.*, 2020, **383**, 264–272.

395 H. Y. Kim, H. M. Lee and G. Henkelman, *J. Am. Chem. Soc.*, 2012, **134**, 1560–1570.

396 Y.-G. Wang, D. Mei, V.-A. Glezakou, J. Li and R. Rousseau, *Nat. Commun.*, 2015, **6**, 6511.

397 C. E. Harvey, I. E. I. Petterson, B. M. Weckhuysen, C. Gooijer, F. Ariese and A. J. G. Mank, *Appl. Spectrosc.*, 2012, **66**, 1179–1185.

398 J. Wei, S.-N. Qin, J.-L. Liu, X.-Y. Ruan, Z. Guan, H. Yan, D.-Y. Wei, H. Zhang, J. Cheng, H. Xu, Z.-Q. Tian and J.-F. Li, *Angew. Chem. Int. Ed.*, 2020, **59**, 10343–10347.

399 V. Joseph, C. Engelbrekt, J. Zhang, U. Gernert, J. Ulstrup and J. Kneipp, *Angew. Chem. Int. Ed.*, 2012, **51**, 7592–7596.

400 W. Xie, R. Grzeschik and S. Schlücker, *Angew. Chem. Int. Ed.*, 2016, **55**, 13729–13733.

401 W. Xie, C. Herrmann, K. Kömpe, M. Haase and S. Schlücker, *J. Am. Chem. Soc.*, 2011, **133**, 19302–19305.

402 A. Gellé, T. Jin, L. de la Garza, G. D. Price, L. V. Besteiro and A. Moores, *Chem. Rev.*, 2020, **120**, 986–1041.

403 Z. Zhang and J. Kneipp, *Anal. Chem.*, 2018, **90**, 9199–9205.

404 P. Singh and V. Deckert, *Chem. Commun.*, 2014, **50**, 11204–11207.

405 K. J. Savage, M. M. Hawkeye, R. Esteban, A. G. Borisov, J. Aizpurua and J. J. Baumberg, *Nature*, 2012, **491**, 574–577.

406 Z. Zhang, M. Sun, P. Ruan, H. Zheng and H. Xu, *Nanoscale*, 2013, **5**, 4151–4155.

407 A. Urakawa and A. Baiker, *Top. Catal.*, 2009, **52**, 1312–1322.

408 J.-D. Grunwaldt, S. Hannemann, C. G. Schroer and A. Baiker, *J. Phys. Chem. B*, 2006, **110**, 8674–8680.

409 M. G. O'Brien, A. M. Beale, S. D. M. Jacques, M. Di Michiel and B. M. Weckhuysen, *ChemCatChem*, 2009, **1**, 99–102.

410 M. Dieterle, G. Weinberg and G. Mestl, *Phys. Chem. Chem. Phys.*, 2002, **4**, 812–821.

411 M. A. Camacho-López, L. Escobar-Alarcón, M. Picquart, R. Arroyo, G. Córdoba and E. Haro-Poniatowski, *Opt. Mater.*, 2011, **33**, 480–484.

412 S. T. Oyama and W. Zhang, *J. Am. Chem. Soc.*, 1996, **118**, 7173–7177.

413 W. Zhang and S. T. Oyama, *J. Phys. Chem.*, 1996, **100**, 10759–10767.

414 J. R. Schmink, J. L. Holcomb and N. E. Leadbeater, *Chem. Eur. J.*, 2008, **14**, 9943–9950.

415 L. R. Knöpke, N. Nemati, A. Köckritz, A. Brückner and U. Bentrup, *ChemCatChem*, 2010, **2**, 273–280.

416 T. Moreno, M. A. Morán López, I. Huerta Illera, C. M. Piqueras, A. Sanz Arranz, J. García Serna and M. J. Cocero, *Chem. Eng. J.*, 2011, **166**, 1061–1065.

417 S. Mozharov, A. Nordon, D. Littlejohn, C. Wiles, P. Watts, P. Dallin and J. M. Girkin, *J. Am. Chem. Soc.*, 2011, **133**, 3601–3608.

418 E. Mikolajska, V. Calvino-Casilda and M. A. Bañares, *Appl. Catal. A*, 2012, **421**–**422**, 164–171.

419 S. Salkic, L. H. Eckler and M. J. Nee, *J. Raman Spectrosc.*, 2013, **44**, 1746–1752.

420 H.-Y. Chan, V.-H. Nguyen, J. C. S. Wu, V. Calvino-Casilda, M. A. Bañares and H. Bai, *Catalysts*, 2015, **5**, 518–533.

421 E. Cao, G. Brett, P. J. Miedziak, J. M. Douthwaite, S. Barrass, P. F. McMillan, G. J. Hutchings and A. Gavriilidis, *Catal. Today*, 2017, **283**, 195–201.

422 E. Cao, S. Firth, P. F. McMillan and A. Gavriilidis, *Catal. Today*, 2007, **126**, 119–126.

423 E. Cao, M. Sankar, S. Firth, K. F. Lam, D. Bethell, D. K. Knight, G. J. Hutchings, P. F. McMillan and A. Gavriilidis, *Chem. Eng. J.*, 2011, **167**, 734–743.

424 A. Urakawa, F. Trachsel, P. R. von Rohr and A. Baiker, *Analyst*, 2008, **133**, 1352.

425 P. Beato, R. Kraehnert, S. Engelschalt, T. Frank, and R. Schlögl, *Chem. Eng. J.*, 2008, **135**, S247–S253.

426 G. Li, D. Hu, G. Xia and Z. C. Zhang, *Top. Catal.*, 2009, **52**, 1381–1387.

427 D. Baurecht and U. P. Fringeli, *Rev. Sci. Instrum.*, 2001, **72**, 3782–3792.

428 A. Urakawa, T. Bürgi and A. Baiker, *Chem. Eng. Sci.*, 2008, **63**, 4902–4909.

429 P. Müller and I. Hermans, *Ind. Eng. Chem. Res.*, 2017, **56**, 1123–1136.

430 A. Urakawa, W. Van Beek, M. Monrabal-Capilla, J. R. Galán-Mascarós, L. Palin and M. Milanesio, *J. Phys. Chem. C*, 2011, **115**, 1323–1329.

431 C. C. Neacsu, J. Dreyer, N. Behr and M. B. Raschke, *Phys. Rev. B*, 2006, **73**, 193406.

432 E. Bailo and V. Deckert, *Angew. Chem. Int. Ed.*, 2008, **47**, 1658–1661.

433 M. D. Sonntag, J. M. Klingsporn, L. K. Garibay, J. M. Roberts, J. A. Dieringer, T. Seideman, K. A. Scheidt, L. Jensen, G. C. Schatz and R. P. Van Duyne, *J. Phys. Chem. C*, 2012, **116**, 478–483.

434 R. Zhang, Y. Zhang, Z. C. Dong, S. Jiang, C. Zhang, L. G. Chen, L. Zhang, Y. Liao, J. Aizpurua, Y. Luo, J. L. Yang and J. G. Hou, *Nature*, 2013, **498**, 82–86.

435 A. B. Zrimsek, N. Chiang, M. Mattei, S. Zaleski, M. O. McAnally, C. T. Chapman, A.-I. Henry, G. C. Schatz and R. P. Van Duyne, *Chem. Rev.*, 2017, **117**, 7583–7613.

436 E. Stavitski and B. M. Weckhuysen, *Chem. Soc. Rev.*, 2010, **39**, 4615.

437 F. Schueth, *J. Phys. Chem.*, 1992, **96**, 7493–7496.

438 F. Marlow, K. Hoffmann, W. Hill, J. Kornatowski and J. Caro, in *Zeolites and Related*

*Microporous Materials: State of the Art 1994*, ed. J. Weitkamp, H. G. Karge, H. Pfeifer and W. Hölderich, Elsevier, Oxford, 1994, pp. 2277–2284.

439 M. H. F. Kox, E. Stavitski and B. M. Weckhuysen, *Angew. Chem. Int. Ed.*, 2007, **46**, 3652–3655.

440 D. Mores, J. Kornatowski, U. Olsbye and B. M. Weckhuysen, *Chem. Eur. J.*, 2011, **17**, 2874–2884.

441 A. Gasecka, L.-Q. Dieu, D. Brühwiler and S. Brasselet, *J. Phys. Chem. B*, 2010, **114**, 4192–4198.

442 M. A. van der Veen, B. F. Sels, D. E. De Vos and T. Verbiest, *J. Am. Chem. Soc.*, 2010, **132**, 6630–6631.

443 M. H. F. Kox, K. F. Domke, J. P. R. Day, G. Rago, E. Stavitski, M. Bonn and B. M. Weckhuysen, *Angew. Chem. Int. Ed.*, 2009, **48**, 8990–8994.

444 G. W. H. Wurpel, J. M. Schins and M. Müller, *Opt. Lett.*, 2002, **27**, 1093–1095.

445 K. F. Domke, J. P. R. Day, G. Rago, T. A. Riemer, M. H. F. Kox, B. M. Weckhuysen and M. Bonn, *Angew. Chem. Int. Ed.*, 2012, **51**, 1343–1347.

446 K.-L. Liu, A. V. Kubarev, J. Van Loon, H. Uji-i, D. E. De Vos, J. Hofkens and M. B. J. Roeffaers, ACS Nano, 2014, 8, 12650–12659.

447 G. Fleury, J. A. Steele, I. C. Gerber, F. Jolibois, P. Puech, K. Muraoka, S. H. Keoh, W. Chaikittisilp, T. Okubo and M. B. J. Roeffaers, J. Phys. Chem. Lett., 2018, 9, 1778−1782.

448 Y.-P. Huang, S.-C. Huang, X.-J. Wang, N. Bodappa, C.-Y. Li, H. Yin, H.-S. Su, M. Meng, H. Zhang, B. Ren, Z.-L. Yang, R. Zenobi, Z.-Q. Tian and J.-F. Li, *Angew. Chem. Int. Ed.*, 2018, **57**, 7523–7527.

449 N. Kumar, C. S. Wondergem, A. J. Wain and B. M. Weckhuysen, *J. Phys. Chem. Lett.*, 2019, **10**, 1669–1675.

450 H. Yin, L.-Q. Zheng, W. Fang, Y.-H. Lai, N. Porenta, G. Goubert, H. Zhang, H.-S. Su,

B. Ren, J. O. Richardson, J.-F. Li and R. Zenobi, *Nature Catal.*, 2020, **3**, 834–842.

451 A. Brückner, *Chem. Commun.*, 2005, 1761–1763.

452 G. Le Bourdon, F. Adar, M. Moreau, S. Morel, J. Reffner, A. S. Mamede, C. Dujardin and E. Payen, *Phys. Chem. Chem. Phys.*, 2003, **5**, 4441–4444.

453 J. C. J. Camp, M. D. Mantle, A. P. E. York and J. McGregor, *Rev. Sci. Instrum.*, DOI:10.1063/1.4882317.

454 S. J. Tinnemans, M. H. F. Kox, M. W. Sletering, T. A. (Xander) Nijhuis, T. Visser and B. M. Weckhuysen, *Phys. Chem. Chem. Phys.*, 2006, **8**, 2413.

454 A. Filtschew and C. Hess, *J. Phys. Chem. C*, 2017, **121**, 19280–19287.

455 A. M. Beale, A. M. J. van der Eerden, K. Kervinen, M. A. Newton and B. M. Weckhuysen, *Chem. Commun.*, 2005, 3015–3017.

456 C. Hess, *J. Catal.*, 2007, **248**, 120–123.

457 C. T. Nottbohm and C. Hess, *Catal. Commun.*, 2012, **22**, 39–42.

458 U. Caudillo-Flores, M. J. Muñoz-Batista, A. Kubacka and M. Fernández-García, *ChemPhotoChem*, 2018, **2**, 777–785.

459 Y. Gao, W. Nie, X. Wang, F. Fan and C. Li, *Chem. Commun.*, 2020, **56**, 1007–1021.

460 V. M. V and G. Nageswaran, *Front. Chem.*, 2020, **8**, 23.

461 X. Li, H.-Y. Wang, H. Yang, W. Cai, S. Liu and B. Liu, *Small Methods*, 2018, **2**, 1700395.

462 Y. Deng and B. S. Yeo, *ACS Catal.*, 2017, **7**, 7873–7889.

463 H. Yang, Y. Hu, J. Chen, M.-S. Balogun, P. Fang, S. Zhang, J. Chen and Y. Tong, *Adv. Energy Mater.*, 2019, **9**, 1901396.

464 J.-C. Dong, X.-G. Zhang, V. Briega-Martos, X. Jin, J. Yang, S. Chen, Z.-L. Yang, D.-Y. Wu, J. M. Feliu, C. T. Williams and Z.-Q. Tian, Nature Energy, 2019, 4, 60-67.

465 Z. Liang, Q. Zou, Y. Wang and Y.-C. Lu, *Small Methods*, 2017, **1**, 1700150.

466 T. Ichimura, N. Hayazawa, M. Hashimoto, Y. Inouye and S. Kawata, *Phys. Rev. Lett.*,

2004, **92**, 20–23.